


Spring 2015

# Investigations of carbon nanotube catalyst morphology and behavior with transmission electron microscopy

Sammy M. Saber  
*Purdue University*

Follow this and additional works at: [https://docs.lib.purdue.edu/open\\_access\\_dissertations](https://docs.lib.purdue.edu/open_access_dissertations)

 Part of the [Materials Science and Engineering Commons](#), and the [Nanoscience and Nanotechnology Commons](#)

---

## Recommended Citation

Saber, Sammy M., "Investigations of carbon nanotube catalyst morphology and behavior with transmission electron microscopy" (2015). *Open Access Dissertations*. 555.  
[https://docs.lib.purdue.edu/open\\_access\\_dissertations/555](https://docs.lib.purdue.edu/open_access_dissertations/555)

This document has been made available through Purdue e-Pubs, a service of the Purdue University Libraries. Please contact [epubs@purdue.edu](mailto:epubs@purdue.edu) for additional information.

**PURDUE UNIVERSITY  
GRADUATE SCHOOL  
Thesis/Dissertation Acceptance**

This is to certify that the thesis/dissertation prepared

By Sammy M. Saber

Entitled

Investigations of Carbon Nanotube Catalyst Morphology and Behavior with Transmission Electron Microscopy

For the degree of Doctor of Philosophy

Is approved by the final examining committee:

Eric P. Kvam

Chair

Fabio H. Ribeiro

Eric A. Stach

Benji Maruyama

Timothy S. Fisher

To the best of my knowledge and as understood by the student in the Thesis/Dissertation Agreement, Publication Delay, and Certification Disclaimer (Graduate School Form 32), this thesis/dissertation adheres to the provisions of Purdue University's "Policy of Integrity in Research" and the use of copyright material.

Approved by Major Professor(s): Eric P. Kvam

Approved by: David F. Bahr

Head of the Departmental Graduate Program

4/16/2015

Date



INVESTIGATIONS OF CARBON NANOTUBE CATALYST MORPHOLOGY AND  
BEHAVIOR WITH TRANSMISSION ELECTRON MICROSCOPY

A Dissertation

Submitted to the Faculty

of

Purdue University

by

Sammy M. Saber

In Partial Fulfillment of the

Requirements for the Degree

of

Doctor of Philosophy

May 2015

Purdue University

West Lafayette, Indiana



For my parents, Mahmoud and Margaret

Your love, time and effort in raising me have culminated to this moment in my life.

For my daughter, Amandine

I vowed as a father to teach you how to be a good person, but instead you're teaching me.

For my wife, Dorothée

The time and effort I have put into building our family is the best thing I have ever done.

I couldn't have picked a better partner.

Thank you

## ACKNOWLEDGEMENTS

First and foremost I would like to thank Prof. Alina Alexeenko for her time. Discussions and conversations with her were the inspiration for the Ostwald ripening work. I would also like to thank Dr. Eric Stach for his guidance, patience, and continued faith in me, which began by accepting a naïve undergraduate student for a summer project. Dr. Dmitri Zakharov was an invaluable mentor to me who taught me the intricacies of TEM operation and experimental design. I would also like to thank Dr. Tim Sands for supporting my research work during times when funding was hard to come by. Dr. Ahmad Islam and Dr. Pavel Nikolaev were instrumental in the completion of the work presented in this dissertation through their experimental work and sample preparation. I would like to thank Dr. Rahul Rao and Dr. Avetik Hartyunyan for their cooperation and assistance in the Ostwald ripening work, and, finally, Dr. Benji Maruyama for his guidance, without which, the bulk of this work would not be possible.

## TABLE OF CONTENTS

	Page
LIST OF FIGURES .....	vi
ABSTRACT .....	xiii
CHAPTER 1. INTRODUCTION .....	1
1.1 Introduction / Motivation .....	1
1.2 Carbon Nanotubes .....	2
CHAPTER 2. CNT GROWTH .....	5
2.1 Chemical Vapor Deposition .....	5
2.2 Catalysts .....	6
2.3 Substrate .....	9
2.4 Growth Temperature .....	10
2.5 Gasses .....	10
2.6 The Role of Water .....	12
2.7 Ostwald Ripening .....	13
CHAPTER 3. CHARACTERIZATION TECHNIQUES .....	20
3.1 Electron Microscopy .....	20
3.2 TEM Sample Preparation .....	32
3.3 Raman Spectroscopy .....	35
CHAPTER 4. INFLUENCE OF CATALYST MORPHOLOGY .....	38
4.1 Catalyst Morphology and CNT Growth .....	38
4.2 Experimental Setup and Results .....	39
4.3 Discussion .....	46
CHAPTER 5. CONTROLLING CATALYST ACTIVITY VIA SUBSTRATE MANIPULATION .....	52
5.1 Ion Beam Bombardment of Substrates .....	52
5.2 Experimental Setup & Results .....	53

	Page
5.3 Discussion.....	60
CHAPTER 6. USING GRADIENTS TO STUDY CNT GROWTH .....	63
6.1 CNT Growth Dependence on Catalyst Size.....	63
6.2 Experimental Setup.....	64
6.3 Results.....	69
6.4 Discussion.....	79
CHAPTER 7. FUTURE WORK AND CONCLUSIONS.....	82
LIST OF REFERENCES.....	87
APPENDIX.....	93
VITA.....	119

## LIST OF FIGURES

Figure	Page
Figure 1 - Diagram of a graphene sheet with the vectors, $a_1$ and $a_2$ , defining the circumference of a carbon nanotube, $C = na_1 + ma_2$ , where $C$ is the circumference and $n$ and $m$ are integers greater than 0.....	3
Figure 2 - Height of carpet grown at different times with water and without <sup>11</sup> .....	11
Figure 3 - Histograms of the number of particles after annealing for 30 seconds and 5 minutes in hydrogen (left graph) and hydrogen without water (right graph) <sup>62</sup> .....	13
Figure 4 - Histograms of particle size after annealing for 1.5 and 5 minutes on (a) sapphire, (b) annealed e-beam alumina, (c) ALD alumina, (d) e-beam alumina, and (e) sputtered alumina <sup>52</sup> .....	15
Figure 5 - Graph of CNT carpet height with respect to growth time for sapphire and sputtered, e-beam, annealed e-beam, and ALD alumina <sup>52</sup> .....	16
Figure 6 - Catalyst decay rate measured versus (a) inverse temperature and (b) acetylene flow rate.....	18
Figure 7 - TEM image over the wedge-shaped edge of a SiN TEM window. The dark and light bands running horizontally across the image are thickness fringes with the thicker region of the sample at the top of the image and the thinner region of the sample at the bottom. Note that this is a standard TEM image and was not taken in a two-beam condition, thus illustrating the power of the two-beam condition approximation. ....	26
Figure 8 - Figure from Dresselhaus et al. <sup>71</sup> showing the relationship between electronic transition energies and SWNT diameter, where $E_{ii}^M$ and $E_{ii}^S$ are transition energies for metallic and semiconducting tubes respectively.....	36
Figure 9 - Plan view TEM images of 1.8 nm iron film after annealing in 2 Torr $H_2$ at 500°C for 30 minutes.....	40

Figure	Page
Figure 10 - Plan view TEM images of 1.8 nm of iron film annealed in 2 Torr H <sub>2</sub> at 500°C for 30 minutes followed by 12 Torr of Ar at 700°C for 30 minutes.....	40
Figure 11 - TEM images of the top row are images of a sample annealed in 100 sccm argon and water with 400 sccm of argon. The middle row of images is from a sample annealed in 200 sccm argon and water with 300 sccm argon, and the last row of images was taken from a sample annealed in 500 sccm of argon and water. All samples were first annealed in 2 Torr of H <sub>2</sub> for 30 minutes at 700°C for 30 minutes.....	42
Figure 12 - Histogram of particle diameters for the 1.8 nm Fe films annealed in hydrogen and argon and water.....	43
Figure 13 - The mobility of iron (diffusivity x solubility) plotted versus the flow rate of water. As the activity of water increases, the mobility of iron decreases.....	44
Figure 14 - An iron film reduced in (a) 500 mTorr of hydrogen for 90 minutes, (b) 500 mTorr of helium for 60 minutes (c) vacuum for 40 minutes, and then blocks of 30 minutes in argon at (d) 1.5 mTorr, (e) 20 mTorr, (f) 500 mTorr, and (g) 1200 mTorr.....	46
Figure 15 - Rough schematic of a gas molecule colliding with a catalyst. The incident momentum of the gas molecule is labeled and defined as its mass multiplied by its volume.....	47
Figure 16 - SEM images of (a) the patterned sapphire substrate showing VA-CNT growth, and (b) a higher resolution image of the edge of the growth.....	54
Figure 17 - Raman spectra measured from the top of the VA-CNT growth showing a G/D ratio of about 1.4 and the presence of the G' band. The radial breathing modes are shown in the top-left inset from about 150 – 300 cm <sup>-1</sup> .....	55
Figure 18 - TEM image of a small subset of CNTs grown on the modified sapphire substrate. A variety of CNTs are present, including single-wall, double-wall, and MWNTs .....	56
Figure 19 - Cross-section TEM image of ion beam damaged c-cut sapphire substrate with deposited iron. The substrate, and two-layer damaged region consisting of an amorphous layer and interfacial layer are clearly visible .....	57

Figure	Page
Figure 20 - XPS data detailing the enhancement of surface activity with respect to ion bombardment beam energy. (a) Diagrams of the O 1s FWHM and (b) the ratios of the area under the O 1s peak to the area under the Al 2p peak for untreated sapphire and sapphire damaged by 3 keV and 5 keV ion beams. The dotted lines indicate the level of untreated ALD alumina. Diagrams (c), (d), and (e) show the O 1s peaks for pristine sapphire, 3 keV, and 5 keV respectively. Notice how the O 1s peak shifts with increasing ion beam energy .....	58
Figure 21 - Results of varying accelerating voltage on (a) VA-CNT carpet height, (c) surface roughness, and (e) particle count, and the results of varying ion density on (b) VA-CNT carpet height, (d) surface roughness, and (f) particle count.....	59
Figure 22 - Schematic diagram of sputter coating gradient onto a substrate with gradient accentuated to show orientation.....	66
Figure 23 - Schematic of sample preparation controlling gradient deposition.....	68
Figure 24 - Set of images from the Fe gradient sample A2, all taken at 255,000x magnification. The top, middle, and bottom rows are sets of 3 images from a Fe film thickness of 0.3 nm, 0.4 nm, and 0.5 nm, respectively. The scale bar, seen in the top left image, is 10 nm.....	70
Figure 25 - Set of images from the Fe gradient sample A2, all taken at 255,000x magnification. The top, middle, and bottom rows are sets of 3 images from a Fe film thickness of 0.6 nm, 0.7 nm, and 0.8 nm, respectively. The scale bar, seen in the top left image, is 10 nm.....	71
Figure 26 - Set of images from the Fe gradient sample A2, all taken at 255,000x magnification. The top, middle, and bottom rows are sets of 3 images from a Fe film thickness of 0.9 nm, 1.0 nm, and 1.1 nm, respectively. The scale bar, seen in the top left image, is 10 nm.....	72
Figure 27 - Set of images from the Fe gradient sample A2, all taken at 255,000x magnification. The top, middle, and bottom rows are sets of 3 images from a Fe film thickness of 1.2 nm, 1.3 nm, and 1.4 nm, respectively. The scale bar, seen in the top left image, is 10 nm.....	73
Figure 28 - Set of images from the Fe gradient sample A2, all taken at 255,000x magnification. The top, middle, and bottom rows are sets of 3 images from a Fe film thickness of 1.5 nm, 1.6 nm, and 1.7 nm, respectively. The scale bar, seen in the top left image, is 10 nm.....	74

Figure	Page
Figure 29 - Set of images from the Fe gradient sample A2, all taken at 255,000x magnification. The top, middle, and bottom rows are sets of 3 images from a Fe film thickness of 1.8 nm, 1.9 nm, and 2.0 nm, respectively. The scale bar, seen in the top left image, is 10 nm.....	75
Figure 30 - Sample image from the 1.0 nm film thickness on sample A2 displayed for the purpose of explaining the particle analysis procedure. Particles were manually masked with polygons or ovals and then fed into a Matlab script running the Dunin-Borkowski algorithm. Six particles are numbered on the edge, and they would all be counted as half particles, only to be included in the particle density statistics and not the particle diameter statistics. ....	76
Figure 31 - Average particle diameter in nm (y-axis) versus Fe gradient film thickness in nm (x-axis). ....	77
 Appendix Figure	
Figure A1 - Histogram of nanoparticle diameters at 0.4 nm film thickness of Sample T3. ....	93
Figure A2 - Histogram of nanoparticle diameters at 0.4 nm film thickness of Sample T3 segmented by core-shell structure. ....	94
Figure A3 - Histogram of nanoparticle diameters at 0.5 nm film thickness of Sample T3. ....	94
Figure A4 - Histogram of nanoparticle diameters at 0.5 nm film thickness of Sample T3 segmented by core-shell structure. ....	95
Figure A5 - Histogram of nanoparticle diameters at 0.6 nm film thickness of Sample T3. ....	95
Figure A6 - Histogram of nanoparticle diameters at 0.6 nm film thickness of Sample T3 segmented by core-shell structure. ....	96
Figure A7 - Histogram of nanoparticle diameters at 0.7 nm film thickness of Sample T3. ....	96
Figure A8 - Histogram of nanoparticle diameters at 0.7 nm film thickness of Sample T3 segmented by core-shell structure. ....	97
Figure A9 - Histogram of nanoparticle diameters at 0.4 nm film thickness of Sample T7. ....	97



Appendix Figure	Page
Figure A10 - Histogram of nanoparticle diameters at 0.4 nm film thickness of Sample T7 segmented by core-shell structure. ....	98
Figure A11 - Histogram of nanoparticle diameters at 0.5 nm film thickness of Sample T7. ....	98
Figure A12 - Histogram of nanoparticle diameters at 0.5 nm film thickness of Sample T7 segmented by core-shell structure. ....	99
Figure A13 - Histogram of nanoparticle diameters at 0.6 nm film thickness of Sample T7. ....	99
Figure A14 - Histogram of nanoparticle diameters at 0.6 nm film thickness of Sample T7 segmented by core-shell structure. ....	100
Figure A15 - Histogram of nanoparticle diameters at 0.7 nm film thickness of Sample T7. ....	100
Figure A16 - Histogram of nanoparticle diameters at 0.7 nm film thickness of Sample T7 segmented by core-shell structure. ....	101
Figure A17 - Histogram of nanoparticle diameters at 0.8 nm film thickness of Sample T7. ....	101
Figure A18 - Histogram of nanoparticle diameters at 0.8 nm film thickness of Sample T7 segmented by core-shell structure. ....	102
Figure A19 - Histogram of nanoparticle diameters at 0.9 nm film thickness of Sample T7. ....	102
Figure A20 - Histogram of nanoparticle diameters at 0.9 nm film thickness of Sample T7 segmented by core-shell structure. ....	103
Figure A21 - Histogram of nanoparticle diameters at 1.0 nm film thickness of Sample T7. ....	103
Figure A22 - Histogram of nanoparticle diameters at 1.0 nm film thickness of Sample T7 segmented by core-shell structure. ....	104
Figure A23 - Histogram of nanoparticle diameters at 0.4 nm film thickness of Sample S8. ....	104

Appendix Figure	Page
Figure A24 - Histogram of nanoparticle diameters at 0.4 nm film thickness of Sample S8 segmented by core-shell structure.....	105
Figure A25 - Histogram of nanoparticle diameters at 0.5 nm film thickness of Sample S8. ....	105
Figure A26 - Histogram of nanoparticle diameters at 0.5 nm film thickness of Sample S8 segmented by core-shell structure.....	106
Figure A27 - Histogram of nanoparticle diameters at 0.6 nm film thickness of Sample S8. ....	106
Figure A28 - Histogram of nanoparticle diameters at 0.6 nm film thickness of Sample S8 segmented by core-shell structure.....	107
Figure A29 - Histogram of nanoparticle diameters at 0.7 nm film thickness of Sample S8. ....	107
Figure A30 - Histogram of nanoparticle diameters at 0.7 nm film thickness of Sample S8 segmented by core-shell structure.....	108
Figure A31 - Histogram of nanoparticle diameters at 0.8 nm film thickness of Sample S8. ....	108
Figure A32 - Histogram of nanoparticle diameters at 0.8 nm film thickness of Sample S8 segmented by core-shell structure.....	109
Figure A33 - Histogram of nanoparticle diameters at 0.9 nm film thickness of Sample S8. ....	109
Figure A34 - Histogram of nanoparticle diameters at 0.9 nm film thickness of Sample S8 segmented by core-shell structure.....	110
Figure A35 - Histogram of nanoparticle diameters at 1.0 nm film thickness of Sample S8. ....	110
Figure A36 - Histogram of nanoparticle diameters at 1.0 nm film thickness of Sample S8 segmented by core-shell structure.....	111
Figure A37 - Histogram of nanoparticle diameters at 0.4 nm film thickness of Sample T9. ....	111
Figure A38 - Histogram of nanoparticle diameters at 0.4 nm film thickness of Sample T9 segmented by core-shell structure. ....	112

Appendix Figure	Page
Figure A39 - Histogram of nanoparticle diameters at 0.5 nm film thickness of Sample T9.....	112
Figure A40 - Histogram of nanoparticle diameters at 0.5 nm film thickness of Sample T9 segmented by core-shell structure.....	113
Figure A41 - Histogram of nanoparticle diameters at 0.6 nm film thickness of Sample T9.....	113
Figure A42 - Histogram of nanoparticle diameters at 0.6 nm film thickness of Sample T9 segmented by core-shell structure.....	114
Figure A43 - Histogram of nanoparticle diameters at 0.7 nm film thickness of Sample T9.....	114
Figure A44 - Histogram of nanoparticle diameters at 0.7 nm film thickness of Sample T9 segmented by core-shell structure.....	115
Figure A45 - Histogram of nanoparticle diameters at 0.8 nm film thickness of Sample T9.....	115
Figure A46 - Histogram of nanoparticle diameters at 0.8 nm film thickness of Sample T9 segmented by core-shell structure.....	116
Figure A47 - Histogram of nanoparticle diameters at 0.9 nm film thickness of Sample T9.....	116
Figure A48 - Histogram of nanoparticle diameters at 0.9 nm film thickness of Sample T9 segmented by core-shell structure.....	117
Figure A49 - Histogram of nanoparticle diameters at 1.0 nm film thickness of Sample T9.....	117
Figure A50 - Histogram of nanoparticle diameters at 1.0 nm film thickness of Sample T9 segmented by core-shell structure.....	118
Figure A51 - Average particle size by segmented populations. Core-shell structures are generally larger than non-core shell particles and the difference becomes greater at increasing film thicknesses.....	118

## ABSTRACT

Saber, Sammy M. Ph.D., Purdue University, May 2015. Investigations of Carbon Nanotube Catalyst Morphology and Behavior with Transmission Electron Microscopy. Major Professor: Dr. Eric A. Stach.

Carbon nanotubes (CNTs) are materials with significant potential applications due to their desirable mechanical and electronic properties, which can both vary based on their structure. Electronic applications for CNTs are still few and not widely available, mainly due to the difficulty in the control of fabrication. Carbon nanotubes are grown in batches, but despite many years of research from their first discovery in 1991, there are still many unanswered questions regarding how to control the structure of CNTs. This work attempts to bridge some of the gap between question and answer by focusing on the catalyst particle used in common CNT growth procedures. Ostwald ripening studies on iron nanoparticles are performed in an attempt to link catalyst morphology during growth and CNT chirality (the structure aspect of a nanotube that determines its electrical properties). These results suggest that inert gas dynamics play a critical role on the catalyst morphology during CNT growth. A novel method for CNT catalyst activation by substrate manipulation is presented. Results of this study build upon prior knowledge of the role of the chemistry of the substrate supporting CNT catalysts. By bombarding sapphire, a substrate known to not support CNT growth, with an argon ion beam, the substrate is transformed into an active CNT growth support by modifying both the

structure and chemistry of the sapphire surface. Finally, catalyst formation is studied with transmission electron microscopy by depositing an iron gradient film in order to identify a potential critical catalyst size and morphology for CNT growth. A relationship between catalyst size and morphology has been identified that adds evidence to the hypothesis that a catalysts activity is determined by its size and ability to properly reduce.

## CHAPTER 1. INTRODUCTION

### 1.1 Introduction / Motivation

Moore's law, first observed in 1965, describes the general trend that the number of transistors in central processing units seems to double about every two years<sup>1</sup>. Once observed as a general trend, it is now used as a benchmark to guide future research<sup>2</sup>. However, generally, current technology is beginning to hit a wall with regards to miniaturization<sup>3</sup>.

This is a problem that is shared with most electronic devices. As the world faces the need to process larger amounts of data and harness larger amounts of energy, our technology needs are forced towards the nanoscale. The nanoscale is special in that at these small dimensions, quantum effects arise and surface chemistry plays a far more important role. Utilizing devices with nanoscale structure allow us to process data faster, utilize less energy, and increase the effectiveness or efficiency of devices that depend on surface area.

One potential solution to further minimize electronics is utilizing carbon nanotubes (CNT)<sup>4</sup>. These small, one-dimensional materials have interesting and desirable properties. Despite having diameters on the order of a few nanometers, CNTs have extremely high

Young's Moduli and tensile strength<sup>5-8</sup>. In addition, they have unique electrical properties<sup>9-11</sup>, which can be used for a range of applications<sup>12</sup>.

## 1.2 Carbon Nanotubes

Carbon nanotubes are one-dimensional structures that can be described as sheets of graphene rolled into tubes<sup>13</sup>. These unique materials are interesting due to their unique mix of properties, as discussed earlier. While the Young's modulus can remain somewhat constant, a CNT's electrical properties may vary and are determined by its structure<sup>14</sup>.

The structure of a CNT is defined by its chiral vector  $(n,m)$ . This chiral vector is laid out on a sheet of graphene that defines a CNT's circumference. There are three categories of CNT structures: armchair, zigzag, and chiral. Armchair CNTs are defined by a chiral vector  $(n,n)$  where  $n = m$  in the standard notation. Visually, these CNTs are defined by a chiral vector which falls along the sides and through the centers of the hexagons within the graphene structure. This results in an armchair-like pattern in the CNT structure along the diameter of the CNT. Zigzag CNTs are defined by the chiral vector  $(n,0)$  or  $(0,m)$ . The name, once again, describes the pattern of the carbon bonds in the CNT structure observed along the diameter of the CNT, perpendicular to the length. Lastly, chiral CNTs are defined as all other CNTs with chiral vector  $(n,m)$  that cannot be defined as armchair or zigzag<sup>15</sup>.

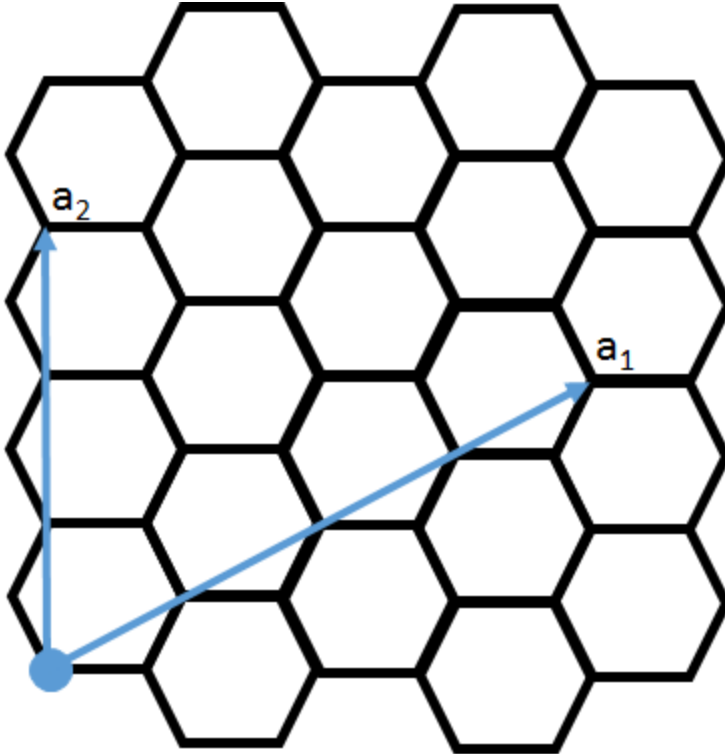


Figure 1 - Diagram of a graphene sheet with the vectors,  $a_1$  and  $a_2$ , defining the circumference of a carbon nanotube,  $C = na_1 + ma_2$ , where  $C$  is the circumference and  $n$  and  $m$  are integers greater than 0.

Electrical properties of CNTs can vary quite drastically, with some CNTs exhibiting metallic behavior while others act as semiconductors<sup>14</sup>. Their chiral vectors determine the distinction in electrical properties between these tubes. Carbon nanotubes with chiral vectors such that  $n = m$  exhibit metallic electrical behavior. So, all armchair CNTs act as metals, electrically. However, if a CNT has a chiral vector such that  $n - m$  is a multiple of three, then the CNT will act as a semiconductor with a small bandgap. Sometimes this bandgap can be small enough that there is little distinction between it and a metallic CNT. All other CNTs exhibit semiconducting electrical behavior<sup>15</sup>. The drastic difference between CNTs' electrical properties simply based on their structure highlight the



importance of finding ways to either grow, or process through filtering, CNTs of specific chirality.

In addition to variations in chirality, there exist two other classifications of CNTs, single-wall<sup>16,17</sup> and multi-wall. Single-wall carbon nanotubes (SWNT), as the name suggests, are CNTs that have a wall thickness of one layer of carbon atoms. Multi-wall carbon nanotubes (MWNT) are larger CNTs that are made up of multiple concentric CNTs. Multi-walled CNTs have their uses, but for the purposes of semiconducting applications as described in the previous section, SWNTs are preferred, simply due to the reliability of their electrical properties<sup>18-21</sup> and theoretical ease of structural control during growth. A MWNT, for example, could consist of a mixture of metallic and semiconducting CNTs. In this case, its mechanical properties would be the result of some combination of its parts, any potentially desirable semiconducting behavior could be shorted by the presence of a concentric metallic CNT, and MWNTs are generally larger which limit benefits arising from the one-dimensionality of the tube<sup>21</sup>.

## CHAPTER 2. CNT GROWTH

There are a number of ways to grow CNTs. Methods such as arc discharge<sup>4,22</sup>, laser ablation<sup>23,24</sup>, and chemical vapor deposition (CVD)<sup>25-30</sup> have all proven to be effective methods of producing CNTs. Despite years of research since CNTs were famously identified in 1991, there remain many unanswered or incompletely answered questions regarding the process of CNT growth, such as: What is the mechanism of growth termination? What is the catalyst composition and morphology during growth and how does that impact the structure of the grown CNTs? What is the role of water or oxygen with respect to the catalyst during growth? And, last, but not least how can chirality be controlled during growth? The reason these questions are so complicated to answer is due to the dynamic nature of growth, and the interconnectedness of the available variables to control during growth.

### 2.1 Chemical Vapor Deposition

Currently, the most popular method of CNT growth is CVD due to the potential scalability for manufacturing<sup>31</sup>, growth at up to atmospheric pressure or higher, and the ability to grow at relatively lower temperatures<sup>32</sup> and in-place (*i.e.* control the location of growth)<sup>33</sup>. The process of growing CNTs through CVD starts with catalyst particles, usually made up of some transition metal, which are heated on a substrate while a carbon

precursor, a small amount of water, and a delivering gas are passed over the catalysts. The catalysts break down the carbon precursor and are able to assemble the carbon atoms in a structured manner that results in a CNT. However, the process of CNT growth is not very well understood. There are reports of wide variations in CNT quality, length, and chirality. In addition, CNT growth is not very efficient in that only a small percentage, ~10%, of catalysts actually nucleate CNTs. These problems faced are likely due to the current limits of our understanding and the inability to control the direct mechanisms of CNT growth, but instead, control higher order factors such as temperature, pressure and initial catalyst size.

## 2.2 Catalysts

There are many choices of materials for growing CNTs. However, metals appear to be the most effective, specifically Fe<sup>34-39</sup>, Co<sup>40-42</sup>, and Ni<sup>43-45</sup>. These transition metals seem to be the most effective due to several properties, including their high carbon solubility and diffusion rate at higher temperatures<sup>46</sup>. However, growth has not been limited to these catalyst materials and has been shown in gold<sup>47</sup>, tungsten<sup>48</sup>, oxides<sup>49</sup>, and alloys<sup>50</sup>.

In addition, recent studies have suggested that their adhesion to carbon is important. Ding et al.<sup>51</sup> used first principles calculations to show that in addition to the normal catalyst function of cracking the carbon precursor gasses and nucleating CNTs, the catalyst also is required to have strong carbon adhesion for SWNT growth. As a SWNT is growing, if the adhesion between the carbon dangling bonds and the catalyst is not sufficient, the CNT will separate and form a cap, either forming a very short CNT or a structure more

similar to a ball than a tube. Coincidentally, this study showed that the elements that had the highest carbon adhesion were Fe, Co, and Ni. In addition, these metals also have a relatively high melting point and low equilibrium vapor pressure<sup>46</sup>, which means that CNTs can be grown at a wide range of temperatures without fear of catalyst loss through boiling or sublimation.

There are multiple methods for catalyst preparation for growth. Commonly, thin films are deposited through atomic layer deposition (ALD), electron beam evaporation or sputter deposition. Catalysts may also be prepared by creating solutions of dissolved nanoparticles and then dipping a substrate into the solution. When preparing catalysts through film deposition, it is important to carefully choose the film thickness as it is directly related to catalyst size. Thicker films, when reduced, result in larger particles. In addition, CNT growth is a highly sensitive process, and small changes in surface chemistry can affect growth results. Amama et al.<sup>52</sup> found that different methods of preparing alumina as a support for iron catalysts resulted in different growth behaviors.

When preparing catalysts through film deposition, then the film must be broken up into nanoparticles. This is done by exposing the film to a heated reducing environment. The state of the catalyst prior to CNT growth is important and there is a diverse set of data suggesting many different kinds of catalysts for CNT growth. For example, the most popular assumption is that active catalysts are in a pure metallic state<sup>38,53</sup>. However, CNT growth from iron carbide has also been observed.<sup>54,55</sup>

The catalyst morphology during growth is also the subject of debate. Harutyunyan et al.<sup>56,57</sup> assert that the catalyst is a liquid during growth and solid catalyst particles inhibit the growth of CNTs. The argument for the catalyst being liquid at these temperatures is that as their size becomes very small, there is a suppression of their melting point. Even though bulk iron with a small amount of carbon begins to melt at around 1500°C, well above normal growth temperatures, the fact that catalyst particles are on the order of a few nanometers in diameter pushes the melting point downward. However, direct evidence of an epitaxial relationship has been observed. The definition of epitaxy veers slightly from the classical definition with respect to CNT growth. In this case, epitaxy refers to a situation where the wall(s) of CNTs line up crystalline planes within a catalyst. Rodriguez-Mazano et al.<sup>58</sup> observed the walls of a MWNT lining up well with crystalline planes in a catalyst particle. The images, though, were taken after growth occurred. If growth had occurred from a liquid particle, it is possible that the particle solidified when the temperature was decreased and was seeded by the CNT walls so that there was an epitaxial relationship only after growth occurred. Other evidence exists, however. Chiang and Sankaran<sup>59</sup> grew carbon nanotubes with  $\text{Ni}_x\text{Fe}_{1-x}$  catalysts. By varying the relative amounts of each element, they were able to alter the CNT chirality distribution, independent of size. This means one of two things: 1) either nickel or iron has the ability to preferentially grow CNTs of a certain chirality or 2) changing the relative amounts of nickel or iron in the catalyst slightly alters the crystal structure, enough to influence the growth of certain chiralities. The first explanation falls beyond our current understanding of CNT growth. If catalysts are liquid during growth then a catalyst particle would presumably have a homogenous mixture of iron and nickel. In addition, the ability to

influence chirality in single metallic catalysts such as iron or nickel has always come from altering the growth environment, and is not independent of other growth parameters such as temperature, pressure, substrate, and feedstock gasses.

### 2.3 Substrate

Carbon nanotube growth, as with most parameters, is sensitive to the choice of substrate to support the catalyst particles. The most popular substrate for CNT growth, especially with iron, is alumina,  $\text{Al}_2\text{O}_3$ . Alumina readily supports forest growth with iron. However, iron does not easily grow vertically aligned carbon nanotubes (VA-CNTs) on other substrates. This is likely due to a few reasons. The oxygen in alumina plays active role during growth. As stated earlier, keeping the support material constant, but changing the preparation method alters the nanoparticle behavior and catalytic activity of iron. This result indicates that something about the alumina, either its topography or, more likely, its surface chemistry is affected by preparation method. Alumina also has the ability to restrict iron movement on the surface. This has the effect of limiting Ostwald ripening, a potential cause of growth termination, and it also helps pin the catalyst in place as it grows the CNT. Carbon nanotube forest growth has been shown to be fairly uniform and well aligned. As a CNT grows it produces a force against the growth direction on the catalyst. If the support were not able to pin the catalyst in place, the catalyst would likely migrate around the surface of the substrate and could potentially entangle tubes or even result in no forest growth.

While alumina is the most popular support for growth, other supports are used, even ones that support VA-CNT growth. Quartz and silica are common supports that, in the right conditions, will support forest growth.

#### 2.4 Growth Temperature

In CVD, CNTs may be grown at a range of temperatures from about 500°C up to 1200°C. One of the benefits of CVD is the tunability of this temperature. However, these growth temperatures are mid range compared to other CNT growth methods. For example, arc discharge growth temperatures can be around 4000°C<sup>33</sup>. Temperature affects a few things. First, it can, and likely does, influence the catalyst morphology. It also affects growth rate and CNT quality. At higher temperatures, the kinetic energy of all species are increased and this, in turn, increases the growth rate. After all, CNT growth is and should be thought of as a chemical reaction. Higher temperatures are also associated with CNTs with lower defects. This process is not well understood, but the general assumption is that as CNTs are growing faster at higher temperature, there is a smaller amount of time for defects to occur or grow. It has also been shown that annealing CNTs after growth at high temperatures (about 2000°C) can reduce the number of defects<sup>60</sup>.

#### 2.5 Gasses

There are many choices for gasses to use during CNT growth. The initial annealing and reduction step has already been discussed. This step commonly uses hydrogen or some dilution of hydrogen in a carrier gas, such as helium. During growth, a carbon source is required for the catalysts to use during growth. Common carbon feedstock includes

ethylene ( $C_2H_4$ ), acetylene ( $C_2H_2$ ) or methane ( $CH_4$ ). Each carbon source differs in its total carbon content and the ease with which carbon is mined from its source. When the carbon source is fed under growth conditions, the catalysts break the precursor gas down and a number of different compounds are formed. These include carbon, hydrogen, volatile organic compounds, and polycyclic aromatic hydrocarbons. Ideally, only carbon and hydrogen would be the result of the decomposition, but extra compounds result and it is unclear what role they play during growth. Some compounds are likely carried away as a constant flow of gasses is commonly used during growth, but others are likely deposited around the catalysts or on the surface of the substrate. Very little is understood of this process and elucidating the dynamics of the development of unwanted compounds remains a critical question in understanding CNT growth and its potential implications for growth termination.

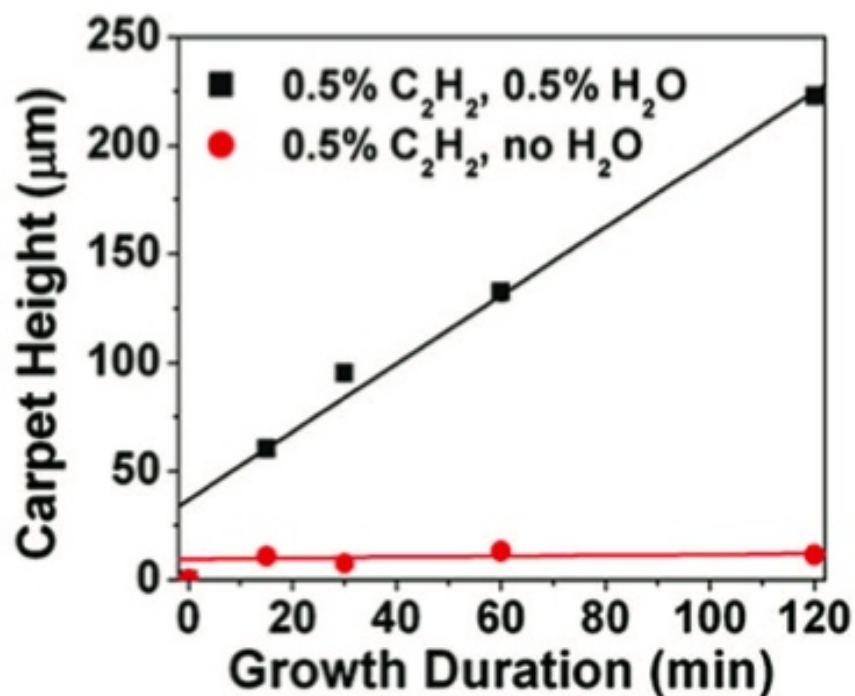


Figure 2 - Height of carpet grown at different times with water and without<sup>62</sup>.



## 2.6 The Role of Water

Hata et al.<sup>61</sup> first showed that introducing a small amount of water during growth assisted in vertically aligned “super growth.” See Figure 2. This result has since been duplicated, and there has been debate about what water does during CNT growth. Work by Amama et al.<sup>62</sup> showed that in hydrogen and water, without the presence of carbon feedstock and, thus, without growth, water inhibited Ostwald ripening. In addition, growth was performed in two separate conditions. First, growth was performed in hydrogen, acetylene and water and then in hydrogen and acetylene, without water. In each case, growth was only performed for 30 seconds. The resulting CNTs were removed by two methods in order to guarantee no effects on catalyst Ostwald ripening trends were due to the CNT liftoff procedures. First, CNTs were removed by catalyst oxidation and liftoff and second, by burning the CNTs off in air. In each case, Ostwald ripening was repressed in the CNT sample grown with water (Figure 3). This was attributed to water and hydroxyl (species resulting from the decomposition of water) adsorbing to the surface of the iron nanoparticles or substrate. Harutyunyan et al.<sup>63</sup> used in-situ TEM to observe the catalyst morphology at elevated temperatures. They found that catalyst particles in the presence of water exhibit strong faceting in helium environments, but became rounded in argon. This work will be discussed more in depth in Chapter 4, as it is the motivation for our work in that chapter. Conclusions were made that the decomposed water adsorbed onto the catalyst led to preferential growth of metallic CNTs, suggesting that the faceting may be related. This is in direct contradiction to Harutyunyan’s earlier work arguing that active catalysts are in their liquid state. This is one example of the complex nature of

CNT growth simply due to the chaotic, dynamic nature of the chemical reaction that is very hard to visualize.

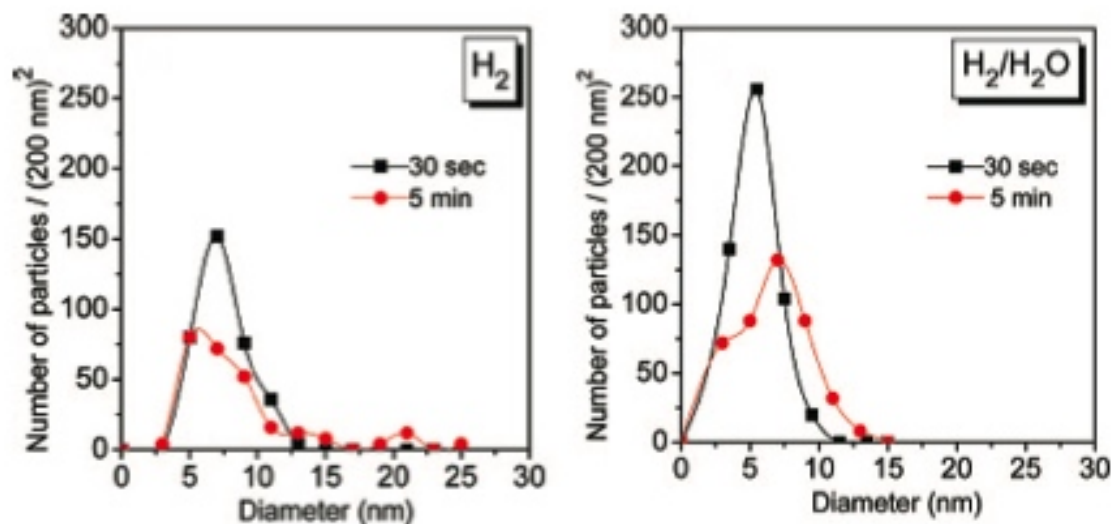


Figure 3 - Histograms of the number of particles after annealing for 30 seconds and 5 minutes in hydrogen (left graph) and hydrogen with water (right graph)<sup>62</sup>.

The second, more widely accepted role of water is to prolong the catalyst lifetime. Many have shown that oxygen (not just from water) acts as a mild oxidizer and is thought to remove unwanted amorphous material from the outside of the catalyst. Pint et al.<sup>64</sup> grew CNTs on the order of millimeters with the use of oxygen, and it has been shown that oxidizing with water was able to restart growth after it had terminated.

## 2.7 Ostwald Ripening

Ostwald ripening is a process of a particle system over a period of time where the total surface area of the particle system decreases. Surfaces are high-energy aspects of materials. This is essentially because atoms at the surface are only half bonded to the bulk

material. So, in Ostwald ripening, large particles grow at the expense of smaller particles to reduce the total surface energy and increase the volume-to-surface ratio, which is greater in larger particles.

The most widely accepted theory for Ostwald ripening behavior was developed independently by Lifshitz and Slyozov<sup>65</sup> and Wagner<sup>66</sup> and later combined into the Lifshitz-Slyozov-Wagner (LSW) model. Ostwald ripening was first developed for colloidal systems where particles are dispersed in a liquid. So, the LSW model assumes infinite dispersity in a solution. This differs slightly from Ostwald ripening in CNT catalyst systems, where the catalysts are dispersed on a solid substrate in the presence of a gas, and atom dissolution occurs by diffusion along the surface of the substrate or, potentially, diffusion through the gas phase.

The LSW model offers two general equations describing particle coarsening in a dispersed system.

$$(1) \quad \langle a_t \rangle^3 - \langle a_0 \rangle^3 = \frac{8D\gamma C_\infty V_m^2 t}{9RT}$$

$$(2) \quad \langle a_t \rangle^2 - \langle a_0 \rangle^2 = \frac{64K\gamma C_\infty V_m^2 t}{81RT}$$

The first describes diffusion controlled Ostwald ripening, where  $\langle a \rangle$  is the average radius for all the particles in the system, the subscripts  $t$  and  $0$  denote the state of the system at time  $t$  and its initial state, respectively,  $D$  is the diffusion coefficient,  $\gamma$  is the surface energy,  $C_\infty$  is the particle material solubility,  $V_m$  is the molar volume,  $R$  is the ideal gas constant,  $T$  is temperature, and  $t$  denotes time. The second equation, where  $K$  is a constant

taking surface mobility into account, describes Ostwald ripening controlled by interface reactions. The main difference between the two equations is that the first assumes spherical particles and the second assumes that the particles have facets which control how atoms move along those facets. In the latter, Ostwald ripening is limited by atomic diffusion along facets. In each situation, however, the behavior remains the same. As time increases, the average particle size increases, the number of particles decreases as small particles completely dissolve, and the spread in particle size increases as large particles grow bigger and small particles decrease in size.

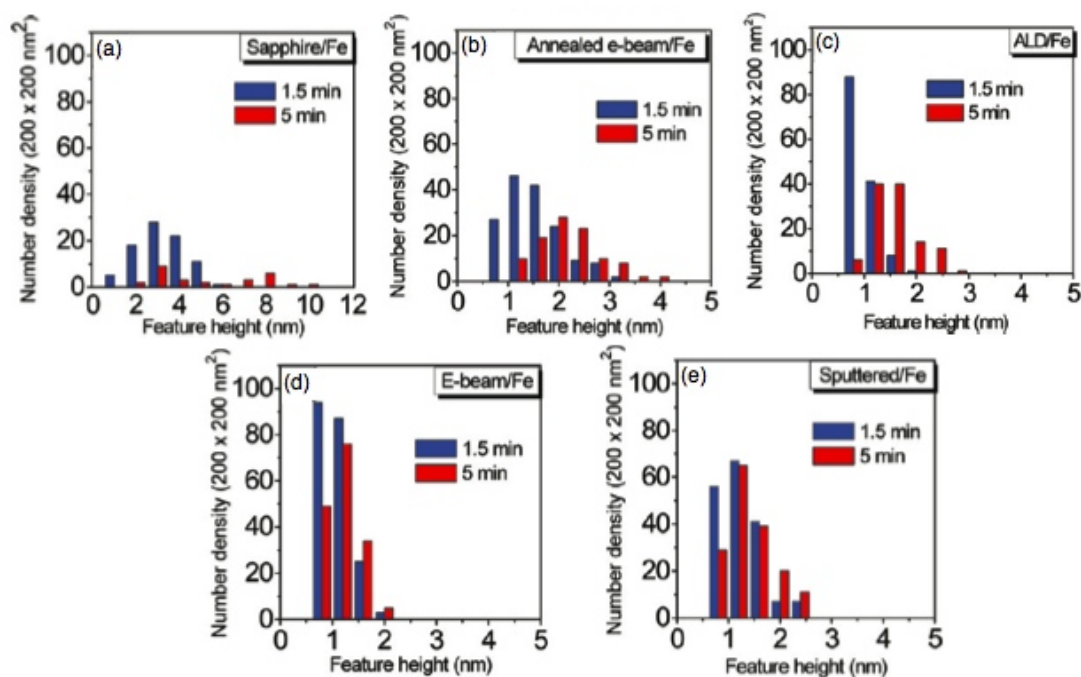


Figure 4 - Histograms of particle size after annealing for 1.5 and 5 minutes on (a) sapphire, (b) annealed e-beam alumina, (c) ALD alumina, (d) e-beam alumina, and (e) sputtered alumina<sup>52</sup>.

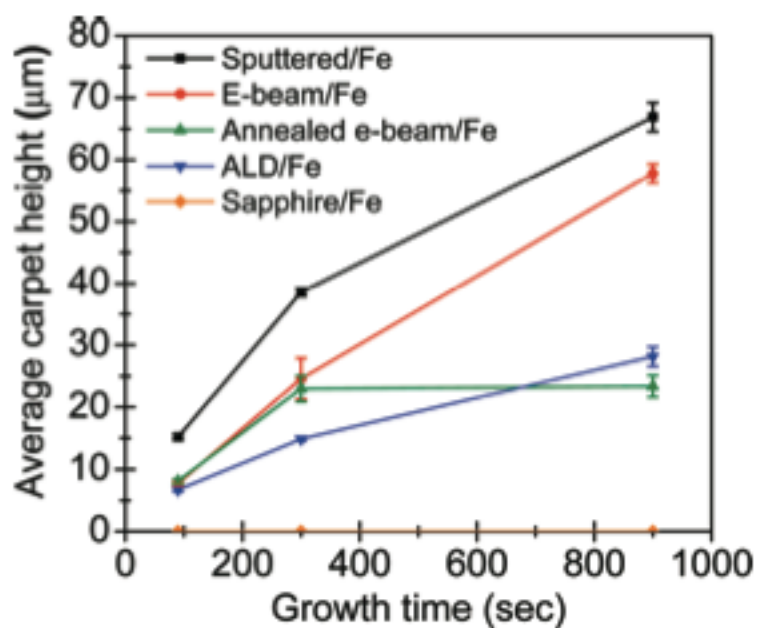


Figure 5 - Graph of CNT carpet height with respect to growth time for sapphire and sputtered, e-beam, annealed e-beam, and ALD alumina<sup>52</sup>.

Ostwald ripening is a critical area of study with respect to CNT growth due to its impact on particle size for CNT diameter control, but also its role during growth and its potential impact on termination of growth. As discussed earlier, work by Amama<sup>62</sup> showed direct evidence of the ability of water to inhibit Ostwald ripening. Further work by Amama focused on the effects of alumina preparation on CNT growth<sup>52</sup>. The study compared sapphire, sputtered, e-beam deposited, annealed e-beam deposited, and ALD alumina and found different results in CNT growth from almost every substrate (Figure 4). Sapphire did not support any growth, ALD and annealed e-beam deposited alumina supported a small amount of growth, and sputtered and e-beam deposited alumina supported the best growth (Figure 5). Interestingly, the growth results inversely correlated with the Ostwald

ripening behavior of iron on the different substrates. This supports the hypothesis that Ostwald ripening is a mechanism of CNT growth termination. Furthermore, this adds to the evidence that the chemical interaction between catalyst and support is critical in the successful growth of VA-CNTs.

While not exactly Ostwald ripening, Kim et al.<sup>67</sup> showed that subsurface diffusion coupled with Ostwald ripening is another critical mechanism of CNT growth termination. Ostwald ripening studies of iron on alumina found little correlation between Ostwald ripening theory and experimental behavior past an anneal time of 5 minutes. Cross-sectional TEM was performed on samples annealed in hydrogen and water. Images showed that iron had diffused into pores within the alumina support layer. This diffusion is driven by the reduction of the total system energy by reducing surface area, similar to Ostwald ripening. Iron clusters on the surface of the catalyst support have dangling bonds from the surface area, which is exposed to the gas flow during growth. Iron clusters within the pores of the support have a higher coordination due to the ability to bond to the support, which completely surrounds the particle.

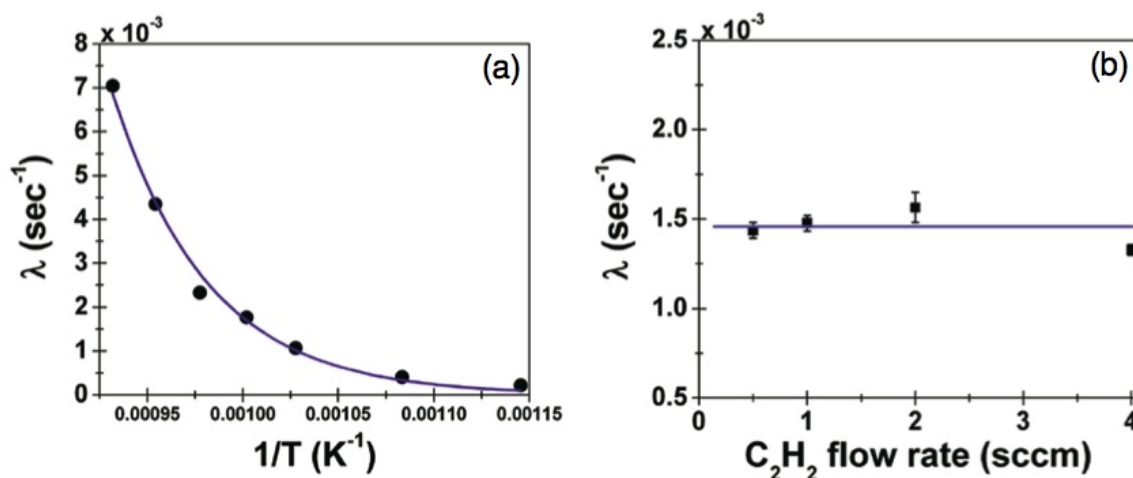


Figure 6 - Catalyst decay rate measured versus (a) inverse temperature and (b) acetylene flow rate.

Going one step further, growth kinetics were studied by analyzing the catalyst decay rate parameter  $\lambda$  to test for its dependence on temperature and carbon precursor, shown in Figure 6. Fitting with Ostwald ripening theory, the catalyst decay rate shows a strong dependence on temperature, decaying faster with increasing temperature. The logarithmic decay in Figure 6a indicates that Ostwald Ripening is consistent with the Arrhenius relationship,  $k = Ae^{-E_a/(RT)}$ , which states that a rate constant,  $k$ , is equal to some constant,  $A$ , multiplied by the exponential of the activation energy of the process,  $E_a$ , divided by the ideal gas constant multiplied by temperature,  $T$ . In this case, the slope of the line resulting from the log of Figure 6a would be equivalent to  $-E_a/(RT)$ . This makes sense as increasing temperature increases kinetic energy, and, thus, iron mobility within the catalyst particles. In addition, there is no dependence of the catalyst decay rate on acetylene flow.

These catalyst decay rate tests were performed by using square wave pulses of acetylene through the growth chamber. By using pulses rather than a constant flow, the amount of growth between each pulse could be measured and, thus, characterization of the growth kinetics could be performed.



## CHAPTER 3. CHARACTERIZATION TECHNIQUES

### 3.1 Electron Microscopy

Microscopes are unique and critical tools in the study of our environment and we use them primarily because they allow us to see objects or features that the naked eye would otherwise be unable to perceive. When studying the nanoscale, it is often necessary to be able to visualize the nanoscale features of materials that are important. This creates a unique problem because spatial resolution, the measure of how closely features can be together while remaining discernable, is dependent on the wavelength of light being utilized.

The primary focus of this dissertation is on the utilization of electron microscopy to study material properties and dynamic phenomena related to carbon nanotube growth. For this reason, the following discussion will be focused on the brief explanation of the theory, operation, and techniques essential to the use of transmission electron microscopy (TEM), the primary tool used for these studies.

The German physicist, Ernst Abbe, approximated the resolution of microscopes to follow the formula  $d = \frac{\lambda}{2n \sin \theta}$ , where  $d$  is the resolution,  $\lambda$  is the wavelength of the radiation,  $n$  is the refractive index of the observable medium, and  $\theta$  is the half opening angle of the

lens. Making some general assumptions about a light microscope where  $n = 1.5$ , a common refractive index for immersion lenses,  $\theta = 70^\circ$ , and  $\lambda = 400$  nm, the approximate wavelength of violet light, the maximum resolution for a light microscope comes out to about 142 nm. However, compared to some rough numbers for a 300 keV TEM, like the FEI Titan 300 keV Environmental TEM used in these studies, with  $n = 1$  for a vacuum,  $\sin \theta = 0.01$  using the low angle approximation and  $\lambda = 1.97 \times 10^{-3}$  nm, the resolution is approximately 0.10 nm. This is a significant resolution limit as it is below the lattice constant spacing of many materials, including the interatomic spacing of carbon, which is 0.142 nm. It should be noted that the energy transmitted to carbon from a 300 keV electron beam is too much to allow the carbon structure to remain intact. However, TEMs can be operated at 80 keV which allows the imaging of carbon without damage<sup>68</sup>.

Transmission electron microscopy is a unique characterization tool in that it uses plane wave electrons to image samples, which are extremely thin (less than 100 nm) and transparent to electrons. In a transmission electron microscope, electrons are emitted one-at-a-time from a source, collimated by a series of electromagnetic lenses, interact with a sample, and then are magnified and projected onto a viewing screen, typically a charge-coupled device (CCD)<sup>68</sup>. Other common forms of high-resolution microscopy such as atomic-force microscopy (AFM) or scanning electron microscopy (SEM) generally image the surface or topography of a sample. However, in this scenario, the electron wave passes through the sample, and, thus, what is seen in TEM images are three-dimensional projections through the thickness of the sample onto a two-dimensional viewing screen<sup>68</sup>.

There are four conditions that can describe the electron wave once it exits the sample: coherent, incoherent, elastic, and inelastic. Coherence refers to the phase of the electron wave. So, an electron passing through a specimen can either keep the phase that it entered the sample with (coherent) or lose its phase relationship with the incident beam (incoherent). Whether scatter is elastic or not refers to the energy of the electron as it leaves the specimen. An electron which scatters elastically has the same energy it did when it entered the sample, but an electron which undergoes inelastic scatter has lost some amount of energy through interaction with the specimen. When the electron wave passes through the sample, it can undergo four different events which all interact to form the image. The beam can pass through the sample without interference, coherently scatter elastically, incoherently scatter elastically, or incoherently scatter inelastically. Coherent inelastic scattering may occur; however, it will only likely occur at higher angles, and, therefore, does not affect the image. These are all examples of forward scatter. Back scattering can occur, meaning the electron can bounce backward toward the direction from which it came; however, only forward scatter influences the resulting image<sup>68</sup>.

Forward scatter is what makes up the forms of TEM imaging techniques, and will underline the following discussion on electron diffraction: bright-field TEM, dark-field TEM, high-resolution TEM (HRTEM), and energy filtered TEM (EFTEM).

One useful tool in the TEM to characterize the structure of a material is electron diffraction. When discussing electron diffraction in the TEM it is useful to reference the discussion of classical Bragg diffraction. Bragg diffraction describes reflection of

electromagnetic waves off of planes of atoms. This is illustrated in the simple formula  $n\lambda = 2d \sin \theta$ , where  $n$  is an integer,  $\lambda$  is the wavelength of the wave,  $d$  is the distance between planes of atoms, and  $\theta$  is the incident angle. This equation essentially describes the specific set of conditions for diffraction to occur. Specifically, the distance between planes of atoms multiplied by the sine of the incident angle must be equal to a multiple integer of the wavelength of the incident wave. So, if the condition is met, constructive interference occurs and a diffraction event is observed, otherwise there is destructive interference off of the planes of atoms and no diffraction is observed. At a higher level, diffraction in crystallography is often described by the Laue equation,  $k_0 - k_i = \Delta k$ , where  $k_0$  is the exiting wavevector,  $k_i$  is the incident wavevector and  $\Delta k$  is the difference vector. However, this just essentially describes Bragg diffraction in three dimensions. In practice, an incident electron wave will encounter a crystalline specimen within the TEM and undergo diffraction events off any set of periodic planes within a sample. Projected onto the CCD, what is observed is a two-dimensional array of diffraction spots. If a specimen's crystal structure is known and it is tilted properly to a zone axis, an orientation of a crystalline material by which multiple sets of lattice planes align along the observed direction, then it is possible to identify the zone axis from the diffraction pattern<sup>68</sup>.

It may be useful at this point to discuss how to find a zone axis of a specimen within the microscope. During the sample preparation process, it is useful to understand the rough orientation of the material and prepare a TEM sample such that the thickness of the sample is as close to parallel to a zone axis of interest. However, the level of precision

during the sample preparation process can only reliably achieve about  $\pm 5 - 10\%$  from the zone axis. When the kind of diffraction work is performed that requires a zone axis be reached, a double tilt sample holder is used. This allows the specimen to tilt in two perpendicular directions, which are commonly labeled  $\alpha$  and  $\beta$ . The  $\alpha$  tilt tilts the specimen around the axis of the specimen holder and the  $\beta$  tilt tilts the specimen perpendicular to that axis. To observe the exact tilt of the specimen, a convergent beam electron diffraction pattern (CBED) is utilized. To obtain a CBED pattern, the electron beam is collapsed to a small point and positioned over an area of interest. Then the microscope is put in diffraction mode. What is then observed is a diffraction pattern from the specimen using many  $k_i$  wave vectors over a spread of incident angle  $\theta$ . This differs from a standard two-beam diffraction pattern, which, instead, spreads the beam to obtain as parallel illumination as possible so as to only sample one  $k_i$  wave vector. If  $\theta$  is large enough, what is observed on the viewing screen is called a Kossel pattern (if observing a crystalline specimen). A diffraction pattern may also display Kikuchi diffraction, pairs of diffraction lines forming bands that arise from incoherent electron scatter. These Kikuchi diffraction patterns act as stereographic maps in diffraction (reciprocal) space. We can use them to find zone axes of sample by finding areas where these bands formed by Kikuchi diffraction intersect<sup>68</sup>.

Bragg diffraction describes crystalline diffraction. However, sometimes amorphous materials are observed in the TEM. Diffraction from amorphous materials is a little simpler. Due to the lack of long-range order, or even short-range order, little destructive interference occurs. Instead, diffraction occurs in all  $(x,y)$  directions equally and decays

as it moves away from the central spot. What is observed is a circular disk. Observing this pattern can confirm the amorphous nature of a material by not observing any diffraction off of a periodic set of ordered planes, but also allows the user to correct for any astigmatism within the image from the objective lens of the microscope. This correction is often viewed in real time by observing the fast Fourier transform (FFT) of the live image being observed. One of the beauties of mathematics which relate to the physical world is that the Fourier Transform ( $\hat{f}(\xi) = \int f(x) e^{-2\pi i x \cdot \xi} dx$ ) of an image is the diffraction pattern of that image. Conversely, the inverse Fourier transform of a diffraction pattern is an image<sup>68</sup>.

A standard TEM image, formed from the forward scattered electron beams, shows contrast primarily due to mass-thickness and diffraction contrast. Mass-thickness contrast is contrast created by incoherent elastic scattering within the specimen. Simply put, a region of the specimen that is thicker, but has the same density (*i.e.* atomic number,  $Z$ ) as the rest of the specimen will scatter electrons more due to the longer travel distance. Also, a region of the specimen that has a higher density, but the same thickness as the surrounding area will diffract more due to the fact that higher  $Z$  materials have more electrons and a larger nucleus. Figure 7 illustrates an example of this thickness contrast behavior. Imaged on a silicon nitride sloped wall, the image appears darker over areas of the sample that are thicker, and light and dark bands appear due to the effect of the extinction distance of the electron beam through the specimen<sup>68</sup>.

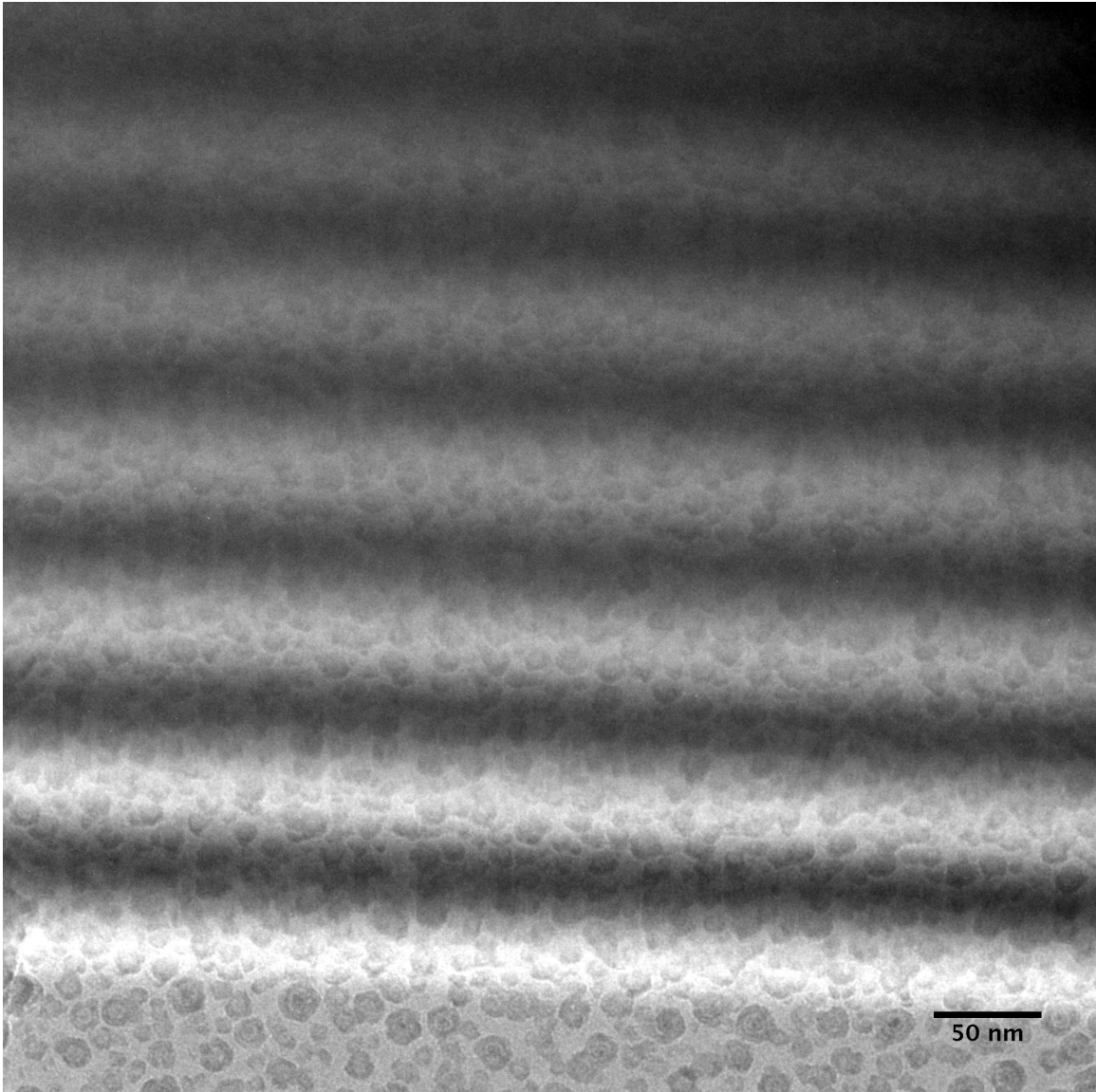


Figure 7 - TEM image over the wedge-shaped edge of a SiN TEM window. The dark and light bands running horizontally across the image are thickness fringes with the thicker region of the sample at the top of the image and the thinner region of the sample at the bottom. Note that this is a standard TEM image and was not taken in a two-beam condition, thus illustrating the power of the two-beam condition approximation.

Diffraction contrast occurs in TEM images due to coherent elastic scatter. This happens when a diffraction event occurs within the specimen and the incident electron is diffracted to a large enough angle that it is not collected by the CCD detector. There are

useful techniques to accentuate this contrast within the TEM. Specifically, this is accomplished through the use of an objective aperture to create bright-field and dark-field images. In bright-field and dark-field images, an objective aperture is placed in the back focal plane of the microscope. This is commonly performed by inserting a selected area diffraction (SAD) aperture over the intermediate image, centering the SAD aperture on the area of interest, spreading the intensity of the beam to achieve parallel illumination of the area of interest, and switching the microscope to “diffraction mode” so as to view the diffraction pattern. Once the diffraction pattern is projected on the viewing screen, an objective aperture is placed in the back focal plane of the microscope. While in “diffraction mode,” the position of the objective aperture may be viewed and centered on the diffraction spot of interest. A bright-field image is created by centering the objective aperture on the central transmitted beam along the optic axis. In this scenario, the image obtained will be made entirely from electrons that have not undergone any diffraction event, simply speaking. It is possible for an electron to undergo multiple diffraction events within the specimen and end up back in the central spot as if it had not diffracted at all. In a bright-field image, bright areas indicated areas of the specimen where the beam has simply passed through and dark contrast in the image is intensity that has been removed from the image by physically blocking it with an objective aperture<sup>68</sup>.

Converse to a bright-field image is a dark field image, where, instead of centering the objective aperture around the central spot, the objective aperture is centered around one of the diffracted spots. In a two-beam condition (which will be discussed soon), bright-field and dark-field images are essentially inverse images in the two-beam condition



because in a dark-field image, the bright areas indicate regions of the specimen where a diffraction event from a specific set of planes occurred and dark contrast in the image is intensity that has been removed from the image by the objective aperture<sup>68</sup>.

There are two ways to create a dark-field image. A dirty dark-field image is made by moving the objective aperture to the diffraction spot of interest. However, a proper dark-field image is made by centering the objective aperture along the optic axis and then tilting the beam so that the diffraction spot of interest is shifted to the optic axis. The latter method keeps the diffracted beam aligned with respect to the microscope and the CCD. Dark-field images are often preferred when observing defects, as they tend to show defects such as dislocations more prominently than bright-field or normal TEM images<sup>68</sup>.

There are ways to further optimize dark-field imaging, by physically tilting the specimen to create what is called a two-beam condition. From here, it is useful to discuss bright-field and dark-field imaging in reciprocal space, since the sample is being manipulated with respect to its diffraction pattern. In reciprocal space, this excited Bragg reflection is referred to as  $\mathbf{G}$  and the central transmitted spot is referred to as  $\mathbf{O}$ . The vector from  $\mathbf{O}$  to  $\mathbf{G}$  is referred to as  $\mathbf{g}$ . Once  $\mathbf{g}$  has been defined, this limits the discussion to the linear set of spots along the line defined by  $\mathbf{O}$  and  $\mathbf{G}$ . All other spots and vectors along this line are referred to as integer multiples of  $\mathbf{G}$  and  $\mathbf{g}$ . In a zone axis diffraction pattern, the central spot (transmitted beam) is the brightest and the array of diffracted spots have lower intensity and decrease as they get farther away from the central spot. When a two-beam condition is made, the sample is tilted such that one diffraction spot of interest ( $\mathbf{g}$ , usually

a nearest neighbor to the transmitted beam) is excited and displays a higher intensity than its surrounding diffracted spots. Ideally, it should approach the intensity of the central spot. In this setup, the majority of the electron beam is either being transmitted through the specimen or undergoes a diffraction event from a single set of crystallographic planes. From here, there are two common kinds of dark-field images that may be used. Once the two-beam condition is set up, a dark-field image may be taken by tilting the beam so that  $-\mathbf{G}$  is on the optic axis. Tilting the beam such that  $-\mathbf{G}$  is on the optic axis will excite that the  $-\mathbf{G}$  Bragg reflection and an objective aperture can be inserted around this spot to collect the dark-field image and block all other forward scattered beams. The second kind of dark-field image that may be taken is called a weak beam dark-field (WBDF) image. Tilting the beam so that  $\mathbf{G}$ , the originally excited Bragg reflection, is on the optic axis, sets up a WBDF condition. However, when this happens,  $\mathbf{G}$  will fade and  $3\mathbf{G}$  will become excited. A WBDF image is taken by inserting an objective aperture around this faded  $\mathbf{G}$  beam. Weak beam dark-field images are usually desirable because they show strong contrast around defects within materials<sup>68</sup>.

At a slightly higher level, in a two-beam condition, not only should the sample be tilted such that the diffracted beam  $\mathbf{G}$  is strongly excited, but it should be tilted such that the deviation parameter  $\mathbf{s}_g$  is slightly greater than zero. The deviation parameter is a measure of how far away  $\mathbf{G}$  is from the exact Bragg condition. This may be geometrically visualized by the concept of the Ewald sphere. The Ewald sphere is defined as the sphere in reciprocal space with a radius of the wave vector of the incident electron wave. When the Ewald sphere intersects a Bragg reflection or its reciprocal lattice rod (an extension of

the Bragg condition due to the three-dimensional planar structure of the sample), a diffraction spot will appear<sup>68</sup>.

Electrons that scatter inelastically usually do so by interaction with the electrons within the sample. In addition, the energy lost in the incident electron wave by interaction with the specimen is often directly related to the discrete energy levels of the electrons within the specimen. This is an extremely powerful concept because it means that if the resulting exit wave (the modulated electron wave as it leaves the specimen) can be segregated by the different energies it contains, then chemical information about the specimen can be determined (*i.e.* elements present and valence state). In practice, some TEMs, as in the case of the FEI Titan ETEM at Purdue University, are equipped with a magnetic prism lens that the exit wave passes through before hitting the CCD. A slit may then be placed in between the path of the exit wave after it passes through the prism and the CCD. This slit allows electrons of only a specific energy gap through. There are two imaging techniques that can be utilized in this setup, electron energy loss spectroscopy (EELS) and EFTEM. Electron energy loss spectroscopy uses wide slits and collects spectra from anywhere the beam interacts with the specimen. Unless, in STEM mode where the electron probe is condensed to a point generally smaller than the atomic spacing, spatial resolution is extremely low, but the shape of peaks can be observed. In EFTEM mode, a smaller slit is used so as to only measure a specific elemental peak and increase the spatial resolution, making an elemental map where bright intensity indicates the presence of the element being searched<sup>68</sup>.

Phase-contrast imaging can take place at very high resolution, where it may be possible to visualize the atomic structure of the material being imaged. Phase-contrast imaging occurs at all magnifications of a specimen; however, it competes with amplitude contrast for dominance in the contrast of an image. At high magnification, we work under the assumption that the sample is a weak-phase object. This essentially means that variations in the intensity of the resulting image are directly related to the potential of the specimen. This means that as the incident electron wave passes through a small area of a specimen, it will be modulated differently depending on whether it passed through a column of atoms or the space between the columns. This difference gives rise to high resolution and the ability to visualize individual columns of atoms within the TEM. High-resolution images require high spatial frequencies. Spatial frequencies refer to periodicity within a crystalline specimen. This means that it is near impossible to be able to visualize a single column of atoms, rather many columns of atoms with adding degrees of periodicity are required to visualize high-resolution images. Directly interpreting these images can be tricky, however, because the contrast that is observed in a HRTEM image is dependent upon the geometry of the specimen (thickness), focal condition of the beam, and spherical aberration. However, for most users, only the specimen thickness (sample preparation) and focal condition can be controlled. Aberration correctors exist for microscopes, however they are not yet the norm. Depending on the focal condition and thickness of a specimen, the contrast observed in an image, the intensity over columns of atoms and the space between them, can vary wildly. Atoms can potentially be black or white. Luckily, the theoretical aspects of this process are fairly well understood, and software exists that can simulate an image based on the thickness or focal condition of

the microscope. The effects of the focal condition and aberration on resolution within a HRTEM image can be represented by what is called the contrast transfer function (CTF). This is a measure of how contrast in the modulated wave is transmitted to the image being viewed. The CTF is a combination of the aperture function and a phase-distortion function which is damped by aberrations within the microscope lenses and the spatial coherence of the electron beam. To maximize the information passed to the image, it is necessary to maximize the area in the CTF. In practice, this is done by choosing a defocus value which maximizes this area. This specific defocus value is called the Scherzer defocus and is given by the equation  $\Delta f_{Sch} = -1.2(C_s\lambda)^{1/2}$ , where  $\Delta f_{Sch}$  is the Scherzer defocus,  $C_s$  is the spherical aberration coefficient, and  $\lambda$  is the wavelength of the electron<sup>68</sup>.

### 3.2 TEM Sample Preparation

Sample preparation is the key to taking good TEM images. Current technology allows for stable electron emission energies, high emission voltages, and noise and sound isolation which make it fairly easy to obtain high-resolution images (all of these being the case for the FEI 300 keV Titan ETEM at Purdue University). However, if a sample is not thin, uniform, and relatively clean of amorphous debris, then it will not be suitable for HRTEM, and, unfortunately, many of our current methods for TEM sample preparation are still highly dependent on skill.

The simplest method for TEM sample preparation involves the use of TEM grids. Grids are readily available and come in a wide variation of sizes, geometries, and support

material. With these available, sample preparation can either be done by some form of physical vapor deposition (such as sputter deposition which was used to prepare the Fe gradient samples) or by dissolving or dispersing a specimen in a fluid (*i.e.* nanoparticles or CNTs) and then placing drops of the fluid onto an organic thin film on a TEM grid.

Preparing plan view or cross-sectional TEM samples is more complex. Plan view samples are prepared by cutting a disk of appropriate size (3.0 mm is standard, but some holders use 2.3 mm samples) and then polishing it until it is around 50 microns thick. Once polished, the sample is placed in a dimple grinder which uses a rotating wheel to grind a dimple in the sample. When complete, the thinnest region of the sample, the bottom of the dimple, should be around 10 microns thick. Lastly, the sample is then placed in an ion polishing system which uses focused ion beams at low angles (typically 1 - 20°) to slowly mill away material and form a small hole in the center of the specimen, usually at the base of the dimple. Once prepared, a user can image the region around the hole, which should be easily less than 100 nm thick. On paper this process can sound quite easy; however, there are a number of variables in the execution of this process that can cause issues, such as pressure applied to the specimen, specimen brittleness, redeposition of material during the ion polishing, and overall human error. When any specimen is prepared by hand to be less than 100 nm thick, extreme care must be taken.

The focused ion beam (FIB) is a tool that is utilized to prepare cross-sectional TEM samples. The FIB is a beam of ions, usually Ga<sup>+</sup>, but sometimes Ar<sup>+</sup>, that is focused and can be used to image, mill, or deposit material. It is common to have dual SEM / FIB

machines as the FIB can be quite damaging to samples, especially at the surface while imaging. If a user is interested in features of the sample that occur near the surface, then imaging with the FIB should be kept to a minimum, and the SEM utilized instead. The procedure for preparing cross-sectional TEM samples with a FIB starts by identifying an area of interest on the specimen. Once chosen, it is common to deposit a thin layer of amorphous Pt (about  $1\ \mu\text{m} \times 10\ \mu\text{m} \times 1\ \mu\text{m}$  thick) to protect the surface of the specimen. The length of this layer can vary depending on the features within the specimen that are of interest. This Pt layer is deposited by focusing the FIB on the area of interest and spraying an organometallic (Pt attached to a hydrocarbon chain) in the path of the beam. The FIB deposits a mix of Pt and C on the surface of the substrate by simple ballistics. Once the protective layer is deposited, the FIB is used to mill trenches on either side of the specimen outline. These trenches are milled deep enough to expose the entire cross-section of the specimen, usually around  $10\ \mu\text{m}$ . What is left is a thin wedge attached to the bulk of the substrate. The FIB is then used to cut one side and the bottom of the specimen free from the bulk sample. Once free, a micromanipulator is brought in and positioned very close to the specimen. Amorphous Pt is once again utilized, but this time to weld the specimen to the manipulator. After the specimen is secured to the manipulator, the FIB is used to cut the remaining side, attaching the specimen to the bulk sample, and the sample is then lifted away from the substrate. Once clear of the substrate, the micromanipulator is used to bring the specimen close to a TEM grid, usually a copper half-circle with a pillar to attach specimens. The specimen is once again welded with amorphous Pt, but this time to the TEM grid. The FIB is then used to cut the specimen free from the manipulator and the manipulator is removed. From here, the final thinning

process begins and the sample is tilted back and forth by about  $1^\circ$  while each side is milled. Once the sample and Pt layer become very thin, the voltage of the FIB is lowered to perform one last thinning step. The purpose of the lower voltage is to reduce the energy of the incident ions and clean away any thin amorphous layers on the side of the specimen that have been created by higher energy ion beam bombardment from the FIB. The specimen is thinned until the protective Pt layer is almost completely removed. A small amount is kept as it allows the TEM user to easily view amorphous material and correct for objective astigmatism.

### 3.3 Raman Spectroscopy

Raman spectroscopy is a common characterization tool, which uses lasers in the visible, or near visible wavelength range to characterize molecules by their vibrational modes of movement. The process relies on inelastic scatter from the species being studied as energy is absorbed and then re-emitted while either shifting the energy of the laser up (Stokes Raman scattering), shifting the energy down (anti-Stokes Raman scattering), or with no shift at all (Rayleigh scattering). The shift in energy of the beam is measured in wavenumbers and is given by the general equation  $\Delta w = \left( \frac{1}{\lambda_0} - \frac{1}{\lambda_1} \right)$ , where  $\Delta w$  is the wavenumber shift,  $\lambda_0$  is the wavelength of the laser being utilized, and  $\lambda_1$  is the wavelength of the measured output<sup>69</sup>.

Carbon nanotubes, based on their hollow tube nature, unique electronic structure based on their diameter and chirality, and corresponding unique phonon states can be discretely



characterized by probing their density of states through Raman spectroscopy. Essentially, singularities within the CNT density of states, called van Hove singularities, occur when the conduction band touches the valence band within the CNT electronic structure. Given that a SWNT has a unique chiral vector and corresponding diameter, the van Hove singularities act like fingerprints. Rather unique to the  $sp^2$  bonding in graphite and SWNTs is that the  $\pi$  band in the electronic structure is close to the Fermi level. For this reason, optical absorption by specific wavelengths of light in Raman spectroscopy can be used to probe the unique electronic structure of SWNTs. Dresselhaus et al.<sup>70</sup> mapped the electron valence to conduction band energy transitions versus the nanotube diameter, as shown in Figure 8.

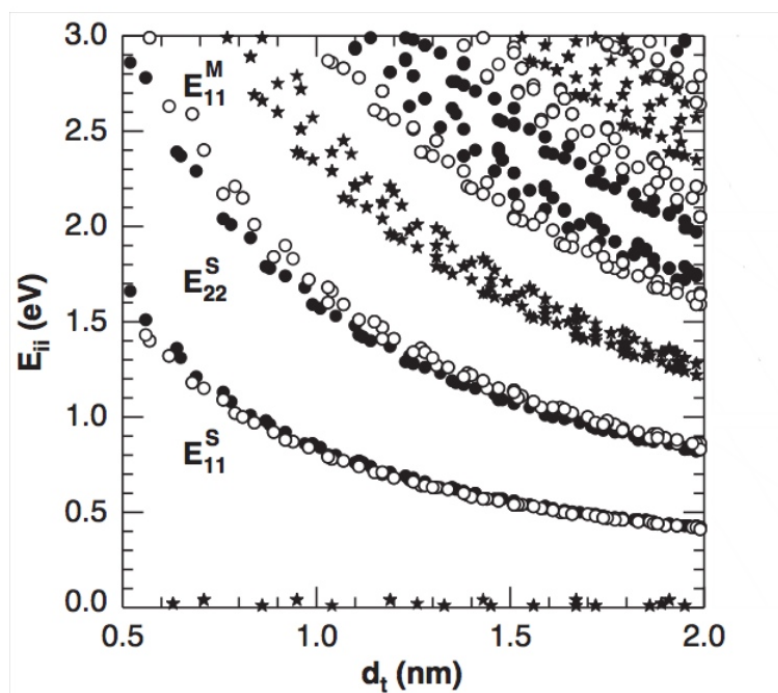


Figure 8 - Figure from Dresselhaus et al.<sup>71</sup> showing the relationship between electronic transition energies and SWNT diameter, where  $E_{ii}^M$  and  $E_{ii}^S$  are transition energies for metallic and semiconducting tubes, respectively.

Phonon scattering within CNTs may also be observed in Raman spectra. During the measurement of Raman spectra, a CNT may absorb energy from the laser, become excited and emit phonons as it relaxes. Multiple scattering events are possible, and, in the sequence of scattering events, the order of the scattering event refers to what place it held in that sequence. So, for example, the *G* band, which is observed at about  $1582\text{ cm}^{-1}$ , is the only first-order Raman peak in CNTs, meaning that the scattering event resulting in the *G* band always occurs first, sequentially, if phonon scattering events occur. There are two possibilities for second-order Raman scattering. Either two phonon scattering events occur or one phonon and one elastic scattering event occurs. An elastic scattering event in a CNT occurs due to defects in the CNT where a phonon changes direction but does not change frequency. The *D* band in CNTs occurs at  $1350\text{ cm}^{-1}$  and consists of one phonon and one elastic scattering event. Since the *D* band consists of an elastic scattering event, it is associated with measuring the degree of disorder within the CNTs. It also indicates the presence of MWNTs. Since Raman spectra are measured in arbitrary units (a.u.) in order to determine the degree of disorder or amount of MWNTs, the ratio of the *G/D* band peaks are calculated. The second-order Raman scattering consisting of two phonon scattering events is labeled as the *G'* band and occurs at  $2700\text{ cm}^{-1}$ <sup>71</sup>.

## CHAPTER 4. INFLUENCE OF CATALYST MORPHOLOGY

### 4.1 Catalyst Morphology and CNT Growth

Recently, research has linked chirality selective SWNT growth to the ambient gas environment during growth. Results have shown that CVD growth at 860°C in a small amount of water (~3.5 mTorr) has resulted in about 91% metallic nanotubes in the presence of a He ambient environment. In similar growth conditions, but by replacing He with Ar, growth resulted in approximately 64% metallic CNTs<sup>63</sup>.

In an attempt to discover the cause of this phenomenon, iron catalyst morphology was observed in-situ ETEM in both helium and argon with a small amount of water. It was observed that the iron nanoparticle showed strong faceting in He, but rounded in Ar. In addition, previous work has shown that water, critical for CNT growth<sup>61</sup>, suppresses Ostwald ripening in iron nanoparticle arrays which would be suitable for CNT growth<sup>39</sup>, and Ostwald ripening rates are higher in argon than in helium<sup>63</sup>.

Two conclusions may be drawn from these results. Either 1) water, or some decomposition of water (*i.e.* hydroxyl or oxygen), adsorbs to the surface of iron nanoparticles and inhibits Ostwald ripening, or 2) some unknown impurity or impurities

in the inert gas adsorb onto the surface of iron nanoparticles and inhibits Ostwald ripening. So, since Ostwald ripening rates have been shown to be higher in nanoparticle arrays that have a more rounded morphology, it is possible to qualitatively measure the degree of faceting in a nanoparticle array by measuring how quickly Ostwald ripening occurs. The idea that a nanoparticle's surroundings can influence their morphology is not new<sup>72</sup>. Using Ostwald ripening as a secondary effect to make conclusions about catalyst morphology in dynamic environments may test both hypotheses through Ostwald ripening studies.

#### 4.2 Experimental Setup and Results

To begin, 18 nm SiO<sub>2</sub> meshed TEM windows were purchased and 1.8 nm of iron was deposited on them by ion beam sputtering. With respect to CNT catalyst preparation, 1.8 nm is thick. Common film thicknesses for CNT catalyst preparation by sputter deposition typically range from about 0.5 – 0.9 nm. In this situation, a thicker film thickness was used to ensure a striking and visible nanoparticle density and size distribution. All samples were first annealed in 2 Torr of hydrogen at 500°C for 30 minutes to reduce the iron film. During the reduction process, oxygen in the iron film is removed, leaving behind pure iron, and the film is broken up into nanoparticles. One sample was prepared using only this initial reduction step and then imaged in plan view TEM in order to measure an estimate for “time 0” before Ostwald ripening in the gaseous environments of interest. See Figure 9. Particle analysis was then performed by utilizing the Dunin-Borkowski algorithm<sup>73</sup>. Just as a note, the sets of images of samples annealed in argon and water were not analyzed rigorously. At the time of measurement and analysis there

were deadlines that prevented thorough data analysis. So, all interpretations of data or trends from the data analysis within this section should be read or observed with a higher degree of skepticism than may be given to a peer-reviewed article.

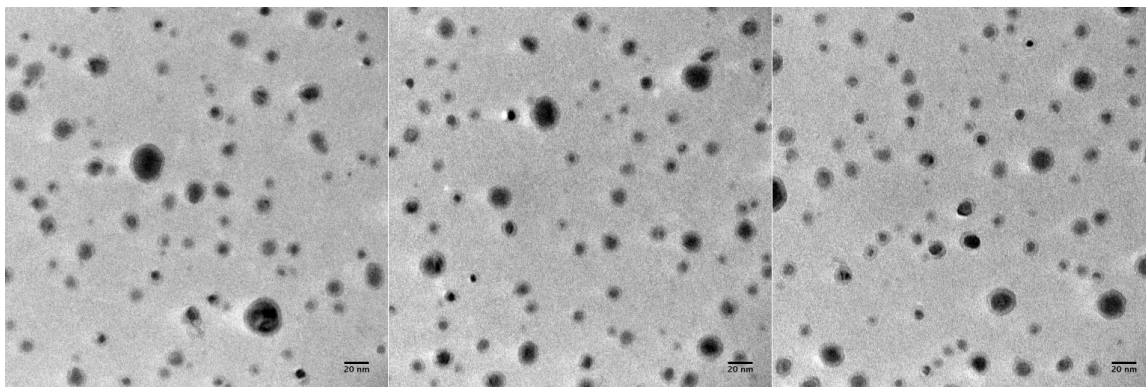


Figure 9 - Plan view TEM images of 1.8 nm iron film after annealing in 2 Torr H<sub>2</sub> at 500°C for 30 minutes.

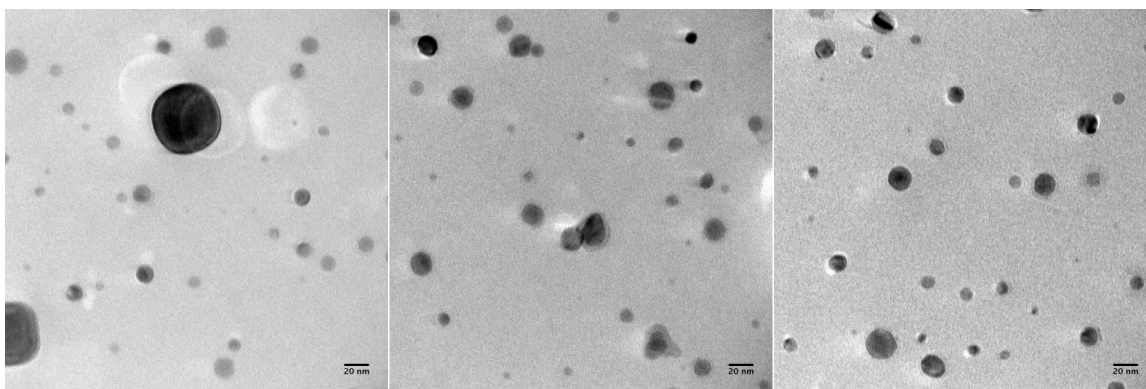


Figure 10 - Plan view TEM images of 1.8 nm of iron film annealed in 2 Torr H<sub>2</sub> at 500°C for 30 minutes followed by 12 Torr of Ar at 700°C for 30 minutes.

After annealing in hydrogen, the samples were annealed in different gas mixtures of argon and water. One sample was annealed in 12 Torr of argon at 700°C for 30 minutes, and three other samples were annealed in a mixture of argon and 100 ppm of water. Three samples were annealed at 700°C for 30 minutes in 100 sccm argon and water and

400 sccm of argon, 200 sccm argon and water and 300 sccm argon, and 500 sccm argon and water. Each sample had a fixed flow rate and was allowed to build up to 12 Torr of pressure before flowing through the chamber. The images from the argon and water experiments are shown in Figure 11. The 200 sccm argon and water images appear brighter because they are bright-field images which were taken to test the effectiveness of the Dunin-Borkowski algorithm of particle analysis.

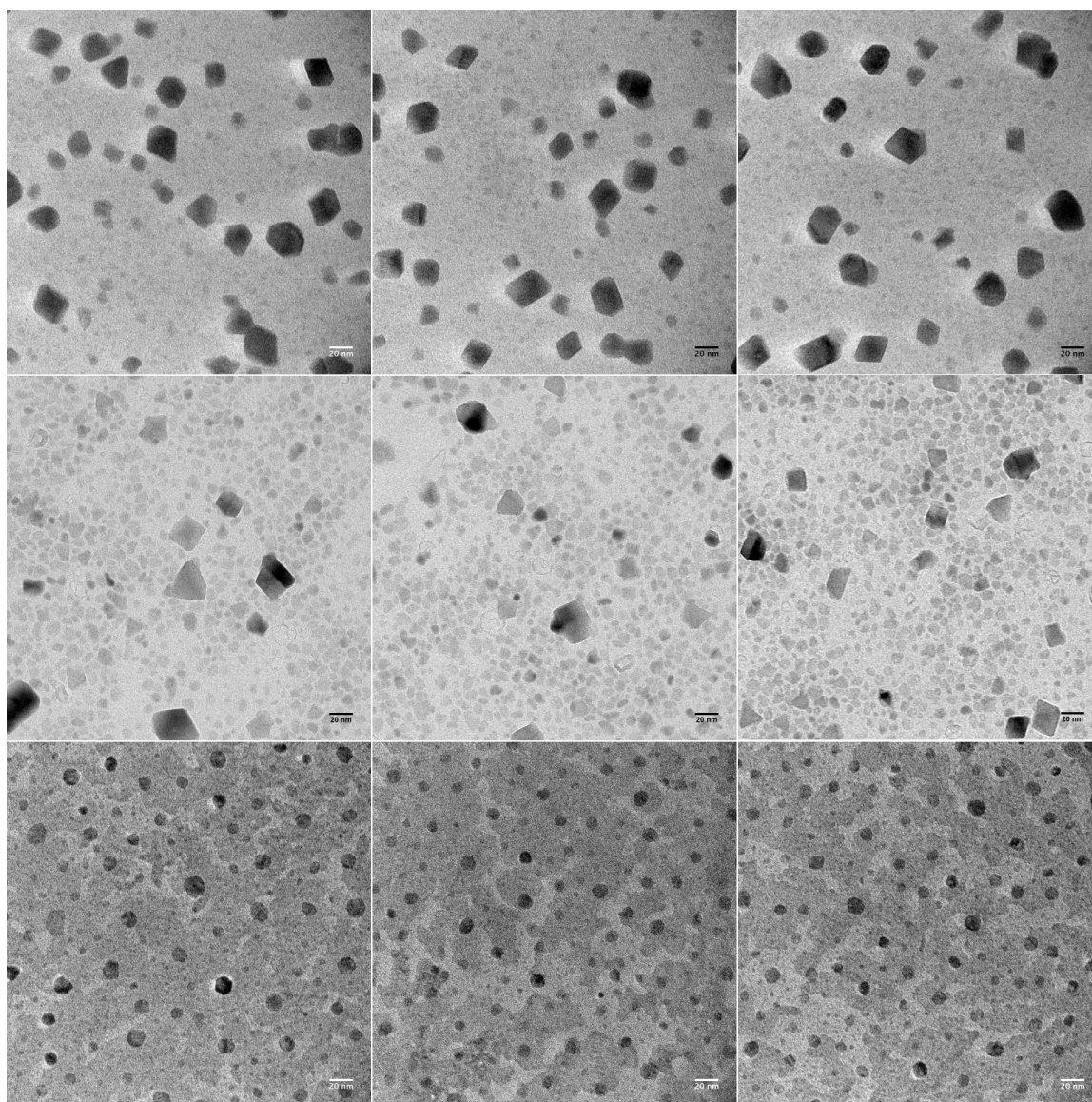


Figure 11 - TEM images of the top row are images of a sample annealed in 100 sccm argon and water with 400 sccm of argon. The middle row of images is from a sample annealed in 200 sccm argon and water with 300 sccm argon, and the last row of images was taken from a sample annealed in 500 sccm of argon and water. All samples were first annealed in 2 Torr of  $H_2$  for 30 minutes at  $585^\circ C$ , and then annealed in their respective argon and water environments at  $700^\circ C$  for 30 minutes.

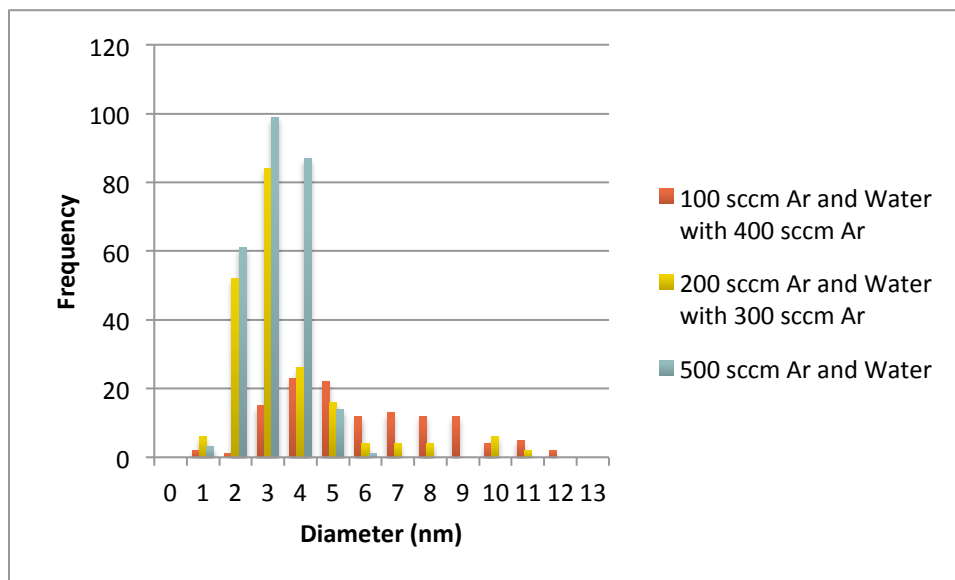


Figure 12 - Histogram of particle diameters for the 1.8 nm Fe films annealed in hydrogen and argon and water.

The particle analysis results are shown in Figure 12. Even though the average particle size decreases with increasing water content, the data is more effectively interpreted through a histogram, which illustrates that as the water content is decreased, the overall particle size increases and spreads out to larger diameters.

Ostwald ripening of iron in a catalyst system, under conditions optimized for CNT growth, is affected by the degree to which water and the gas environment interferes with the diffusion. Referring to Equation (1) on page 14, the images in Figures 9-11 can be used to measure the chemical effect of water on the mobility of iron. Specifically, both



the diffusivity and solubility of iron on the catalyst support are influenced by the interaction of iron with the gas species. Solving for these two constants yields equation (3), and is plotted in Figure 13.

$$(3) \quad DC_{\infty} = [\langle a_t \rangle^3 - \langle a_0 \rangle^3] \frac{9R_g T}{8\gamma V_m^2 t}$$

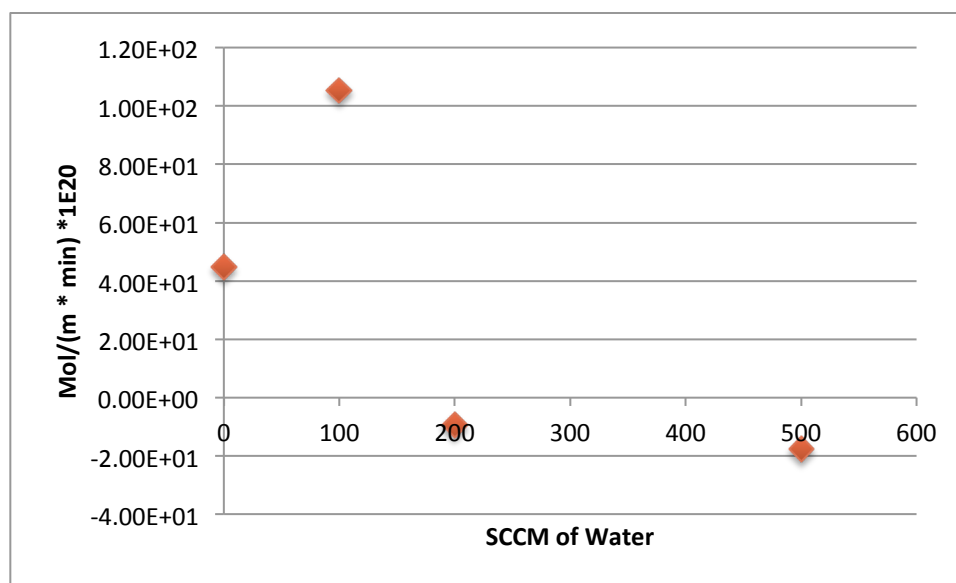


Figure 13 - The mobility of iron (diffusivity x solubility) plotted versus the flow rate of water. As the activity of water increases, the mobility of iron decreases.

The data in Figures 11 and 13 are odd in that, at a certain level of water vapor, the iron mobility actually became negative. There are two possibilities for this to be a real result. Either, the assumption that the data collected from the sample deemed to be at time 0 did not apply to the two samples where mobility was negative, or there was a chemical reaction taking place, which interfered with Ostwald ripening reaction. The last row of images from Figure 11 seems to support the latter conclusion. The support film in the images appears patchy and not uniform in contrast. This reaction could have been a result

of the catalyst reacting with either the excessive amount of water or some impurity in the gas mixture.

Taking a step back, this work was, in part, motivated by a short in-situ experiment performed by Seung Min Kim, a former graduate student at Purdue and currently at the Korea Institute of Science and Technology. The TEM images are presented in Figure 14. Iron was deposited on a TEM grid and reduced in (a) 500 mTorr of hydrogen for 90 minutes, (b) annealed in 500 mTorr of helium for 60 minutes, (c) annealed in vacuum for 40 minutes, and then annealed in increasing steps of argon pressure for 30 minutes each of (d) 1.5 mTorr, (e) 20 mTorr, (f) 500 mTorr, and (g) 1200 mTorr, consecutively. No particle analysis has been performed on these images, but my interpretation of these images suggests that the rate of Ostwald ripening increases with increasing argon pressure.

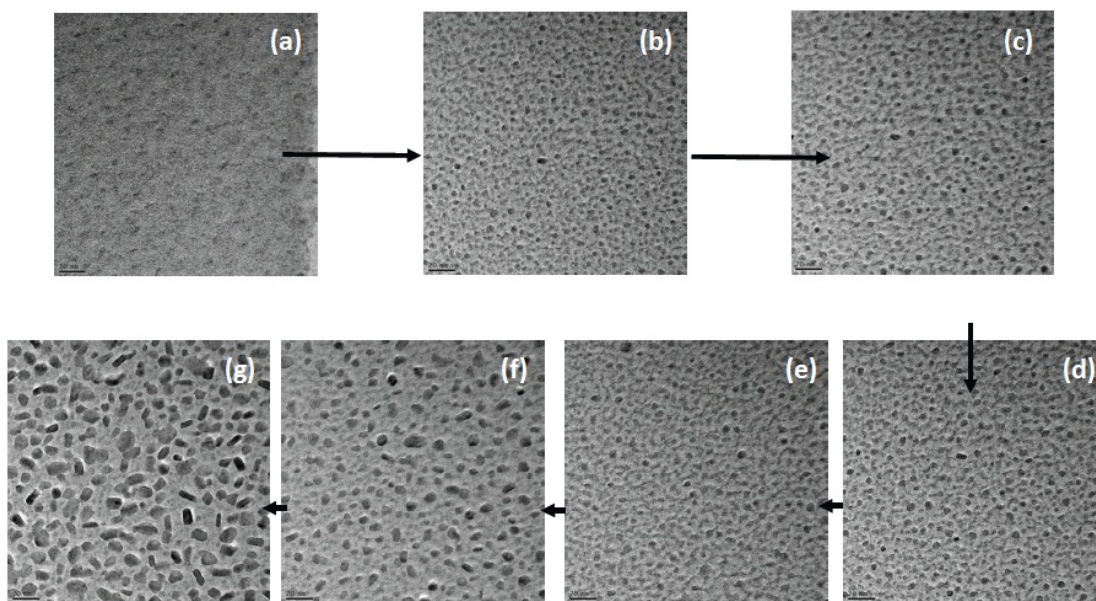


Figure 14 - An iron film reduced in (a) 500 mTorr of hydrogen for 90 minutes, (b) 500 mTorr of helium for 60 minutes (c) vacuum for 40 minutes, and then blocks of 30 minutes in argon at (d) 1.5 mTorr, (e) 20 mTorr, (f) 500 mTorr, and (g) 1200 mTorr.

This ripening concept was compounded by Harutyunyan et al.<sup>63</sup> when it was shown that in the presence of water, iron particles coarsened faster in argon than in helium.

### 4.3 Discussion

The results show that as the activity of water increases (or the overall amount of water) the mobility of the catalyst species decreases, and they seem to suggest that the inert gasses play a role in interfering with the ability of water to inhibit Ostwald ripening. Gases are often thought of in terms of their pressure, and pressure is an averaged force over an area. However, at a smaller scale, this is simply gas molecules with different kinetic energies and momentums colliding with a surface. But, since different ripening behaviors are observed at equal pressures in different gasses, it may be necessary to look at how these gasses are interacting with the catalyst particles. This may be modeled by

considering the ability of the inert gas environment to transfer momentum to the catalyst particle and its adsorbates. Helium is a lighter element and therefore cannot transfer as much momentum to adsorbates on the surface of catalyst particles as heavier atoms like Ar or Xe. This results in catalyst particles in He undergoing lower Ostwald ripening rates and, therefore, exhibiting stronger facets.

When modeling how these inert gasses behave in dynamic CNT growth conditions, it may be useful to consider the Knudsen number of the gas. The Knudsen number is a dimensionless constant that relates a particle's mean free path to an arbitrary length scale. In this case, the length scale will be the size of the particle. So,  $Kn = \frac{\lambda}{L}$  where  $Kn$  is the Knudsen number,  $\lambda$  is the mean free path, and  $L$  is the arbitrary length scale. For an ideal gas,  $Kn = \frac{k_B T}{\pi \sigma^2 p L \sqrt{2}}$  where  $k_B$  is the Boltzmann constant,  $\sigma$  is the hard shell diameter of the gas particle, and  $p$  is the total pressure.

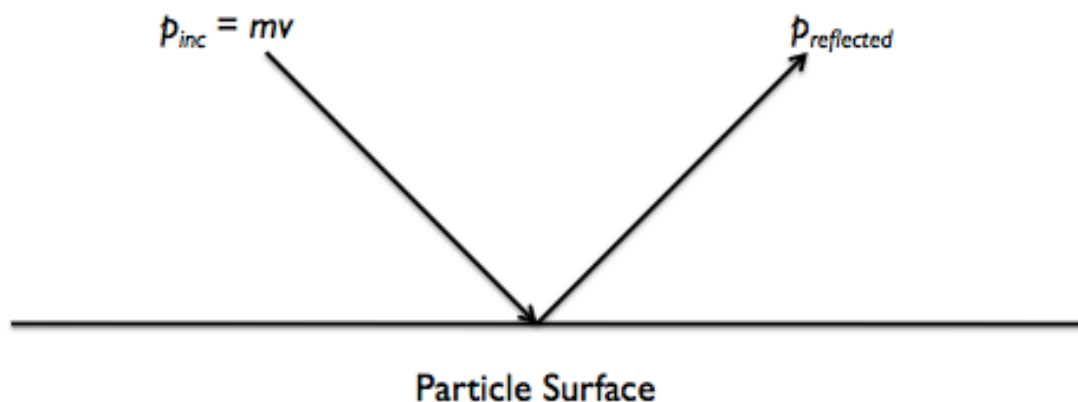


Figure 15 - Rough schematic of a gas molecule colliding with a catalyst. The incident momentum of the gas molecule is labeled and defined as its mass multiplied by its volume.

When the inert gas molecule collides with a catalyst particle (or adsorbed decomposed species of water), some momentum is transferred from the gas molecule to the catalyst (Figure 15). This interaction may be modeled by defining a momentum transfer coefficient,  $\alpha_{momentum} = \frac{p_{reflected} - p_{inc}}{p_{wall} - p_{inc}}$ , where  $p_{reflected}$  is the momentum of the gas molecule after the collision,  $p_{inc}$  is the momentum of the incident gas molecule before the collision, and  $p_{wall}$  is the momentum that has been transferred to the particle surface after the collision. If the momentum transfer coefficient is 1, then momentum is completely accommodated and the gas molecule reflects diffusely. In contrast, if the momentum transfer coefficient is 0, then the gas molecule has not transferred any momentum to the catalyst or its adsorbates and it will reflect specularly. There is also a corresponding energy transfer coefficient,  $\alpha_{energy} = \frac{E_{reflected} - E_{inc}}{E_{wall} - E_{inc}}$  where  $E$  is energy and the subscript labels identify the energies of their corresponding momentums.

The resulting function that describes this momentum transfer model is  $f(Kn, \alpha_{momentum}, \alpha_{energy})$ . This is a complicated function that has many compounding factors such as ambient gas composition and particle surface roughness. It is difficult to tune just one of the many parameters that goes into this function, but what we can do is to scale the Knudsen number of the gas environment which can be approximately done by scaling the mass flux of the ambient gas environment.

It has been previously noted<sup>39</sup> and again shown in this body of work that water interferes with Ostwald ripening. In addition, it has been demonstrated the rate of Ostwald ripening

is affected by the amount of water in the system. The significant and underlying question brought about by this and previous works is: what, exactly, is the water doing in this system?

Akimov<sup>74</sup> performed XPS on an iron surface exposed to water and oxygen. Measurements were taken at different temperatures to observe the relative amounts of adsorbates present on the iron surface. Water was only stable as an adsorbate up to about -73°C. At the maximum temperature which data was presented for, around 400°C, both oxygen and hydroxyl adsorbates are present. However, the amount of hydroxyl is decreasing with temperature and the oxygen adsorbate is dominant. It is difficult to say with certainty that oxygen is the dominant adsorbate during CNT growth because growth temperatures are much higher (above 700°C) and iron begins a phase transition from ferrite (body-centered cubic [BCC]) to austenite (face-centered cubic [FCC]) around 727°C<sup>75</sup>. The iron surface density increases significantly between ferrite and austenite, comparing the density of the (111) FCC plane to the (110) BCC plane<sup>76</sup>. Whether or not this increase in surface density, corresponding with an absolute decrease in surface energy<sup>77</sup>, is enough to compensate increases in temperature and kinetic energy should be experimentally tested.

A few experiments need to be completed in order to rigorously test the theory of momentum transfer presented in this section. The data presented indicating increased catalyst Ostwald ripening rates in increased pressures of gas is a very striking result. Ostwald ripening theory predicts higher ripening rates at higher material solubility, and

solubility increases with ambient gas pressure. As pressure increases, either temperature or moles of gas must increase as well. Both increased kinetic energy and increased material will raise solubility. However, Ostwald ripening performed on Ni<sup>78</sup> and evaporation work on tungsten<sup>79,80</sup> have shown that metal evaporation in the presence of gas is extremely low. It could be possible that impurities in the inert gasses used are responsible for differences in Ostwald ripening behavior. To completely rule out the possibility of impurities interfering with the ability of water to inhibit Ostwald ripening, impurity levels near the part per billion level would need to be achieved, as it has been shown that even gaseous impurities at a level of 1 part per million (ppm) can have an effect on catalytic behavior<sup>81</sup> and carbon nanotube growth<sup>82</sup>. However, if the mass flux of helium, argon, and xenon are scaled to be equal and similar Ostwald ripening behaviors are observed then that result would be further evidence in support of the theory of the significance of momentum transfer in gas dynamics.

The mass flux of gasses is proportional to  $\sqrt{mp}$ , where  $m$  is the mass of the molecule and  $p$  is pressure. So, for example, if the mass flux were to be scaled to that of helium at 1 Torr, the scaling constant would be  $\sqrt{mp} = \sqrt{4.0026} \times 1 = 2.0006$ . The pressure of argon needed to have an equal mass flux to that of helium would be  $\frac{2.006}{\sqrt{39.948}} = 316.53$  mTorr. It is important to note that the scaling constant for normalizing mass flux does not have a time scale factor. So, even if the mass flux of inert gasses are made equal in Ostwald ripening experiments, the samples annealed in different gasses may not coarsen

at the same rate. So, it would be critical to do tests at multiple anneal times to measure the rate relationship between gasses.

To truly test the effects of the inert gas kinetics on CNT growth, tests should be designed to be performed during growth. The proposed tests in this section are all done without the presence of a carbon precursor, and, thus, without growth. Testing catalyst behavior dependence on the environment is complicated as it is difficult to discern catalyst behavior during growth. However, borrowing from Kim et al.<sup>67</sup> it may be possible to test the catalyst decay rate dependence on inert gas flow rate. Previous tests from that work used square wave pulses of acetylene to test the growth kinetics dependence on temperature and acetylene flow rate. A similar test could be designed to measure growth using simultaneous square wave pulses of acetylene and higher amounts of inert gas. Since it has been shown there is no dependence of catalyst decay rate on acetylene flow, square wave pulses of acetylene or any other carbon precursor used in combination with square wave pulses of inert gas would only show the catalyst decay rate dependence on the extra inert gas pulsed through the system. For example, a constant flow of water and helium could be set up in a CVD system. A waveform generator could be used to generate a square wave pulse of both acetylene and extra inert gas, which could be a higher level of helium, argon, or xenon. Since the catalytic decay rate for temperature and acetylene have already been measured, any extra decay occurring on the catalysts in the sample would likely be due to Ostwald ripening induced growth termination from the enhanced Ostwald ripening rate caused by the extra inert gas flow.



## CHAPTER 5. CONTROLLING CATALYST ACTIVITY VIA SUBSTRATE MANIPULATION

### 5.1 Ion Beam Bombardment of Substrates

Earlier discussions have noted the importance of the substrate in supporting CNT growth. The most popular supports are alumina and silica. Past work on alumina has shown that different methods of depositing alumina support films for CNT growth have different effects on CNT growth. While single crystal sapphire does not support growth, alumina deposited by magnetron sputtering, electron beam evaporation, and ALD supported vertically aligned CNT (VA-CNT) growth, exhibiting the importance the substrate on catalytic activity. It was observed that the critical structural feature for supporting VA-CNT growth was substrate porosity, which reduced coarsening (Ostwald ripening) and extended the lifetime of the catalyst<sup>62</sup>. With the knowledge that ion beam bombardment of substrates damages the top surface and introduces porosity<sup>83</sup>, the hypothesis that ion beam bombardment of inactive substrates (*i.e.* sapphire) may turn them into active substrates that supported CNT growth is explored in this chapter.

In addition to the fact that catalyst size affects CNT growth, it is also known that the choice of substrate has an enormous effect, as discussed in section 1.3.3. It is known that defective alumina is an excellent substrate for CNT growth, but, in contrast, pristine

sapphire will not support growth. This is mainly attributed to the fact that an atomically flat substrate acts like a highway for atoms. Flat, single-crystalline surfaces have relatively homogenous and low surface energies. So, there is very little energetic barrier to fix catalyst atoms or clusters of atoms in place.

## 5.2 Experimental Setup & Results

To test the hypothesis, c-cut sapphire was exposed to a 5kV Ar<sup>+</sup> beam at a dose of about  $2.1 \times 10^{20} \text{ cm}^{-2}$ . Once damaged, 1 nm of ion beam sputtered iron was deposited on the surface of the damaged substrate, and then annealed in hydrogen at a flow of 200 sccm at 585°C for 10 minutes to reduce the iron and break it up into individual catalyst particles. After annealing, the samples were then let to cool to room temperature in a hydrogen environment. Some samples that were subject to this procedure were characterized by AFM and others were immediately used to test growth. To test for catalytic activity, the samples were exposed to 470 sccm of argon, 100 sccm for hydrogen, 25 sccm of ethylene (the carbon source), and 50 – 80 ppm of water at 760°C for 30 minutes. Not only did growth occur, but VA-CNT growth was achieved. In addition, a standard mesh molybdenum TEM grid was used as a grid to test the ability to pattern substrates. In this scenario, the entire substrate was coated with Fe, but only the exposed surface of the substrate was damaged by Ar<sup>+</sup> bombardment. Due to the substrate modification by the ion beam, VA-CNT growth only occurred in the patterned region, as seen in Figure 16.

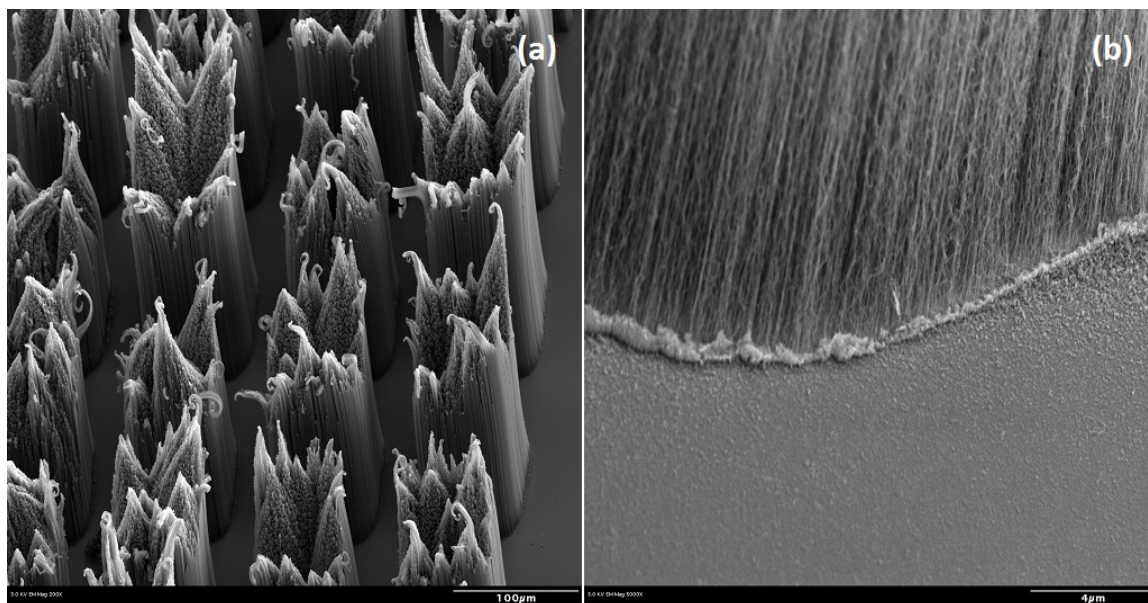


Figure 16 - SEM images of (a) the patterned sapphire substrate showing VA-CNT growth, and (b) a higher resolution image of the edge of the growth.

The VA-CNTs grown by this method were about 0.8 mm tall and had a Raman spectra  $G/D$  ratio of 1.4, as seen in Figure 17. This is a relatively low  $G/D$  ratio, and it indicates the presence of MWNTs<sup>84,85</sup>. This was confirmed in TEM (Figure 18). However, these growth results are similar to what has been previously achieved on ALD alumina supports<sup>52</sup>. To illustrate the contrast and effectiveness of this new procedure, growth was attempted on a flat, unadulterated c-cut sapphire substrate, and only a few CNTs grew and there was no VA-CNT growth.

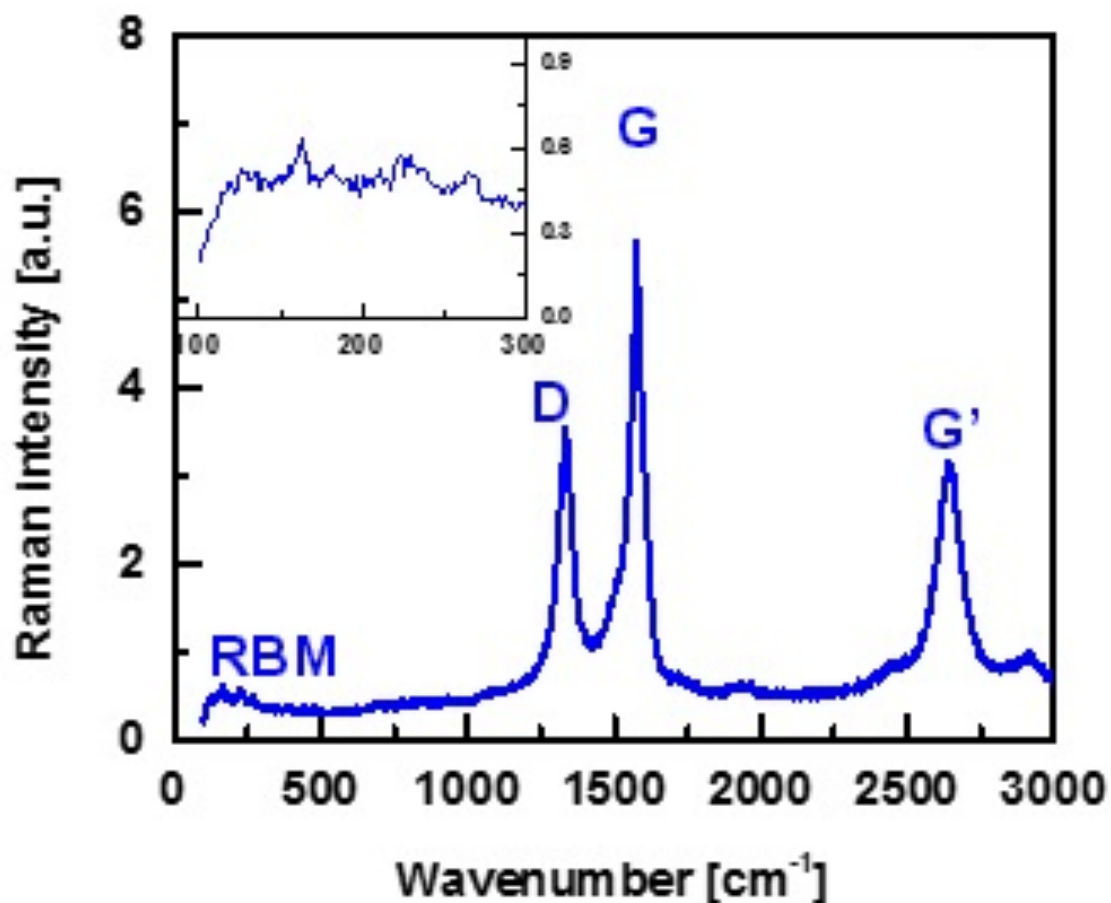


Figure 17 – Raman spectra measured from the top of the VA-CNT growth showing a G/D ratio of about 1.4 and the presence of the G' band. The radial breathing modes are shown in the top-left inset from about 150 – 300  $\text{cm}^{-1}$ .

In addition to the VA-CNT growth on the damaged sapphire substrate, flakes of catalyst support were also observed on top of the carpet. This is consistent with odako growth<sup>86-88</sup>, where the catalyst grows the nanotube downward, elevating itself and small flakes of the supporting substrate as growth occurs.

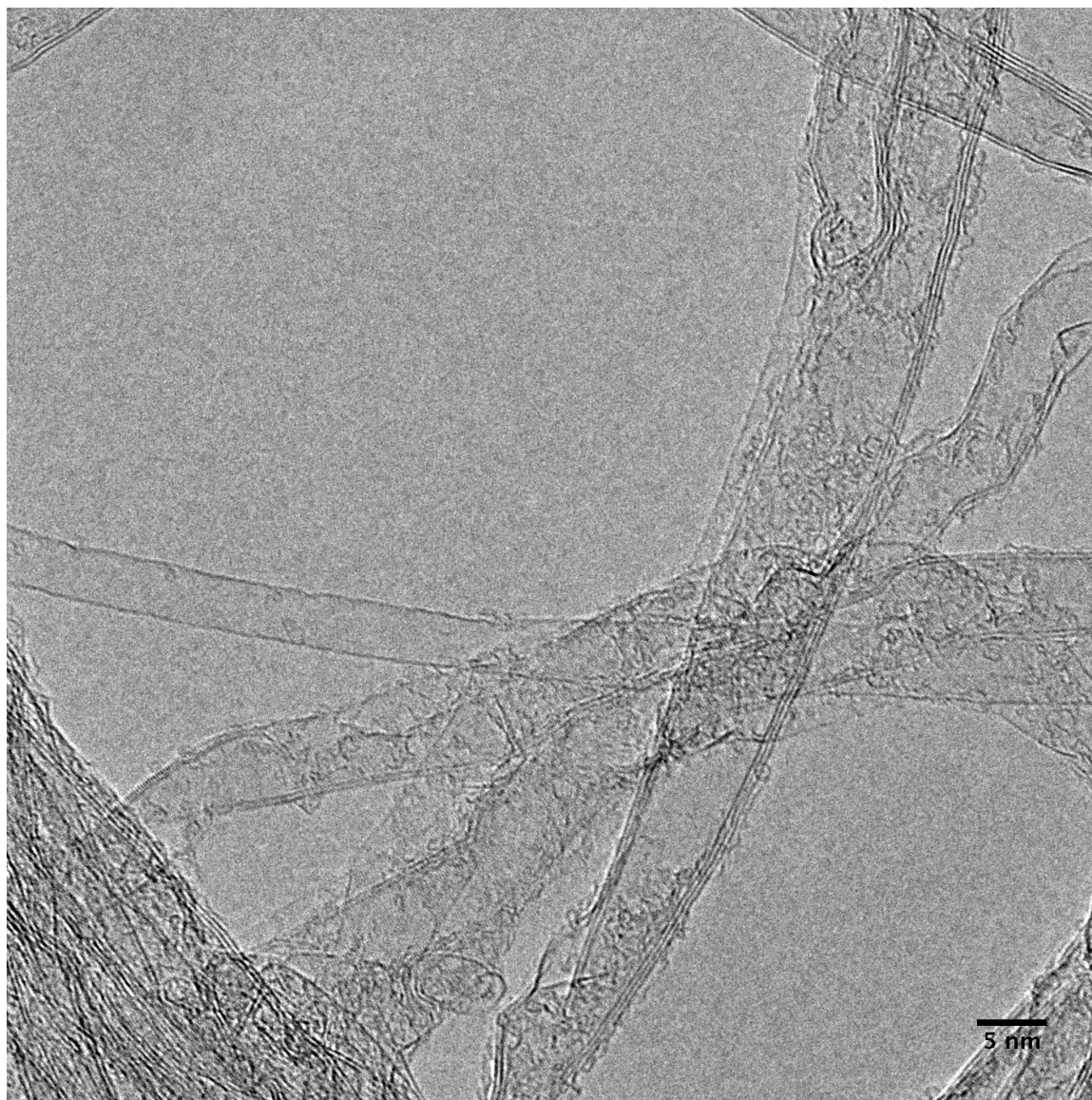


Figure 18 - TEM image of a small subset of CNTs grown on the modified sapphire substrate. A variety of CNTs are present, including single-wall, double-wall, and MWNTs.

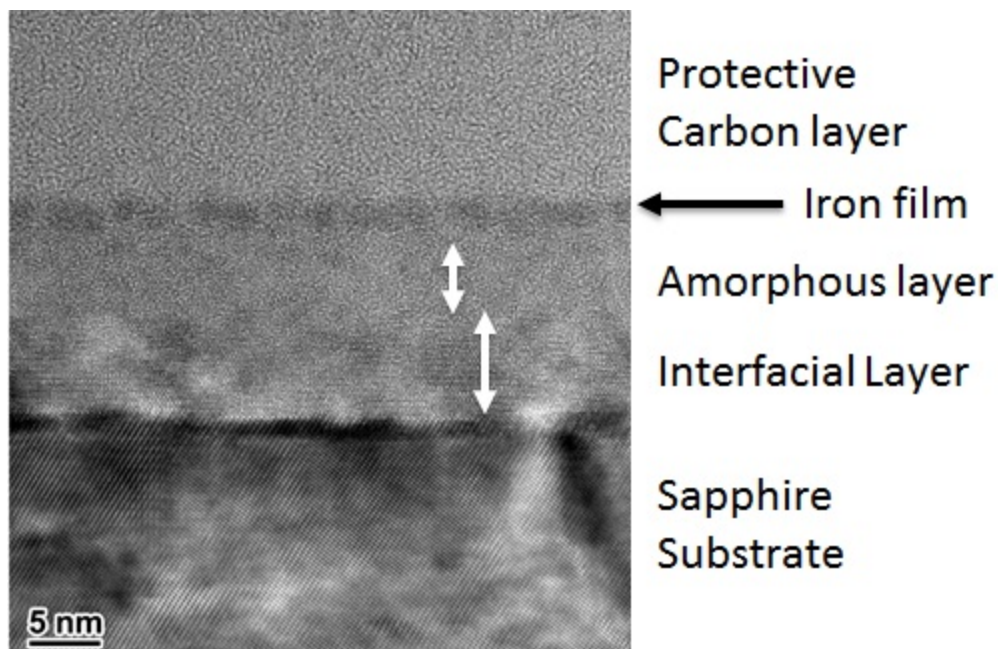


Figure 19 – Cross-section TEM image of ion beam damaged c-cut sapphire substrate with deposited iron. The substrate, and two-layer damaged region consisting of an amorphous layer and interfacial layer are clearly visible.

The nature of the  $\text{Ar}^+$  beam damage was observed and characterized by cross-sectional TEM. Cross-sectional TEM was performed on a sample that was prepared from a c-cut sapphire substrate that was damaged by an  $\text{Ar}^+$  beam with a flux of  $3.8 \times 10^{20}$  ions/cm<sup>2</sup> and an accelerating voltage of 5 keV. Images showed a two-region damaged layer of about 13 nm, as seen in Figure 19, which was confirmed in X-ray reflectivity (XRR). The two-region layer consisted of a crystalline, epitaxial, bottom-layer, which sits on top of the non-damaged substrate and an amorphous layer on top supporting the catalysts. This is consistent with past work that has been done on ion beam damage of silicon and sapphire substrates<sup>89-91</sup>.



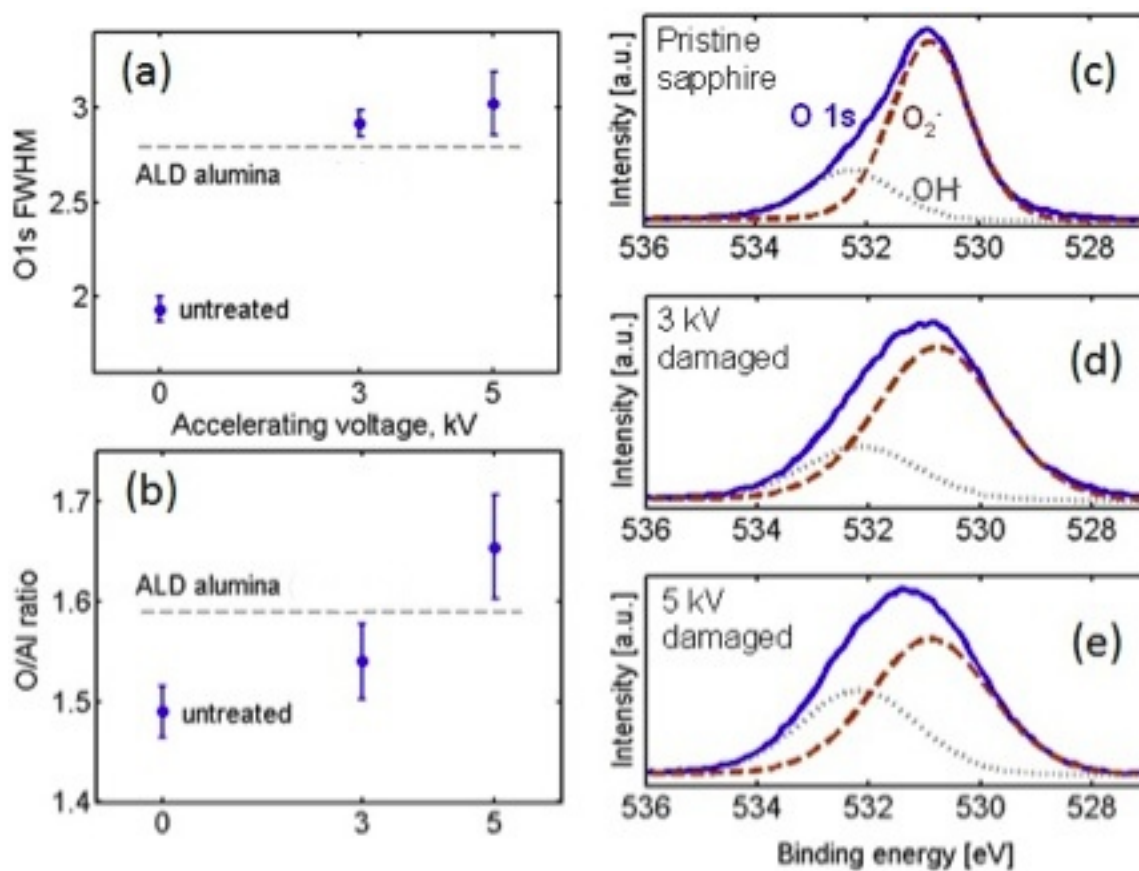


Figure 20 – XPS data detailing the enhancement of surface activity with respect to ion bombardment beam energy. (a) Diagrams of the O 1s FWHM and (b) the ratios of the area under the O 1s peak to the area under the Al 2p peak for untreated sapphire and sapphire damaged by 3 keV and 5 keV ion beams. The dotted lines indicate the level of untreated ALD alumina. Diagrams (c), (d), and (e) show the O 1s peaks for pristine sapphire, 3 keV, and 5 keV respectively. Notice how the O 1s peak shifts with increasing ion beam energy.

X-ray photoelectron spectroscopy (XPS) was used to measure the change in surface chemistry with respect ion beam energy, as seen in Figure 20. Measuring the oxygen-to-aluminum ratio using XPS identifies changes in stoichiometry of  $\text{Al}_2\text{O}_3$  at the substrate surface<sup>92</sup>. In addition, measuring changes in the ratio of surface-active oxygen to stable

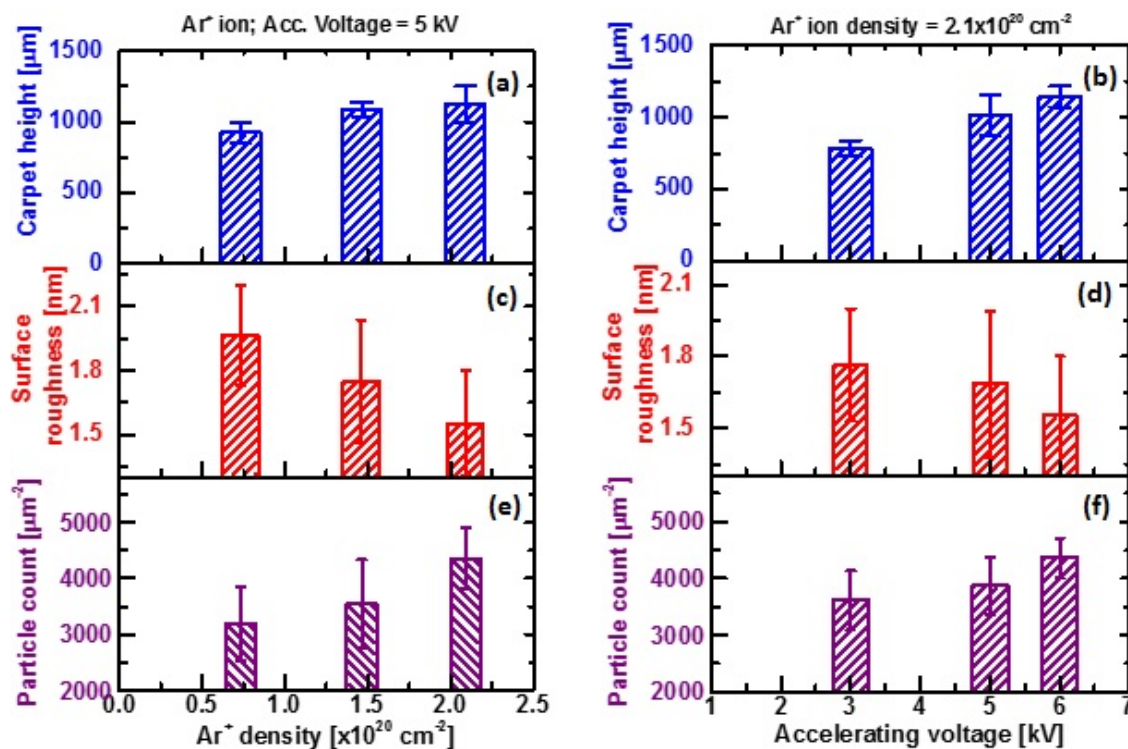


Figure 21 - Results of varying accelerating voltage on (a) VA-CNT carpet height, (c) surface roughness, and (e) particle count, and the results of varying ion density on (b) VA-CNT carpet height, (d) surface roughness, and (f) particle count.

oxygen can indicate changes in the absolute number of surface-active oxygen sites for catalytic activity. Figure 20 compiles the XPS data for the treated sapphire substrate and untreated sapphire, and displays evidence for the ability to tune the surface chemistry of sapphire by bombarding the surface with  $\text{Ar}^+$  ions and varying the energy of the beam by changing the accelerating voltage. Figure 20(b) details the ability to tune the number of



oxygen active sites by varying the accelerating voltage. Figures 20(c – e) show how the O 1s peak changes with ion beam energy. The peak shifts to lower energies with increasing beam energy. The O 1s peaks are the sum of the  $\text{O}_2^-$  and  $\text{OH}^-$  peaks. The shifting of the peaks is due to the change in the relative intensities of the  $\text{O}_2^-$  and  $\text{OH}^-$  peaks. The values of the O 1s full-width at half maximum (FWHM) and O/Al ratio are compared to that of ALD- $\text{AlO}_x$ <sup>92,93</sup>, which is a common support for VA-CNT growth. The ion-beam damaged sapphire exhibits chemical similarities to ALD alumina. Specifically, the damaged substrates show higher  $\text{OH}^-$  concentrations, which correspond with increased catalytic activity<sup>92</sup> and longer catalyst lifetime. The correlation between ion beam damage, VA-CNT growth (Figure 21), the top amorphous substrate layer, and hydroxyl enrichment leads to the conclusion that the disordered nature of the top alumina substrate layer directly leads to enhanced catalytic activity and lifetime.

### 5.3 Discussion

This work expands our current understanding of carbon nanotube growth by building upon our previous knowledge of suitable CNT growth supports. By varying the degree of damage by controlling the accelerating voltage of the argon ion beam, characteristics of the substrate that are required for VA-CNT growth may be controlled, such as surface chemistry and surface roughness. In turn, these substrate properties control catalytic activity, stability (in terms of particle migration), and density. More generally, this opens the door to the possibility of modifying or tailoring substrates to maximize their interaction with catalysts. What this could mean is being able to maximize the catalyst

efficiency, growth rate, catalyst lifetime, or potentially even chirality control simply through substrate modification.

Modification of a substrate for CNT growth could control two major aspects of a substrate: surface chemistry and roughness. As has been shown in this work, argon ion beam bombardment can change the relative amounts of active oxygen sites. Increasing the bombarding ion beam energy increases the relative amount of OH<sup>-</sup> active sites on the surface of the support. Damaging the surface of the support also increases the surface roughness. Increasing the roughness increases surface area. This either increases the surface area of the support that the catalyst particle can interact with, thus increasing the coordination of the catalyst particle, increases the chance that a catalyst particle will find a preferential spot on the support to sit, or it does both.

A number of future avenues of work logically present themselves from this body of work. First, different ion beams should be tried for this method of substrate surface modification. Different ions may interact or modify the substrate differently both chemically and topographically. In an extreme case, hydrogen may be utilized to lightly roughen modify the surface of the substrate. In the case of hydrogen, the ion is very small and will likely only damage the very top surface of the substrate, but it may also implant into the surface and modify its chemical nature. Adding more hydrogen ions could potentially increase the amount of OH<sup>-</sup> active sites on the surface. However, the lower amount of damage would result in either a small amount of pores near the surface or no pores at all. It has been demonstrated that porous substrates are generally better at

growing CNTs due to their stronger interaction with catalyst particles and the higher rate of carbon precursor diffusing through the substrate<sup>94</sup>. Thus, a lower porosity substrate damaged by a hydrogen ion beam may not grow as well, but still may provide insights as to the importance of surface chemistry in CNT growth.

Varying substrates is also a potential area of research. Testing substrates that do not tend to support aligned growth, such as quartz or titanium nitride, would be a logical next step. For similar reasons discussed above, adjusting substrate porosity or modifying surface chemistry could transform previously unsuitable substrates for CNT growth into catalytically active supports that regularly support VA-CNT growth.

## CHAPTER 6. USING GRADIENTS TO STUDY CNT GROWTH

### 6.1 CNT Growth Dependence on Catalyst Size

The generally accepted theory is that the size of the catalyst particle has some effect on the diameter of a growing CNT<sup>95-97</sup>. It stands to reason that a hypothetical catalyst particle with a diameter of 3 nm is unable to grow a carbon nanotube with a diameter larger than its own. This is simply due to the fact that a catalyst particle cannot deliver carbon to a growing CNT that it does not touch.

As stated earlier, CNTs are defined by their chiral vector. This vector  $(n,m)$  defines not only the chirality, but also the diameter of the CNT. Figure 1 illustrates this point. Thus, if one wants to achieve chirality control during growth, it seems that focus should be directed toward smaller diameter CNTs, and thus, catalyst particles. This is due to the fact that, as the catalyst diameter increases, the potential number of chiralities it can grow also increases. By limiting catalyst size, we may be making it easier to select specific CNT chiralities to nucleate and grow.

Catalyst film reduction is a critical step in CNT catalyst preparation<sup>38,53</sup>. Between the deposition of the catalyst film or whole catalysts, it is very likely that these samples will be exposed to air unless specially fabricated sample deposition and growth chambers are fabricated in order to prevent this from occurring. Since transition metals oxidize very easily due to their partially filled *d* orbitals, these films must be reduced to remove the unwanted oxygen and form individual active catalyst particles<sup>53</sup>. Reduction time is an important factor in this process because it is necessary to fully reduce the catalysts without unnecessarily facilitating Ostwald ripening. Ostwald ripening is responsible for increasing the size distribution of the catalyst particles and the average size<sup>98</sup> and may even terminate growth<sup>99</sup>. As discussed earlier, size is of critical importance when growing CNTs, especially SWNTs. The formation of the catalyst particles is a function of the feedstock gasses used for reduction and the reaction rate, which can be influenced by pressure and temperature.

## 6.2 Experimental Setup

To test the dependence of CNT growth on catalyst size, iron gradients were created directly on TEM grids. Silicon nitride films 15 nm thick on TEM grids with rectangular slots (100  $\mu\text{m}$  x 1500  $\mu\text{m}$ ) were deposited with 2.5 nm of ion beam sputtered (IBS) silica in order to simulate an oxide surface suitable for CNT growth. Iron was then deposited as a gradient along the length of the slots from 0 nm to 2.0 nm thick. The gradients were fabricated simply by inserting a razor blade in the path of the sputtered Fe beam, as shown in Figure 22. Once deposited, the Fe film was then heated at 585°C in a reducing environment of H<sub>2</sub> flowing at 200 sccm for 10 minutes. Once the particles were formed,

the TEM was utilized to take images at different thicknesses at 0.1 nm intervals along the gradient of the Fe film. A profile of the gradient was measured using XRR to determine the position of film thicknesses along the length of the gradient. The raw XRR data is noisy and was smoothed by utilizing a moving average with a period of 15. Once the profile was determined, the position of the gradient thicknesses were found within the TEM by simple geometry. The slope of the slot sidewall could be determined simply by noting the  $(x,y)$  position of the beginning of a slot window and a random position along the length of the wall. By finding the equation describing the slot sidewall and utilizing the Pythagorean theorem to determine distances along that wall, the position of specific film thicknesses could be found. Once the images were taken, particle statistics were measured by masking particles with black ovals, circles, or in cases of irregular looking particles, polygons and feeding the masked images into the Dunin-Borkowski algorithm<sup>73</sup>. See Figure 27.

At this point, it may be useful to discuss the current state of particle analysis in electron microscopy. There are many programs and algorithms in the literature that claim to be able to accurately automate the process of finding particles in images on model samples (*i.e.* high contrast, dispersed, regular particles), particularly in TEM. These claims made are valid; however, they by no means have definitively solved this issue of automatic particle statistics analysis. There are still many situations in which these methods simply fail. For example, a few techniques were used to try to automate the measurement of particle statistics for the Fe gradient samples used in this study. The most successful method, by Dunin-Borkowski et al., was more than 90% accurate at finding particles.

This is strictly a rough estimate made by eye with no statistical backing. However, it had trouble accurately finding the edges of those particles and often erroneously identified particles which were just contrast variations on the support. This is simply due to the fact that these particles had oxidized (as some metals do simply when exposed to air) and they

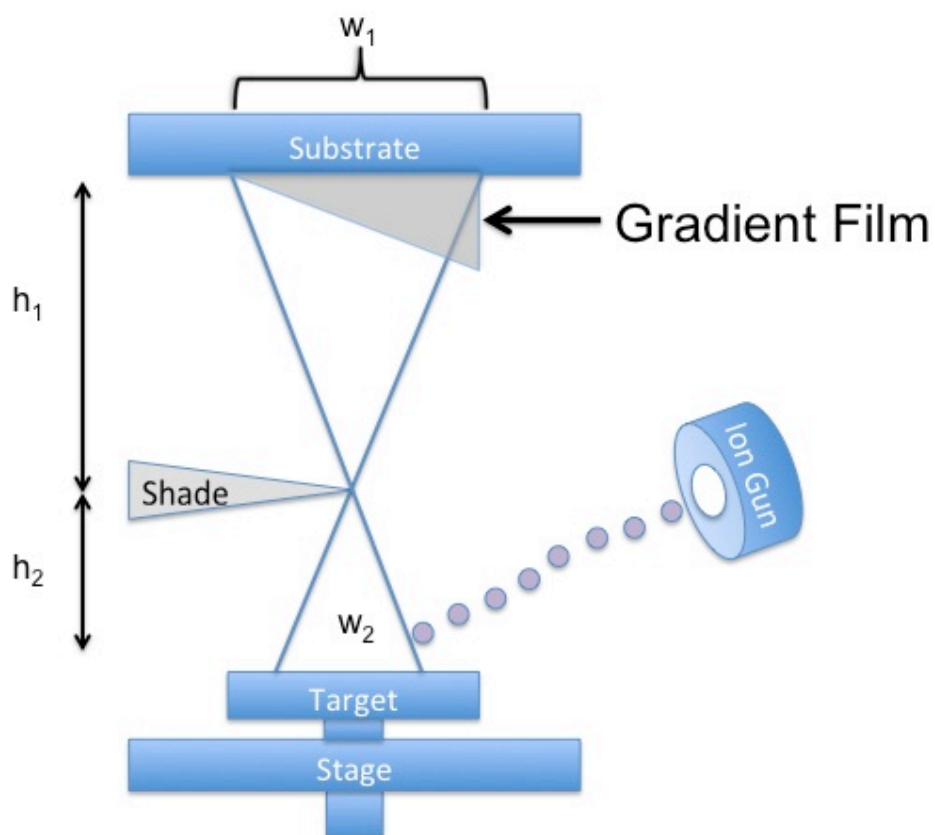


Figure 22 - Schematic diagram of sputter coating gradient onto a substrate with gradient accentuated to show orientation.

were sitting on an amorphous surface. The high contrast speckling of white and black dots on an amorphous region makes it difficult for a computer algorithm to accurately determine the boundaries of particles that themselves do not have a high contrast with respect to the substrate due to their oxidized state. The Dunin-Borkowski method is optimized for bright-field TEM images, where much of the information within the image

is cut out due to the presence of a small objective aperture. While bright-field TEM does smooth out the appearance of amorphous materials, it can also cut off information in the image relating to the particles themselves if they have some portion that does not diffract much, such as an oxide layer. However, one commonality between many particle analysis programs is the thresholding of images while throwing away important information such as curvature. Any particle is most likely to be round and has limits to the curvature of its boundaries. This information is likely left out due to computational cost. However, with our current state of computing power it needs to be reconsidered as a critical component in any particle identification algorithm.

The gradients were created by utilizing an IBS system where the target is the material to be deposited. In this case, the target was iron. See Figure 22. A razor blade is placed between the path of the plume to the sample, which is placed above the target. The blade acts as a shade to block the Fe plume from half of the sample while the unblocked half is coated with the gradient. There are two methods for controlling the gradient. The first method is by adjusting the distance between the blade and the Fe target. When the ion beam strikes the target, Fe is ejected in a plume with a Gaussian distribution. If we assume there is some crossover (*i.e.* some of the plume, when ejected, travels towards the central axis rather than parallel to it or away), then moving the shade closer or farther away from the target will either limit or expand the width of the plume, respectively. Referring to Figure 22, the relationship between the width of the emitted plume, the deposited gradient, and the shade height can be expressed as  $w_2 = w_1 \frac{h_2}{h_1}$ . The second method is adjusting the tilt of the specimen. The plume approaches the specimen at an



angle, not perpendicularly. So, by tilting the specimen away from the plume in the direction of the gradient, the distance traveled by the plume increases and the gradient is extended. Illustrated in Figure 23, the extension in the width of the gradient can be

expressed as  $w'_1 = h_2 \frac{w_1}{w_2} \cos \theta_1 \left[ \frac{1}{\sin(\theta_1 + \theta)} + \frac{1}{\sin(\theta_1 - \theta)} \right]$ .

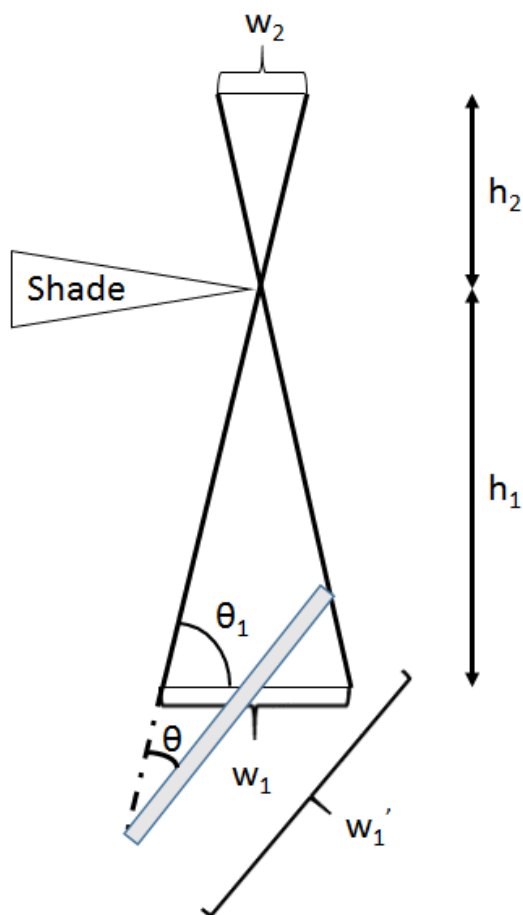


Figure 23 – Schematic of sample preparation controlling gradient deposition.

It should be noted that all substrate preparation, growth, and Raman analysis was performed at Wright-Patterson Air Force Base (WPAFB) and the corresponding TEM studies were done at Purdue University and WPAFB.

### 6.3 Results

One sample, labeled A2 was prepared by the previously discussed method, and then imaged in an FEI Titan ETEM operating at 300 keV. Those images are compiled in Figures 24-29. Most striking is the core-shell nature of many of the particles, and the qualitative phenomenon that at lower thicknesses particles begin to appear that do not share the core-shell structure of the majority. Particle diameter statistics were measured and a few phenomena appeared. Discontinuities at 0.4 nm and 0.6 nm were observed. However, the sample size was low. Particle counts ranged between 75 – 160 particles per sample thickness. Four more samples were prepared, most at the same time. One sample, T3, had iron deposition prepared separately from the rest of the samples, but all samples were annealed in hydrogen at the same time. The second set of four samples (T3, T7, S8, and T9) were all imaged in a 200 keV CM200. For this set of data, more images were taken at a lower magnification, resulting in a larger sample size, ranging from 300 – 700 particles per sample thickness. The resulting particle diameter statistics are compiled in Figure 31. All images were taken as close to identical thicknesses as possible at 0.1 nm intervals, however the data in Figure 31 is plotted in a cluster around the exact thickness to more clearly illustrate the error bars for each data set. To measure the data, all images were masked with polygons to identify particles manually, as shown in Figure 30, and were then fed into a Dunin-Borkowski algorithm to identify particle diameters by

approximating particle areas to a circle and calculating the associated diameter. The Fe film gradients produced a range of average particle sizes that roughly correlated with the thickness of the Fe film.

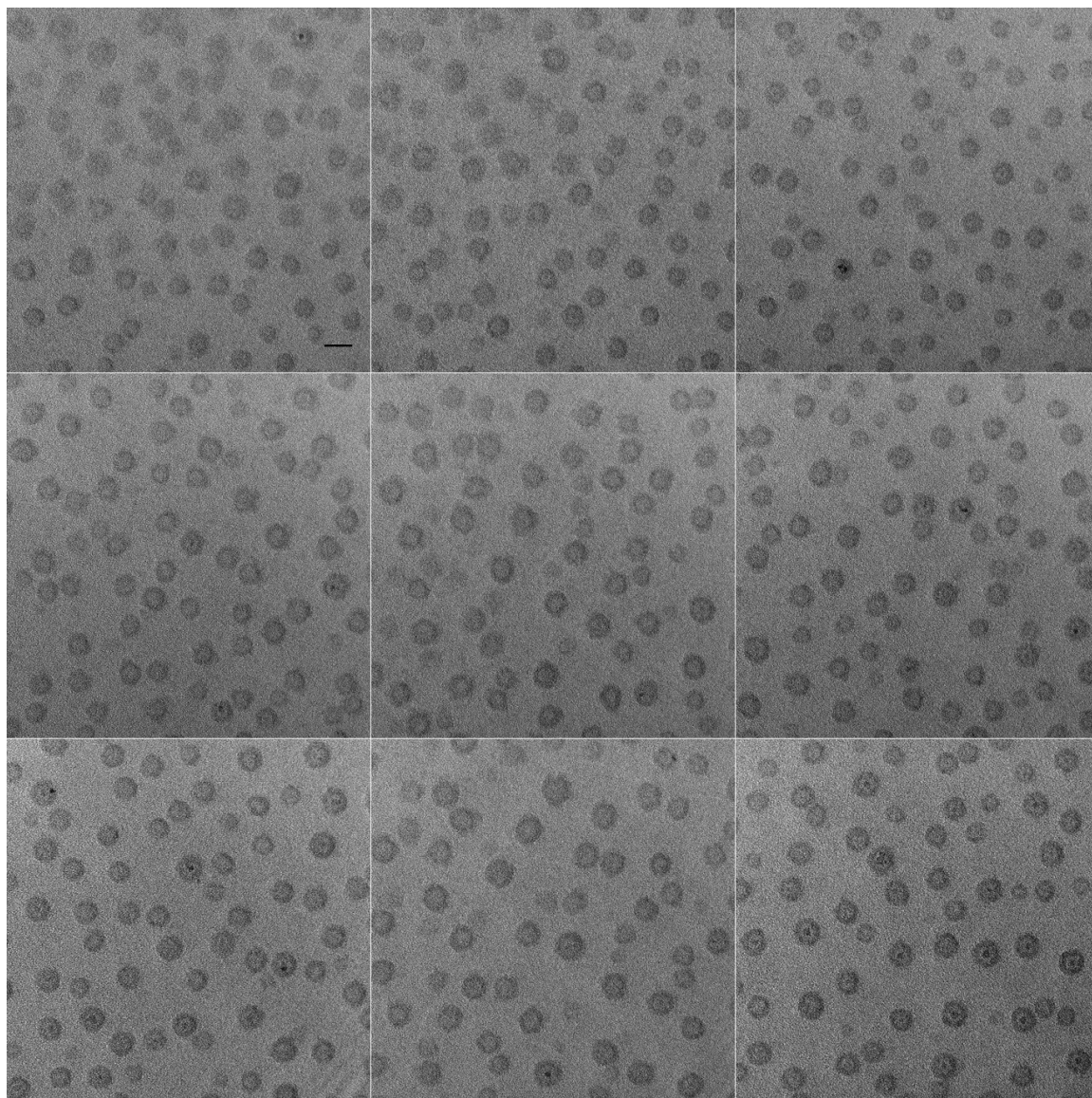


Figure 24 – Set of images from the Fe gradient sample A2, all taken at 255,000x magnification. The top, middle, and bottom rows are sets of 3 images from a Fe film thickness of 0.3 nm, 0.4 nm, and 0.5 nm, respectively. The scale bar, seen in the top left image, is 10 nm.

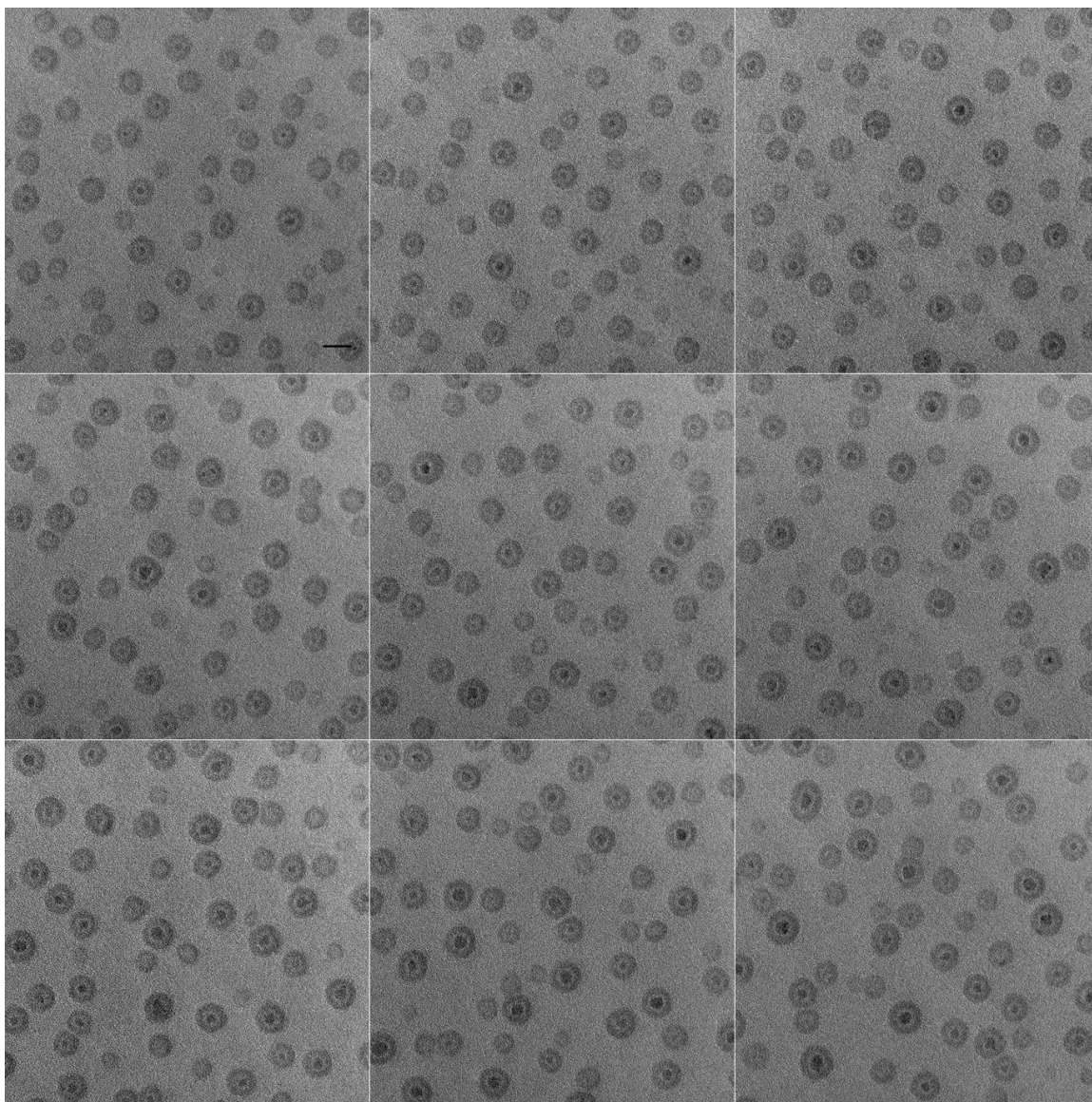


Figure 25 – Set of images from the Fe gradient sample A2, all taken at 255,000x magnification. The top, middle, and bottom rows are sets of 3 images from a Fe film thickness of 0.6 nm, 0.7 nm, and 0.8 nm, respectively. The scale bar, seen in the top left image, is 10 nm.

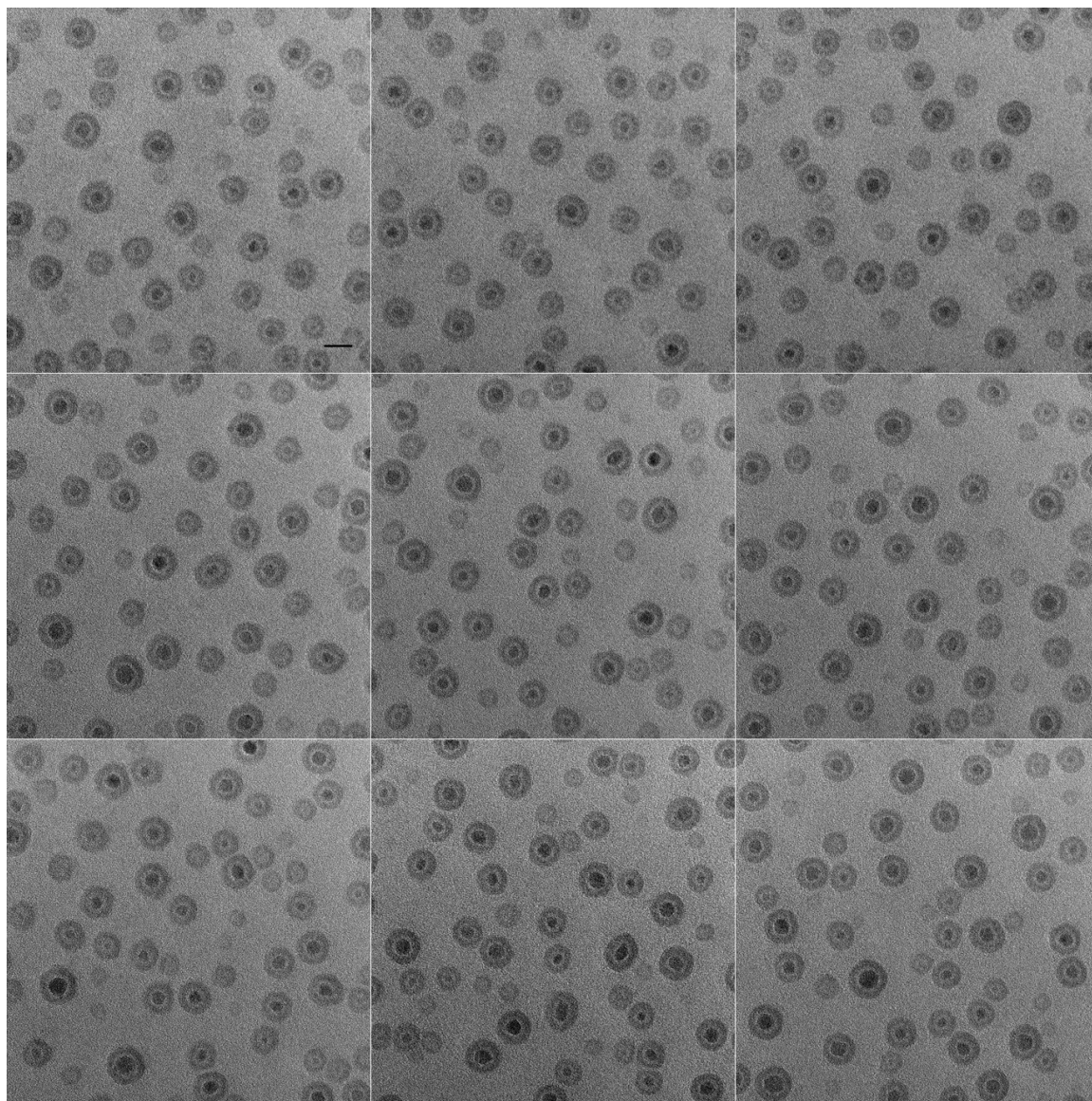


Figure 26 - Set of images from the Fe gradient sample A2, all taken at 255,000x magnification. The top, middle, and bottom rows are sets of 3 images from a Fe film thickness of 0.9 nm, 1.0 nm, and 1.1 nm, respectively. The scale bar, seen in the top left image, is 10 nm.



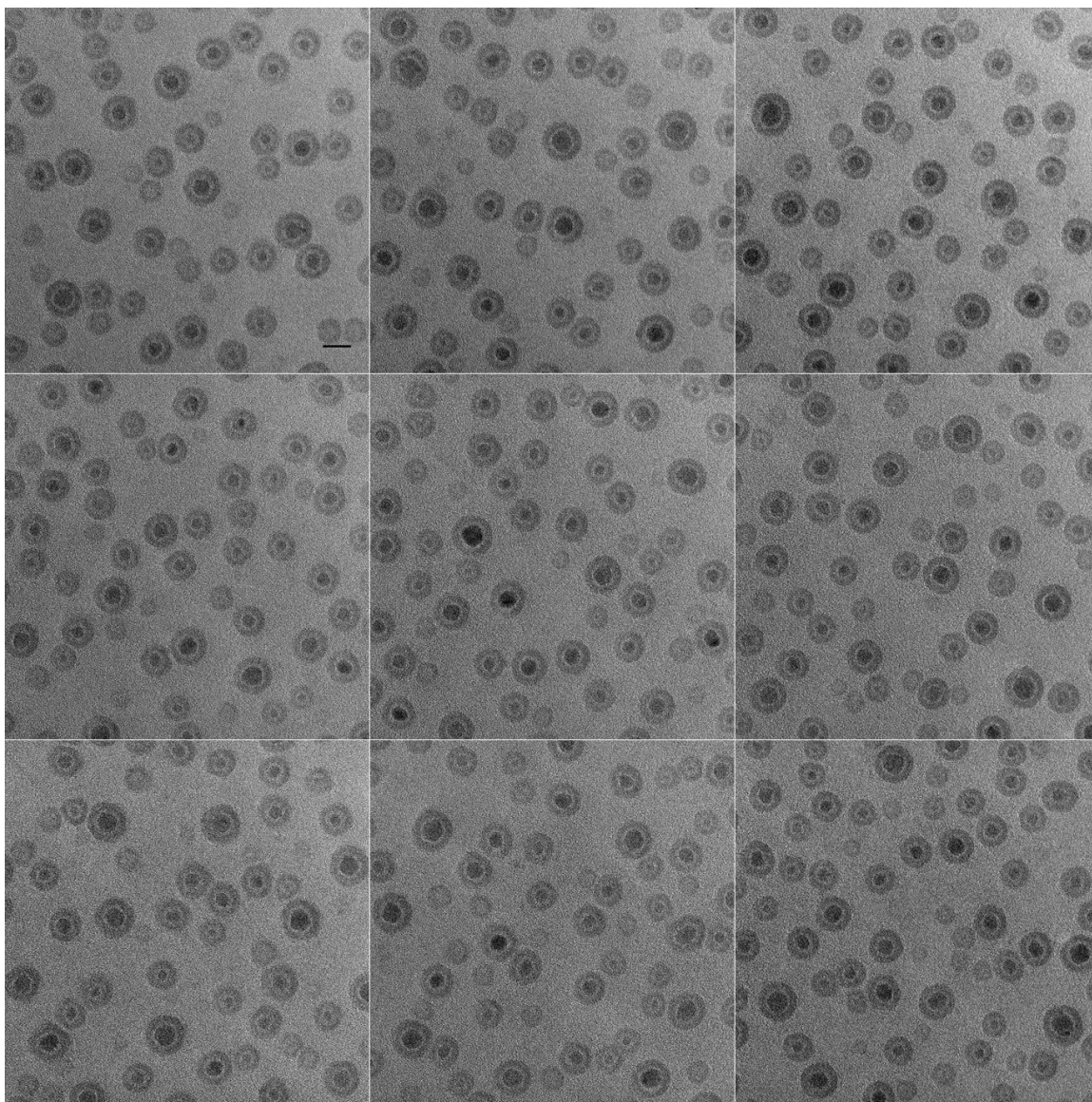


Figure 27 - Set of images from the Fe gradient sample A2, all taken at 255,000x magnification. The top, middle, and bottom rows are sets of 3 images from a Fe film thickness of 1.2 nm, 1.3 nm, and 1.4 nm, respectively. The scale bar, seen in the top left image, is 10 nm.

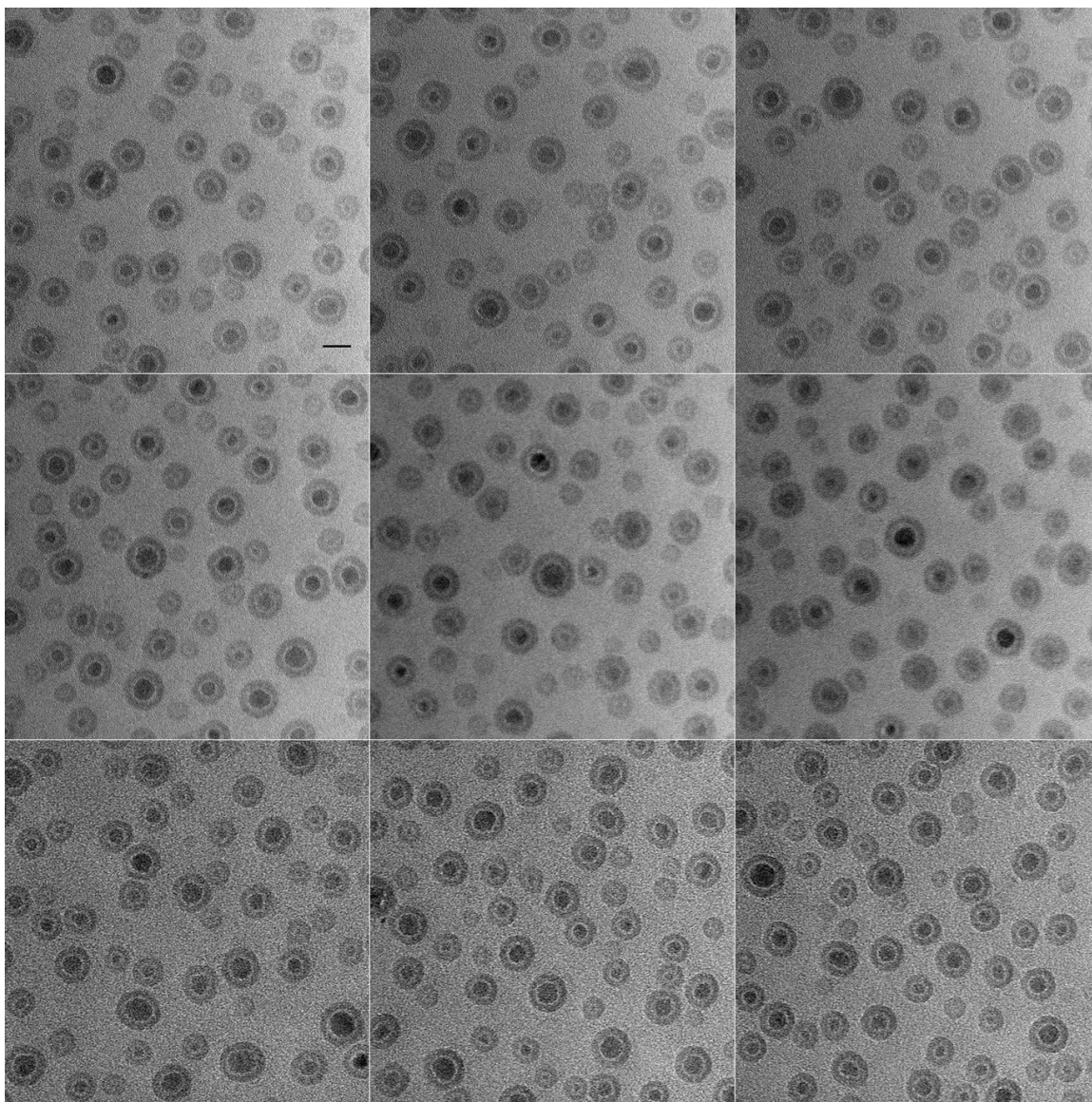


Figure 28 - Set of images from the Fe gradient sample A2, all taken at 255,000x magnification. The top, middle, and bottom rows are sets of 3 images from a Fe film thickness of 1.5 nm, 1.6 nm, and 1.7 nm, respectively. The scale bar, seen in the top left image, is 10 nm.

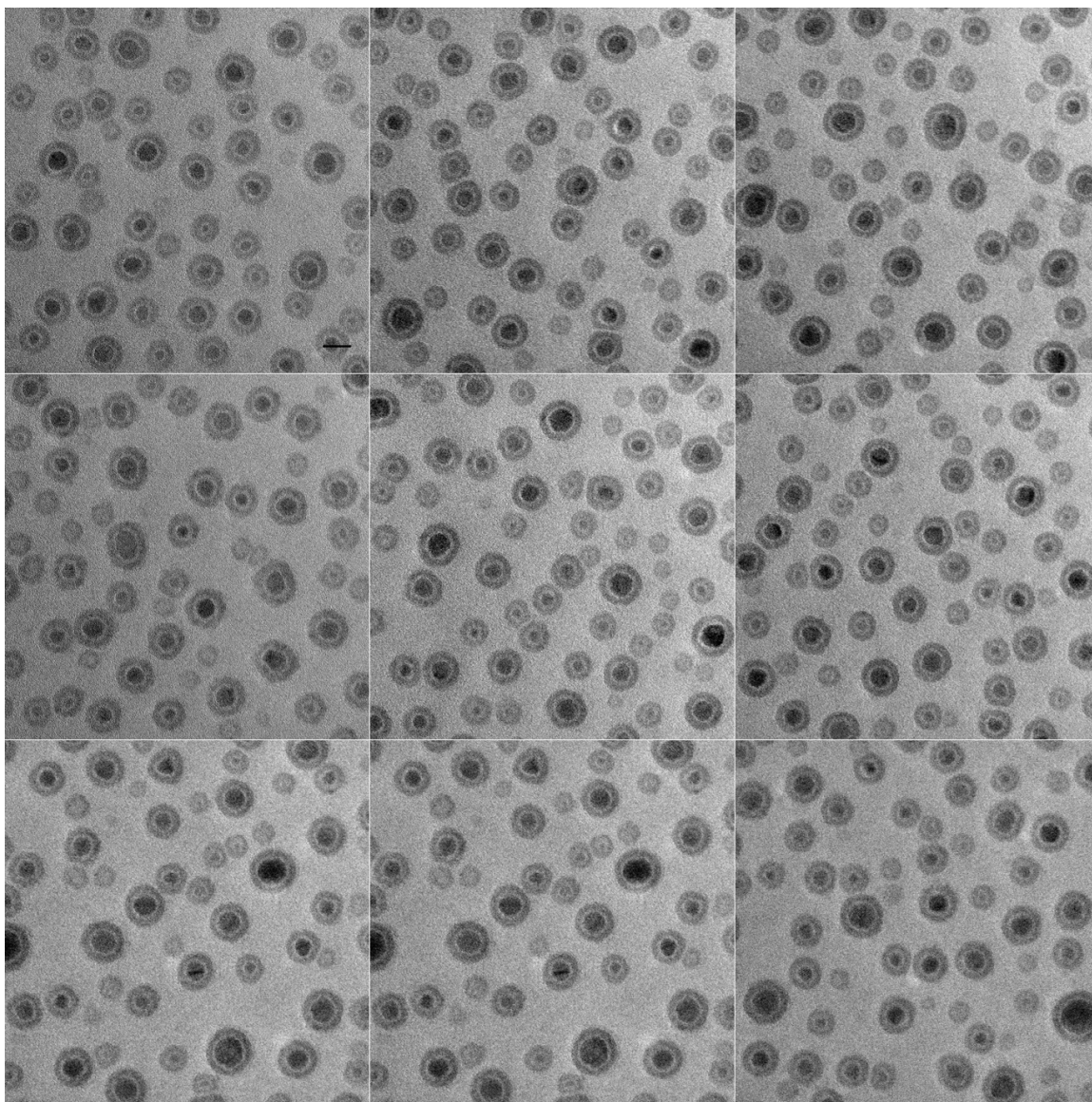


Figure 29 - Set of images from the Fe gradient sample A2, all taken at 255,000x magnification. The top, middle, and bottom rows are sets of 3 images from a Fe film thickness of 1.8 nm, 1.9 nm, and 2.0 nm, respectively. The scale bar, seen in the top left image, is 10 nm.



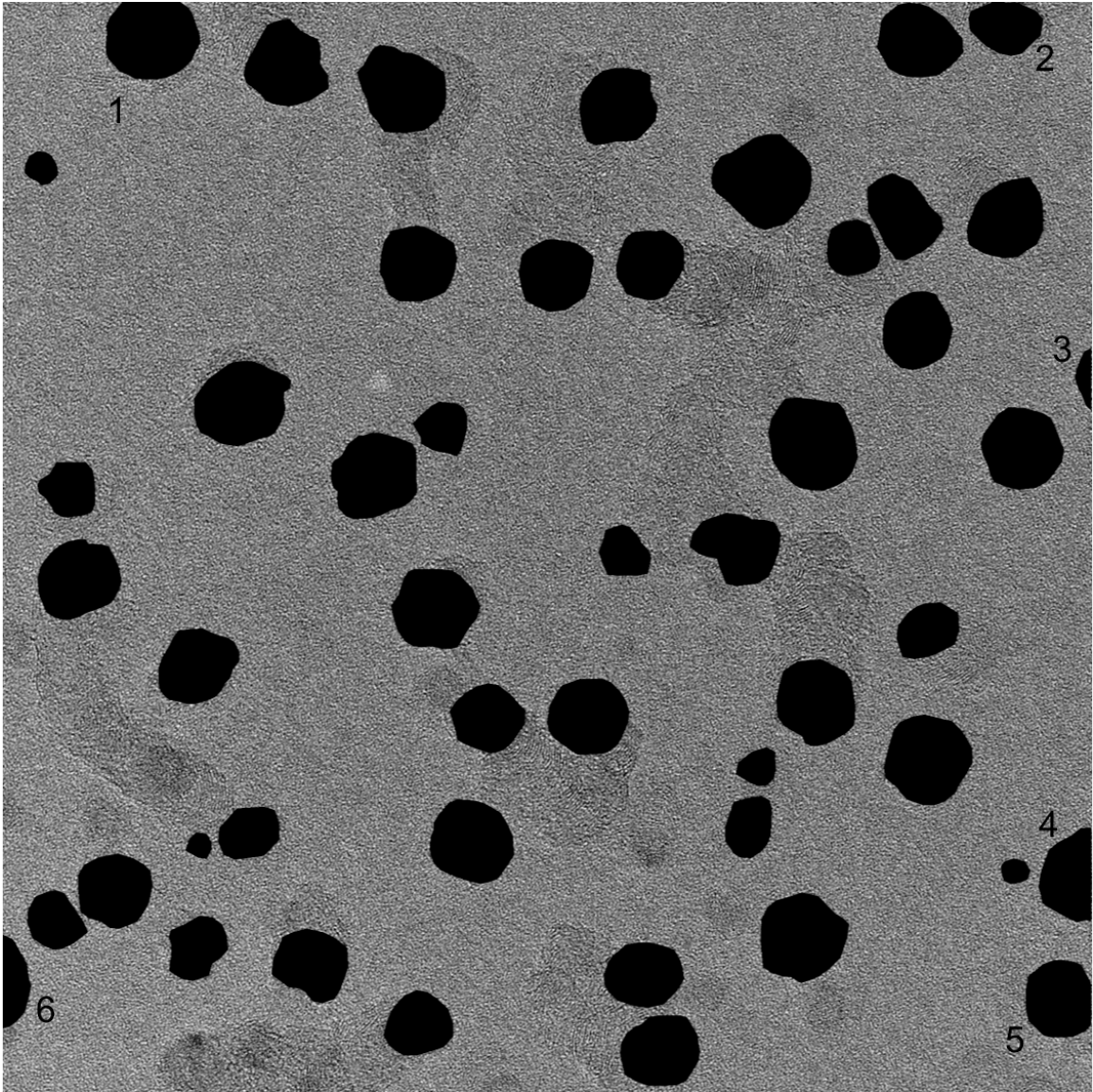


Figure 30 - Sample image from the 1.0 nm film thickness on sample A2 displayed for the purpose of explaining the particle analysis procedure. Particles were manually masked with polygons or ovals and then fed into a Matlab script running the Dunin-Borkowski algorithm. Six particles are numbered on the edge, and they would all be counted as half particles, only to be included in the particle density statistics and not the particle diameter statistics.

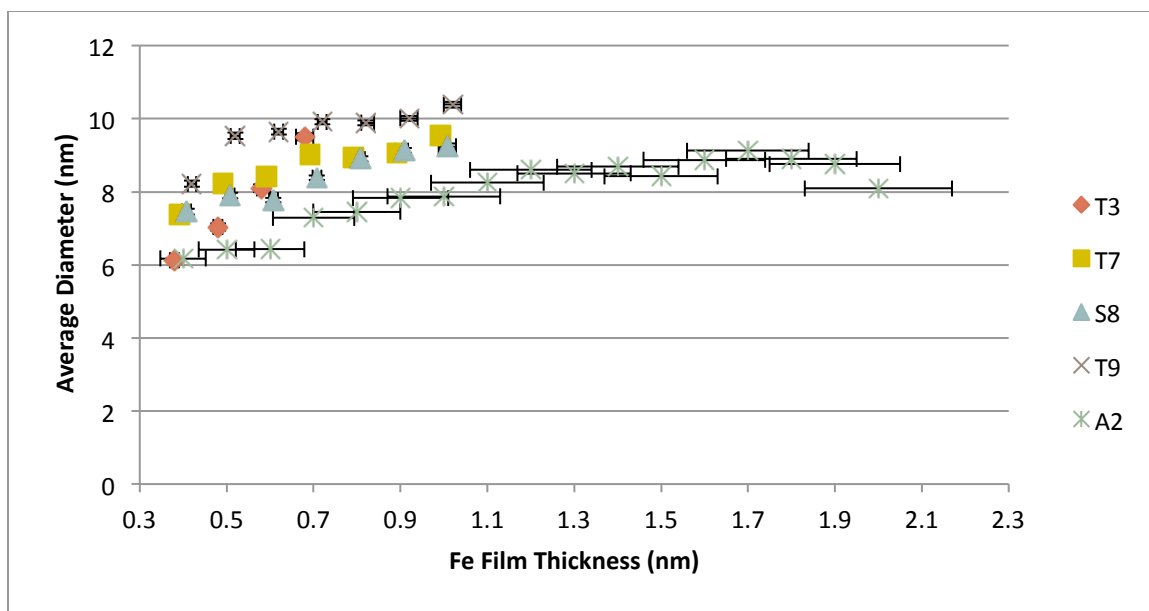


Figure 31 - Average particle diameter in nm (y-axis) versus Fe gradient film thickness in nm (x-axis).

All referenced data from samples T3, T7, S8, and T9, from now on, may be found in the appendix. In sample A2, between thicknesses 1.3 and 2.0 nm, the average particle size varies quite largely. This is due to the bimodal distribution that arises at these larger thicknesses. Below 1.3 nm, there is a steady decrease in the average particle size up until around 0.6 nm. The particles in the thicker film regions have a clear core-shell structure, with an iron core and an oxide shell that is a result of these particles being exposed to air. This core-oxide shell structure was confirmed in scanning TEM (STEM). Below about 0.5 nm, more particles appear to have no core-shell structure, flat contrast, and an irregular shape (non-oval/circular).

Sample T3 exhibits a very clear bimodal distribution above 0.4 nm film thickness, as shown in Figures 32-39, while the other samples do not. The reason for this difference is

not completely understood. Sample T3 had iron deposited on it at a very shallow gradient. This resulted in only thicknesses of 0.3 nm – 0.7 nm being observed in the microscope.

Average particle density was also measured, ranging from about 2000 – 3500 particles per square micron. This data was deliberately left out because, despite a general trend of increasing particle density with increasing iron film thickness, there is no agreement or tighter consistency in the data.

When Ostwald ripening occurs, it is expected that the average particle size increases over time, as it is energetically favorable for large particles to grow at the expense of smaller particles. If this were to occur, then histograms of average particle size would show a tail trailing off the bulk of the data toward larger particles. This is not observed in the histogram data. Given that the particles were annealed in hydrogen for only ten minutes, it is likely that Ostwald ripening has not even had the chance to become a dominating phenomenon.

Particle size error was calculated using the standard error of the mean method where  $SE = \frac{\sigma}{\sqrt{n}}$ , where  $SE$  is the standard error of the mean,  $\sigma$  is the standard deviation, and  $n$  is the number of measurements. In addition, x-axis error bars, or error in position, were calculated by comparing the error in the position measured by the electron probe micro-analyzer used to profile the samples with the slope of the film thickness.

Given that this sample is a gradient, there is some uncertainty related to the position along the gradient. The  $\text{Si}_3\text{N}_4$  TEM slot windows are made by back etching silicon with a thin layer of  $\text{Si}_3\text{N}_4$  deposited on the surface. Given that silicon is so highly utilized and understood, and any etching process, most likely utilizing some kind of mixture of nitric or hydrofluoric acid, would be highly regular, the error in finding the position of a film thickness along the length of the wall from any irregularities in the structure of the sidewall (*i.e.* curvature or the sidewall length not being parallel to the length of the slot) is likely trivial. The major source of error in determining the position of film thicknesses would be from the computer controlling TEM stage movement. This error was determined by noting the  $(x,y)$  location of two opposite corners of the slot and then moving back and forth between those positions to record the change in the  $(x,y)$  position of those corners. This gave an upper estimate of about 6  $\mu\text{m}$  in stage movement error in the FEI Titan. In the CM 200, the error in stage movement was less than 1 micron. While this seems surprising that the error was less on the older microscope, this was because sample movement on the CM 200 was done manually at the same magnification, completely out of necessity, but on the Titan, stage movement was done digitally by entering coordinates to travel to into the software. It can be safely assumed that error in TEM sample position is proportional to the distance the TEM sample is being moved.

#### 6.4 Discussion

Gradients were utilized to find any indications of catalyst morphological anomalies that would explain VA-CNT growth turn on at iron film thicknesses less than 1.0 nm. While nothing obvious was observed, a slight discontinuity between 0.4 nm and 0.5 nm can be

observed from Figures 32, 34, 40 and 42. In addition, there is a striking difference between the histograms of sample T3 and the rest of the samples. To understand what might be causing this, the data was segmented by structure. The most striking feature of the particles was the core-shell structure some exhibited and others did not. The segmented data is displayed in Figures 32 – 82. Quite surprisingly, a clear and consistent pattern emerged where core-shell particles displayed separate Gaussian-like histograms and were most often larger than non-core shell particles. One might argue that core shell particles are naturally going to appear larger due to their bulky oxide shell, but non core shell particles most often display flat or patchy contrast indicating the particle might be completely oxidized. In addition, this separation in average particle size between core-shell and non-core-shell particles appears to widen with increasing film thickness. If there was a random distribution of core-shell particles, then a clear and consistent pattern would not be expected to emerge.

Our current hypothesis for this phenomenon is that there is a particle size threshold for catalysts to reduce. Catalysts that reduce completely, or to a large degree, re-oxidize when exposed to air when they are removed from the CVD furnace and created the core-shell structure. Catalysts that are too small to reduce are likely interacting too strongly with the substrate and remain oxidized while being exposed to reducing conditions. Again, a counter argument might that the non-core shell particles also seem to increase in size with increasing film thickness. So, it is not necessarily a hard catalyst size limit that determines whether it will reduce or not. It may be due to nearest neighbor effects or there may be more segments of particle structure that are being missed in the images.

In addition to segmenting by core-shell structure, roundness may be another method by which the particle data could be segmented. Many particles appeared to have different morphologies. Most particles were round, but some were faceted and some had odd curvature in its features. Both roundness and circularity are distinct measurements, which indicate different aspects curvature of a particle. Circularity is the ratio of  $\frac{4\pi*area}{perimeter^2}$  and roundness is the ratio of  $\frac{4*area}{\pi*major\ axis^2}$ , where the major axis is the long axis if the object is fitted to an ellipse. Furthermore, there are different ways to measure particle size. The method used in this study finds the diameter of a particle to be, that which would fit a perfect circle of equal area. Another way to measure particle size is by measuring the Feret's diameter, or the longest distance between two parallel, tangential lines to the perimeter of the particle. Further data segmentation is an obvious choice when trying to determine if there are any other distinct phenomena which may be affecting the creation and development of catalyst particles.

Lastly, how this relates to CNT growth is unclear. It is known that CNT growth is not very efficient in terms of the percentage of catalysts that are created that actually nucleate and grown a CNT. This segmentation of core-shell/non-core-shell particles may be a result of the inability of catalysts to reduce, which, as a result, do not nucleate CNTs.

## CHAPTER 7. FUTURE WORK AND CONCLUSIONS

The study of carbon nanotube growth is extensive enough that it can be easy to become boxed into the study of carbon, how its forms nucleate, and how they grow. However, it is important to realize that CNT growth, at least through CVD, is a heterogeneous catalyst system. This means that the phase of the catalyst differs from that of the reactants<sup>100</sup>. What this implies is that results discovered through the research of CNT growth are largely applicable to the greater catalysis world in general. Specifically, all of the preliminary results discussed within this dissertation have potential applications within the greater heterogeneous catalysis community.

Chapter 4 focused on the potential influence of the inert gas environment on catalyst morphology when multiple gaseous species are involved. The work is based on previous findings that iron catalysts on alumina tend to grow metallic nanotubes in the presence of helium and semiconducting nanotubes in the presence of argon. This behavior was correlated with catalyst morphology through *in-situ* TEM studies showing that a small iron nanoparticle in the presence of a small amount of water and helium exhibits strong facets and becomes more rounded when exposed to a mixture of argon and water. In addition, it has also been shown that water is effective at inhibiting Ostwald ripening, a mechanism of CNT growth termination, and Ostwald ripening rates are higher in iron/alumina catalyst/support systems when annealed in

argon as opposed to helium. These results suggest that Ostwald ripening might be used as a qualitative measurement of the degree of faceting in a catalyst system. However, it is still unclear whether this strong catalyst faceting behavior in helium is a result of the ability of the inert gas to transfer momentum to the catalyst particle and its adsorbates and knock off any adsorbed hydroxyl or oxygen or if this is due to impurities within the gaseous environment, as it has been shown that ppm impurity levels can have a significant effect on CNT growth behavior.

To discern the cause of the faceting behavior in the iron/alumina system, Ostwald ripening tests of catalyst particles with controlled mass flux of the inert gas are proposed. A positive result showing increased Ostwald ripening rates at higher inert gas mass fluxes would indicate that increasing the mass flux of an inert gas interferes with the ability of water to inhibit Ostwald ripening, and could result in more rounded and less faceted catalyst particles. This disruption of water's ability to inhibit Ostwald ripening would likely be due to the ability of the individual inert gas species to transfer momentum to adsorbates on the surface of the catalyst particle and knock them away. Any potential influences of ppm level impurities could be mitigated by observing increased Ostwald ripening rates in catalyst systems with heavily increased mass flow rates of helium, the lightest species which is least effective at transferring momentum to the adsorbates.

Preliminary data has shown that Ostwald ripening rates decrease with increasing amounts of water, and rates increase with increasing pressure of argon without the



presence of water. Past work has shown that increased Ostwald ripening rates in the catalyst system are not likely due to evaporation of the catalyst material, but more likely due to increased atom mobility on the surface of the substrate.

Further tests should be completed to test the ability of heavier inert gases such as argon or xenon to influence Ostwald ripening rates in the presence of water. In addition, if tests show no dependence on mass flow of inert gases then the next step would be to search for impurities within inert gasses that cause the catalyst faceting behavior.

Next, work was presented highlighting the ability to tune the surface chemistry and morphology of catalyst support substrates through ion beam bombardment. Sapphire, a substrate which does not support VA-CNT growth, was turned into a catalytically active substrate through bombarding the surface with an argon ion beam. Specifically, the ion beam increased the number of active oxygen sites on the surface by increasing the relative OH<sup>-</sup> concentration and the relative O 1s to Al 2p peak ratio. Cross-sectional TEM was used to characterize the nature of the damage. Two layers were observed. A top amorphous layer was found, which is the layer that supports the catalyst particles, and a second crystalline interfacial layer was seen to exist in between the top amorphous layer and the sapphire substrate.

By catalytically activating previously unsuitable substrates for VA-CNT growth, the possibilities exist to attempt similar procedures on other substrates and using other ion beams to tune the substrate chemistry and topography.

Lastly, iron gradients were studied in an attempt to draw conclusions about catalyst development and morphology for CNT growth. It is known that small, uniform catalyst arrays are necessary for CNT growth and CNT growth seems to turn on at small catalyst sizes. So, it is logical to try and observe sudden changes in catalyst morphology at critical sizes near where CNT growth starts.

To study this behavior, an iron gradient thickness film was deposited on a TEM grid covered in a small amount of IBS silica. The tested samples in this body of work exhibited a core-shell structure and were mostly rounded the entire length of the gradient, making it impossible to determine potential changes in catalyst morphology due to changes in deposited iron film thickness. However, a discontinuity in the average particle size was observed along the length of the gradient, which is not immediately expected. In addition, segmenting the particles by whether or not they show a core-shell structure revealed clear, consistent, and distinct data sets.

The questions arising from this iron gradient study are perfectly suited for in-situ TEM experiments. Specifically, it should be attempted to observe newly formed catalyst particles reduce. Electron energy loss spectroscopy could potentially be utilized to measure the degree to which an ensemble of catalysts or individual catalysts reduce or do not reduce. Taking in-situ measurements gives the benefit of observing particle structure and orientation as it is reducing. This data would be invaluable in answering the question “why do some catalysts nucleate CNTs and some do not?” Specifically, for the main catalyst materials for CNT growth, iron,

cobalt, and nickel, their  $L_{2,3}$  EELS edges may be measured to determine the reduction state of the catalyst.

Lastly, the gradient experiments were performed on IBS silica, but alumina is the best support choice for iron due to the metal's affinity for the specific oxide. Repeating these experiments on alumina would be enlightening if catalyst/support interaction is preventing some catalysts from reducing and nucleating CNTs on silica.

## LIST OF REFERENCES

## LIST OF REFERENCES

1. Moore, G. E. *Cramming More Components Onto Integrated Circuits*. (1965).
2. Mollick, E. Establishing Moore's Law. *Annals of the History of Computing, IEEE* **28**, 62–75 (2006).
3. Kanellos, M. Moore says Moore's Law to hit wall. *www.news.cnet.com* (1997). at <<http://news.cnet.com/2100-1001-203750.html>>
4. Iijima, S. Helical microtubules of graphitic carbon. *Nature* (1991).
5. Yakobson, B. I. & Avouris, P. in *Carbon Nanotubes* **80**, 287–327 (Springer Berlin Heidelberg, 2001).
6. Behabtu, N. *et al.* Strong, Light, Multifunctional Fibers of Carbon Nanotubes with Ultrahigh Conductivity. *Science* **339**, 182–186 (2013).
7. Wong, E. W. Nanobeam Mechanics: Elasticity, Strength, and Toughness of Nanorods and Nanotubes. *Science* **277**, 1971–1975 (1997).
8. Qu, L., Dai, L., Stone, M., Xia, Z. & Wang, Z. L. Carbon Nanotube Arrays with Strong Shear Binding-On and Easy Normal Lifting-Off. *Science* **322**, 238–242 (2008).
9. Yao, Z., Kane, C. & Dekker, C. High-Field Electrical Transport in Single-Wall Carbon Nanotubes. *Phys. Rev. Lett.* **84**, 2941–2944 (2000).
10. Zhou, X., Park, J.-Y., Huang, S., Liu, J. & McEuen, P. Band Structure, Phonon Scattering, and the Performance Limit of Single-Walled Carbon Nanotube Transistors. *Phys. Rev. Lett.* **95**, 146805 (2005).
11. Avouris, P., Freitag, M. & Perebeinos, V. Carbon-nanotube photonics and optoelectronics. *Nature Photon* **2**, 341–350 (2008).
12. Baughman, R. H. Carbon Nanotubes--the Route Toward Applications. *Science* **297**, 787–792 (2002).
13. Iijima, S. Helical microtubules of graphitic carbon. *Nature* **354**, 56–58 (1991).
14. Ebbesen, T. W. *et al.* Electrical conductivity of individual carbon nanotubes. , *Published online: 04 July 1996; | doi:10.1038/382054a0* **382**, 54–56 (1996).
15. Dresselhaus, M. S., Dresselhaus, G. & Eklund, P. C. *Science of Fullerenes and Carbon Nanotubes*. (Academic Press, 1996).
16. Bethune, D. S., Klang, C. H., De Vries, M. S. & Gorman, G. Cobalt-catalysed growth of carbon nanotubes with single-atomic-layer walls. (1993).
17. Iijima, S. & Ichihashi, T. Single-shell carbon nanotubes of 1-nm diameter. (1993).
18. Tans, S. J., Verschueren, A. & Dekker, C. Room-temperature transistor based on a single carbon nanotube. *Nature* (1998).
19. Baughman, R. H., Zakhidov, A. A. & de Heer, W. A. Carbon Nanotubes--the Route Toward Applications. *Science* **297**, 787–792 (2002).

20. Martel, R., Schmidt, T., Shea, H. R., Hertel, T. & Avouris, P. Single- and multi-wall carbon nanotube field-effect transistors. *Appl. Phys. Lett.* **73**, 2447–2449 (1998).
21. Bonard, J. X. M. *et al.* Field emission from single-wall carbon nanotube films. *Appl. Phys. Lett.* **73**, 918–920 (1998).
22. Journet, C., Maser, W. K., Bernier, P. & Loiseau, A. Large-scale production of single-walled carbon nanotubes by the electric-arc technique. *Nature* (1997).
23. Thess, A., Lee, R., Nikolaev, P. & Dai, H. Crystalline ropes of metallic carbon nanotubes. ... *AAAS-Weekly Paper* ... (1996).
24. Rinzler, A. G. *et al.* Large-scale purification of single-wall carbon nanotubes: process, product, and characterization. *Appl Phys A* **67**, 29–37 (1998).
25. Li, W. Z. *et al.* Large-scale synthesis of aligned carbon nanotubes. *Science* (1996).
26. Endo, M., Takeuchi, K., Igarashi, S. & Kobori, K. The production and structure of pyrolytic carbon nanotubes (PCNTs). *Journal of physics and ...* (1993).
27. Ivanov, V., Nagy, J. B., Lambin, P., Lucas, A. & Zhang, X. B. The study of carbon nanotubules produced by catalytic method. *Chemical Physics* ... (1994).
28. Jose x2010 Yacaman, M., Miki x2010 Yoshida, M., Rendon, L. & Santiesteban, J. G. Catalytic growth of carbon microtubules with fullerene structure. *Appl. Phys. Lett.* **62**, 657–659 (1993).
29. Dai, H., Wong, E. W., Lu, Y. Z., Fan, S. & Lieber, C. M. Synthesis and characterization of carbide nanorods. *Nature* (1995).
30. Wong, E. W., Maynor, B. W. & Burns, L. D. Growth of metal carbide nanotubes and nanorods. *Chemistry of ...* (1996).
31. Cassell, A., Raymakers, J., Kong, J. & Dai, H. *Large scale single-walled nanotubes by CVD synthesis*. (J. Phys. Chem, 1999).
32. Eklund, P., Ajayan, P., Blackmon, R., Hart, A. J. & Kibng, J. International assessment of research and development of carbon nanotube manufacturing and applications. (2007).
33. Nessim, G. D. Properties, synthesis, and growth mechanisms of carbon nanotubes with special focus on thermal chemical vapor deposition. *Nanoscale* **2**, 1306–1323 (2010).
34. Choi, G. S., Cho, Y. S., Hong, S. Y., Kim, D. & Choi, S. Y. Characterization of Fe-catalyzed carbon nanotubes grown by thermal chemical vapor deposition. *Journal of Crystal ...* (2002).
35. Moisala, A., Nasibulin, A. G. & Kauppinen, E. I. The role of metal nanoparticles in the catalytic production of single-walled carbon nanotubes—a review. *J. Phys.: Condens. Matter* **15**, S3011–S3035 (2003).
36. de los Arcos, T., Garnier, M. G. & Seo, J. W. The influence of catalyst chemical state and morphology on carbon nanotube growth. *The Journal of ...* (2004).
37. Namai, T., Hata, K., Futaba, D. N., Mizuno, K. & Fan, J. Size-selective growth of double-walled carbon nanotube forests from engineered iron catalysts. *Nature* (2006).

38. Nessim, G. D., Hart, A. J., Kim, J. S., Acquaviva, D. & Oh, J. Tuning of vertically-aligned carbon nanotube diameter and areal density through catalyst pre-treatment. *Nano ...* (2008).
39. Li, J. *et al.* Growth of High-Density-Aligned and Semiconducting-Enriched Single-Walled Carbon Nanotubes: Decoupling the Conflict between Density and Selectivity. *ACS ...* (2013).
40. Bethune, D. S., Kiang, C. H., Devries, M., Gorman, G. & Savoy, R. *The discovery of single-wall carbon nanotubes at IBM.* (Nature, 1993).
41. Teo, K. B. K. *et al.* Uniform patterned growth of carbon nanotubes without surface carbon. *Appl. Phys. Lett.* **79**, 1534–1536 (2001).
42. Wen, H.-C. *et al.* Carbon nanotubes grown using cobalt silicide as catalyst and hydrogen pretreatment. *Microelectronic Engineering* **82**, (2005).
43. Ren, Z. F. *et al.* Growth of a single freestanding multiwall carbon nanotube on each nanonickel dot. *Appl. Phys. Lett.* **75**, 1086–1088 (1999).
44. Ho, G. W., Wee, A., Lin, J. & Tjiu, W. C. Synthesis of well-aligned multiwalled carbon nanotubes on Ni catalyst using radio frequency plasma-enhanced chemical vapor deposition. *Thin Solid Films* (2001).
45. Chhowalla, M. *et al.* Growth process conditions of vertically aligned carbon nanotubes using plasma enhanced chemical vapor deposition. *J. Appl. Phys.* **90**, 5308 (2001).
46. Kumar, M. Carbon Nanotube Synthesis and Growth Mechanism. *Carbon Nanotubes - Synthesis, Characterization, Applications* (2011). doi:10.5772/19331
47. Bhaviripudi, S., Mile, E., Steiner, S. A. & Zare, A. T. CVD synthesis of single-walled carbon nanotubes from gold nanoparticle catalysts. *Journal of the ...* (2007).
48. Lee, C. J., Lyu, S. C., Kim, H. W., Park, C. Y. & Yang, C. W. Large-scale production of aligned carbon nanotubes by the vapor phase growth method. *Chemical Physics Letters* (2002).
49. Hart, A. J., Hofmann, S. & Wardle, B. L. Nanoscale zirconia as a nonmetallic catalyst for graphitization of carbon and growth of single-and multiwall carbon nanotubes. *Journal of the ...* (2009).
50. Delzeit, L., Chen, B., Cassell, A. & Stevens, R. Multilayered metal catalysts for controlling the density of single-walled carbon nanotube growth. *Chemical Physics ...* (2001).
51. Ding, F. *et al.* The Importance of Strong Carbon–Metal Adhesion for Catalytic Nucleation of Single-Walled Carbon Nanotubes. *Nano Lett.* **8**, 463–468 (2008).
52. Amama, P. B. *et al.* Influence of Alumina Type on the Evolution and Activity of Alumina-Supported Fe Catalysts in Single-Walled Carbon Nanotube Carpet Growth. *ACS Nano* **4**, 895–904 (2010).
53. Pint, C. L., Kim, S. M., Stach, E. A. & Hauge, R. H. Rapid and scalable reduction of dense surface-supported metal-oxide catalyst with hydrazine vapor. *ACS Nano* (2009).

54. Schaper, A. K., Hou, H., Greiner, A. & Phillipp, F. The role of iron carbide in multiwalled carbon nanotube growth. *Journal of Catalysis* (2004).
55. Yoshida, H., Takeda, S., Uchiyama, T. & Kohno, H. Atomic-scale in-situ observation of carbon nanotube growth from solid state iron carbide nanoparticles. *Nano ...* (2008).
56. Harutyunyan, A. R., Tokune, T. & Mora, E. Liquefaction of catalyst during carbon single-walled nanotube growth. *Appl. Phys. Lett.* **86**, 153113–153113 (2005).
57. Harutyunyan, A. R., Tokune, T. & Mora, E. Liquid as a required catalyst phase for carbon single-walled nanotube growth. *Appl. Phys. Lett.* **87**, 051919–051919 (2005).
58. Terrones, M., Terrones, H. & Kroto, H. W. In situ nucleation of carbon nanotubes by the injection of carbon atoms into metal particles. *Nature* (2007).
59. Chiang, W. H. & Sankaran, R. M. Linking catalyst composition to chirality distributions of as-grown single-walled carbon nanotubes by tuning  $\text{Ni}_x\text{Fe}_{1-x}$  nanoparticles. *Nat Mater* (2009).
60. Pinault, M., Mayne-L'Hermite, M. & Reynaud, C. Carbon nanotubes produced by aerosol pyrolysis: growth mechanisms and post-annealing effects. *Diamond and related ...* (2004).
61. Hata, K. *et al.* Water-Assisted Highly Efficient Synthesis of Impurity-Free Single-Walled Carbon Nanotubes. *Science* **306**, 1362–1364 (2004).
62. Li, J. *et al.* Growth of High-Density-Aligned and Semiconducting-Enriched Single-Walled Carbon Nanotubes: Decoupling the Conflict between Density and Selectivity. *ACS ...* (2013).
63. Harutyunyan, A. R. *et al.* Preferential Growth of Single-Walled Carbon Nanotubes with Metallic Conductivity. *Science* **326**, 116–120 (2009).
64. Pint, C. L., Pheasant, S. T., Pasquali, M. & Coulter, K. E. Synthesis of high aspect-ratio carbon nanotube ‘flying carpets’ from nanostructured flake substrates. *Nano ...* (2008).
65. Lifshitz, I. M. & Slyozov, V. V. The kinetics of precipitation from supersaturated solid solutions. *Journal of Physics and Chemistry of Solids* (1961).
66. Wagner, C. *Wagner: Theory of aging by precipitation coarsening - Google Scholar*. (Z. Elektrochem, 1961).
67. Kim, S. M. *et al.* Evolution in Catalyst Morphology Leads to Carbon Nanotube Growth Termination. *J. Phys. Chem. Lett.* **1**, 918–922 (2010).
68. Williams, D. B. & Carter, C. B. in *Transmission Electron Microscopy* 3–17 (Springer US, 1996). doi:10.1007/978-1-4757-2519-3\_1
69. Colthup, N. B., Daly, L. H. & Wiberley, S. E. *Introduction to infrared and Raman spectroscopy*. (1990).
70. Dresselhaus, M. S., Dresselhaus, G. & Jorio, A. Raman spectroscopy on isolated single wall carbon nanotubes. *Carbon* **40**, 2043–2061 (2002).
71. Dresselhaus, M. S., Dresselhaus, G., Saito, R. & Jorio, A. Raman spectroscopy of carbon nanotubes. *Physics Reports* **409**, 47–99 (2005).
72. Rottman, C. & Wortis, M. Equilibrium crystal shapes for lattice models with nearest-and next-nearest-neighbor interactions. *Phys. Rev. B* (1984).



73. Gontard, L. C., Ozkaya, D. & Dunin-Borkowski, R. E. A simple algorithm for measuring particle size distributions on an uneven background from TEM images. *Ultramicroscopy* (2011).
74. Akimov, A. G. *INTERACTION OF WATER-VAPOR WITH AN IRON SURFACE ELECTRON-SPECTROSCOPIC INVESTIGATION*. (SOVIET ELECTROCHEMISTRY, 1979).
75. Smith, R. P. & Darken, L. S. *The Iron-Carbon Eutectoid Temperature*. (... , 1959).
76. Onink, M., Brakman, C. M. & Tichelaar, F. D. *The lattice parameters of austenite and ferrite in Fe–C alloys as functions of carbon concentration and temperature*. (Scripta metallurgica et ... , 1993).
77. Lang, N. D. & Kohn, W. Theory of metal surfaces: charge density and surface energy. *Phys. Rev. B* (1970).
78. Challa, S. R. *et al.* Relating Rates of Catalyst Sintering to the Disappearance of Individual Nanoparticles during Ostwald Ripening. *J. Am. Chem. Soc.* **133**, 20672–20675 (2011).
79. Fonda, G. R. Evaporation characteristics of tungsten. *Physical Review* (1923).
80. Fonda, G. R. Evaporation of tungsten under various pressures of argon. *Physical Review* (1928).
81. Adamson, A. W. & Gast, A. P. *Physical Chemistry of Surfaces, 1997, 315*. (John Wiley).
82. In, J. B., Grigoropoulos, C. P., Chernov, A. A. & Noy, A. Hidden role of trace gas impurities in chemical vapor deposition growth of vertically-aligned carbon nanotube arrays. *Appl. Phys. Lett.* **98**, 153102–153102 (2011).
83. Kucheyev, S. O. *et al.* Ion-beam-induced porosity of GaN. *Appl. Phys. Lett.* **77**, 1455–1457 (2000).
84. Eswaraiah, V. & Sankaranarayanan, V. Inorganic nanotubes reinforced polyvinylidene fluoride composites as low-cost electromagnetic interference shielding materials. *Nanoscale Res ...* (2011).
85. Chakrabarti, S., Kume, H. & Pan, L. Number of walls controlled synthesis of millimeter-long vertically aligned brushlike carbon nanotubes. *The Journal of ...* (2007).
86. Pint, C. L., Alvarez, N. T. & Hauge, R. H. Odako growth of dense arrays of single-walled carbon nanotubes attached to carbon surfaces. *Nano Res.* **2**, 526–534 (2009).
87. Huang, J.-Q., Zhang, Q., Zhao, M.-Q., Xu, G.-H. & Wei, F. Patterning of hydrophobic three-dimensional carbon nanotube architectures by a pattern transfer approach. *Nanoscale* **2**, 1401–1404 (2010).
88. Huang, J., Zhang, Q., Zhao, M. & Wei, F. Process intensification by CO<sub>2</sub> for high quality carbon nanotube forest growth: Double-walled carbon nanotube convexity or single-walled carbon nanotube bowls? *Nano Res.* (2009).
89. Golecki, I., Chapman, G. E., Lau, S. S., Tsaur, B. Y. & Mayer, J. W. Ion-beam induced epitaxy of silicon. *Physics Letters A* (1979).
90. Linnros, J., Svensson, B. & Holmen, G. Ion-beam-induced epitaxial regrowth of amorphous layers in silicon on sapphire. *Phys. Rev. B* (1984).

91. Canut, B., Benyagoub, A., Marest, G. & Meftah, A. Swift-uranium-ion-induced damage in sapphire. *Phys. Rev. B* (1995).
92. Amama, P. B., Putnam, S. A., Barron, A. R. & Maruyama, B. Wetting behavior and activity of catalyst supports in carbon nanotube carpet growth. *Nanoscale* **5**, 2642–2646 (2013).
93. Van den Brand, J., Sloof, W. G., Terryn, H. & de Wit, J. H. W. Correlation between hydroxyl fraction and O/Al atomic ratio as determined from XPS spectra of aluminium oxide layers. *Surface and Interface Analysis* **36**, 81–88 (2004).
94. Fan, S., Liang, W., Dang, H., Franklin, N. & Tomblor, T. Carbon nanotube arrays on silicon substrates and their possible application. *Physica E: Low- ...* (2000).
95. Wei, Y. Y., Eres, G. & Merkulov, V. I. Effect of catalyst film thickness on carbon nanotube growth by selective area chemical vapor deposition. *Appl. Phys. Lett.* (2001).
96. Kukovitsky, E. F., L'vov, S. G., Sainov, N. A. & Shustov, V. A. Correlation between metal catalyst particle size and carbon nanotube growth. *Chemical Physics ...* (2002).
97. Nasibulin, A. G., Pikhitsa, P. V., Jiang, H. & Kauppinen, E. I. Correlation between catalyst particle and single-walled carbon nanotube diameters. *Carbon* **43**, 2251–2257 (2005).
98. Voorhees, P. W. The theory of Ostwald ripening. *J Stat Phys* **38**, 231–252 (1985).
99. Börjesson, A. & Bolton, K. First principles studies of the effect of ostwald ripening on carbon nanotube chirality distributions. *ACS Nano* (2011).
100. Ross, J. R. H. *Heterogeneous Catalysis*. (Elsevier, 2012).

## APPENDIX

## APPENDIX

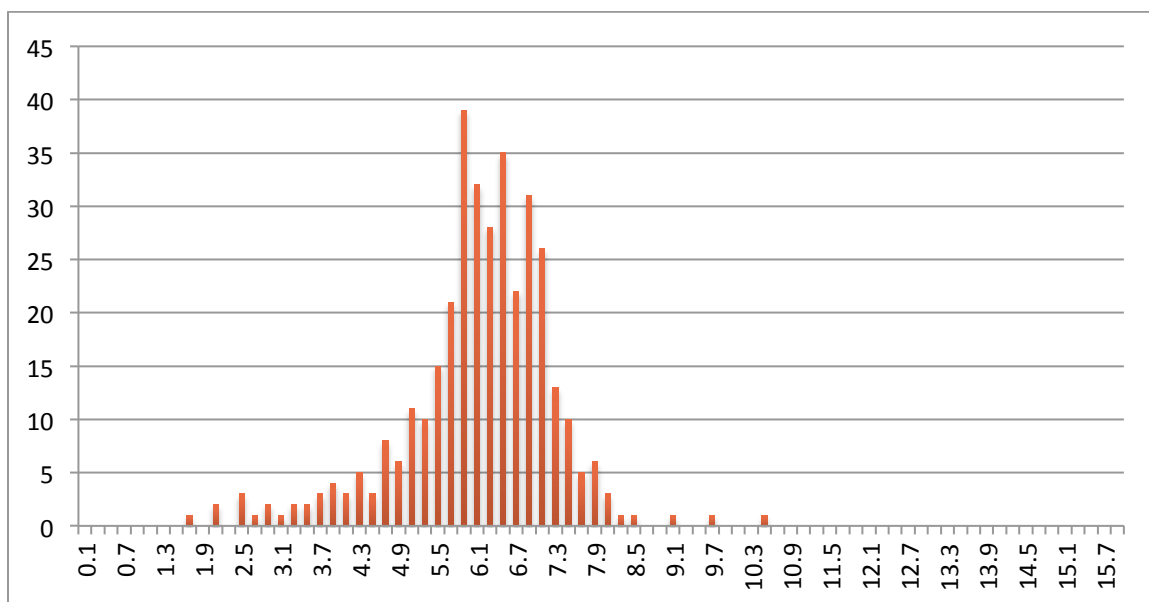


Figure A1 - Histogram of nanoparticle diameters at 0.4 nm film thickness of Sample T3.

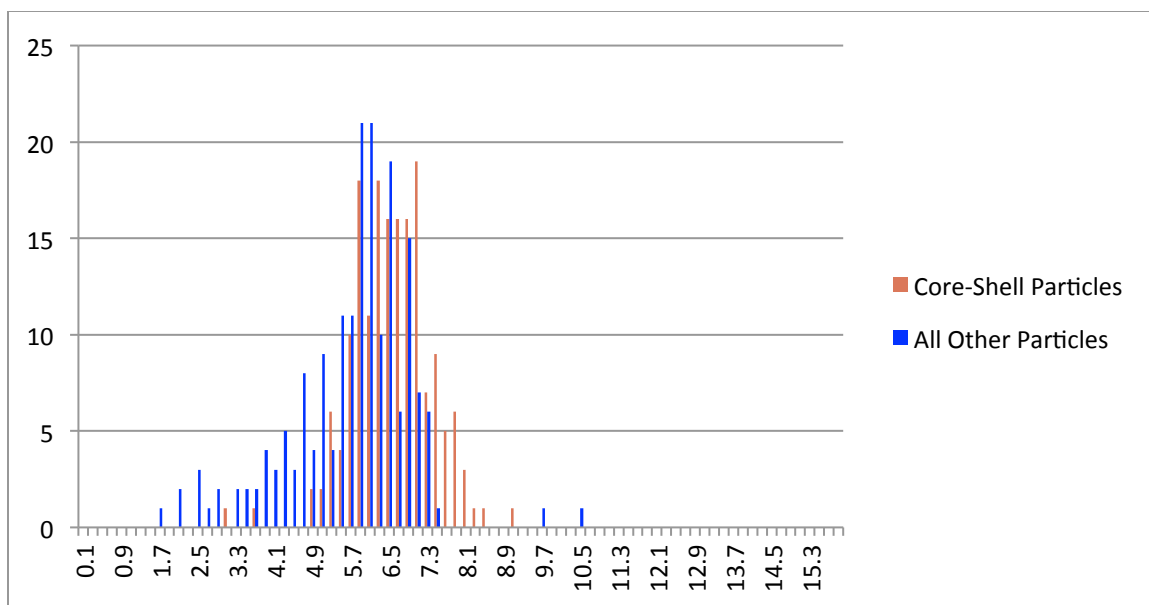


Figure A2 - Histogram of nanoparticle diameters at 0.4 nm film thickness of Sample T3 segmented by core-shell structure.

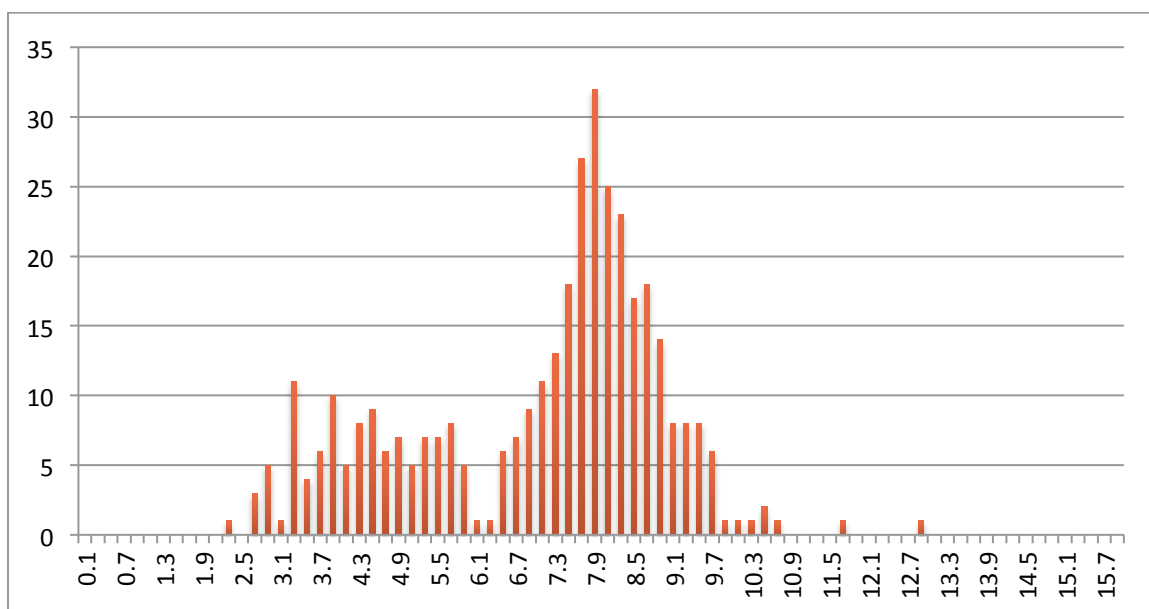


Figure A3 - Histogram of nanoparticle diameters at 0.5 nm film thickness of Sample T3.

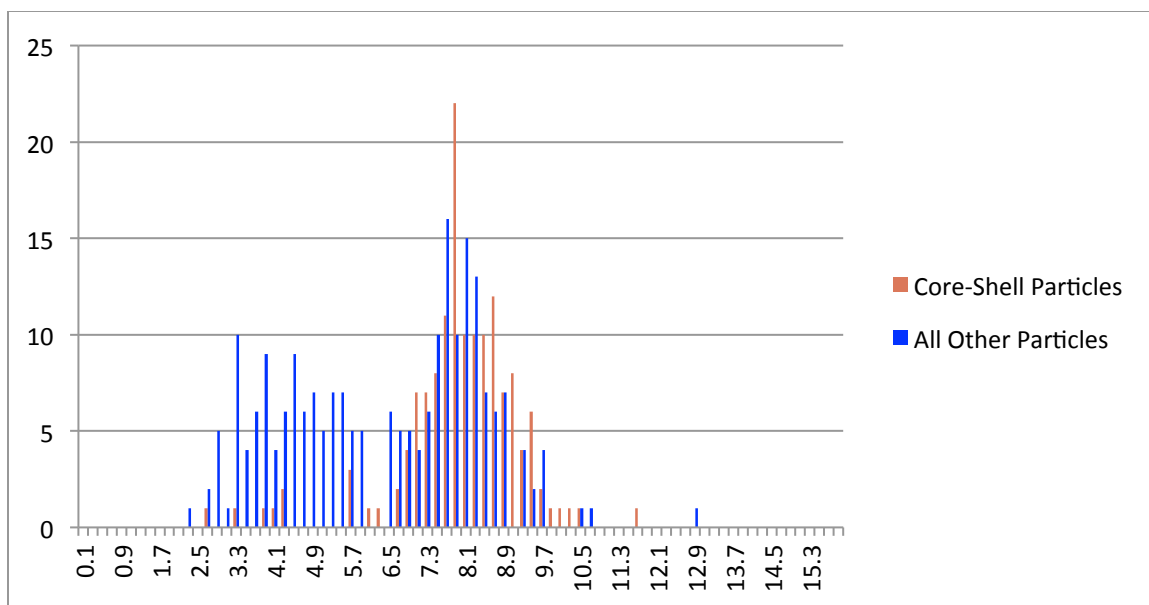


Figure A4 - Histogram of nanoparticle diameters at 0.5 nm film thickness of Sample T3 segmented by core-shell structure.

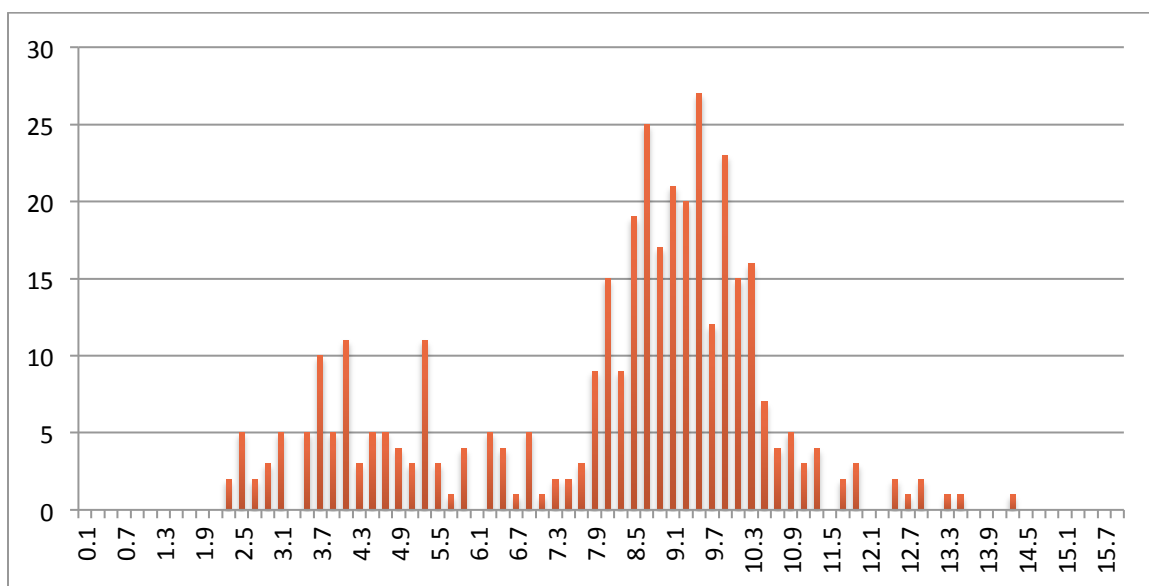


Figure A5 - Histogram of nanoparticle diameters at 0.6 nm film thickness of Sample T3.

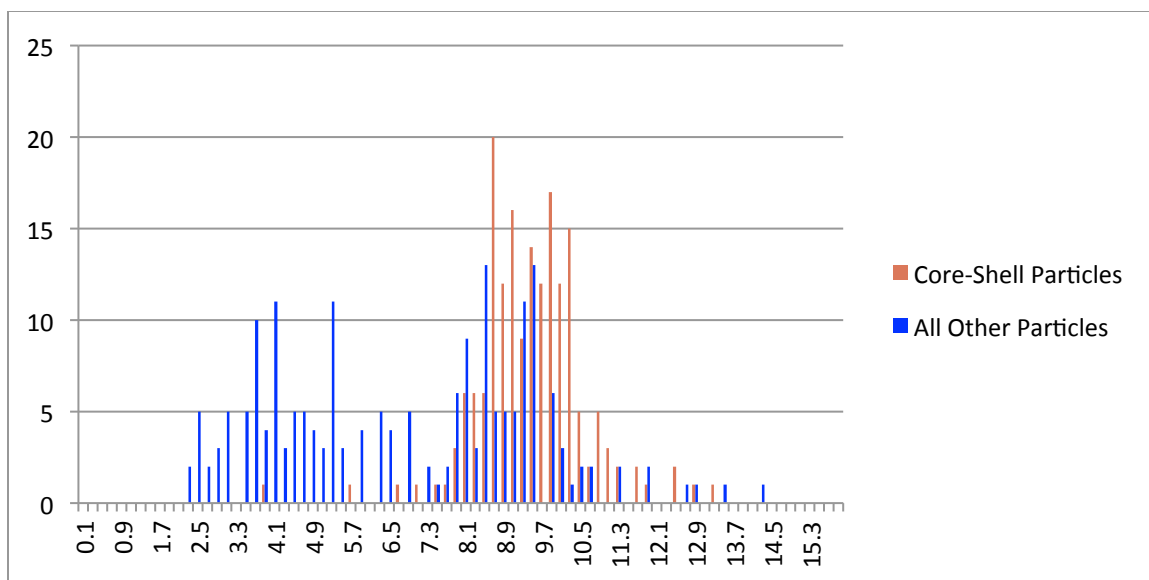


Figure A6 - Histogram of nanoparticle diameters at 0.6 nm film thickness of Sample T3 segmented by core-shell structure.

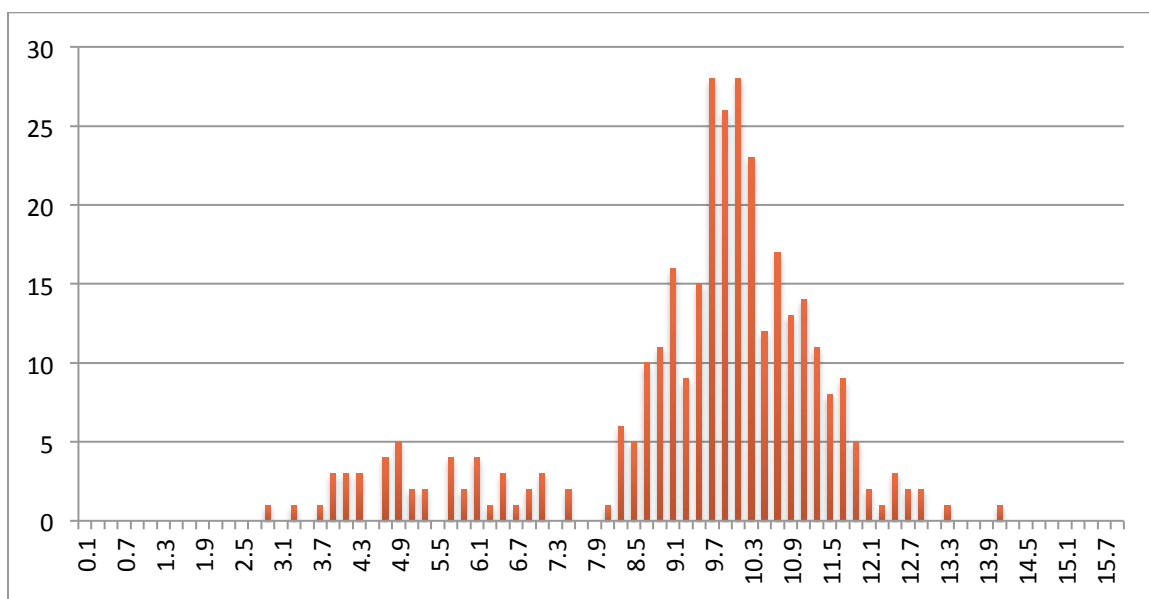


Figure A7 - Histogram of nanoparticle diameters at 0.7 nm film thickness of Sample T3.

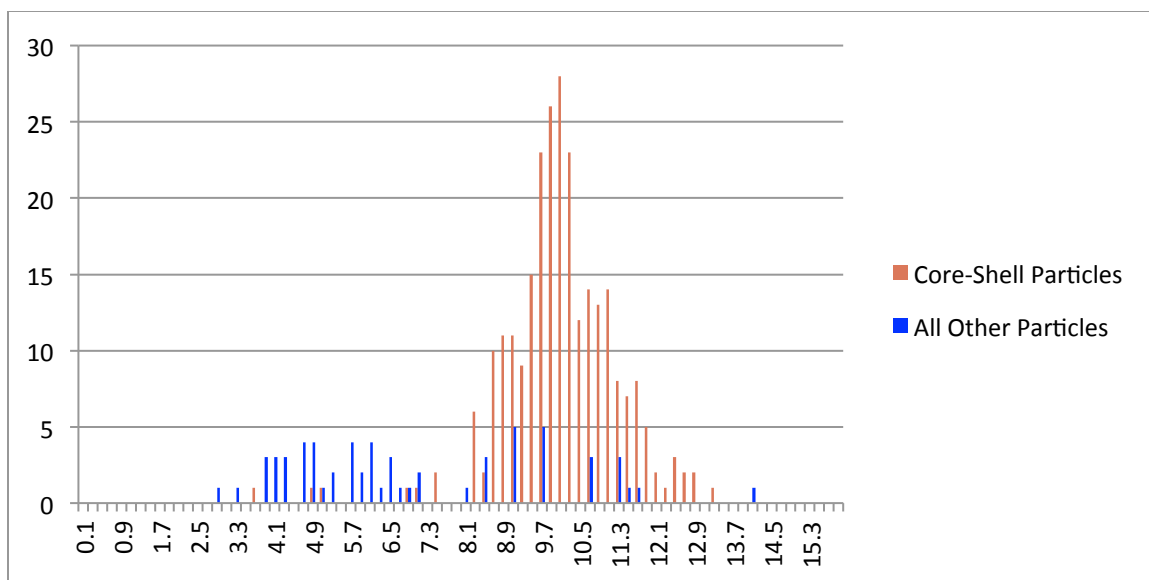


Figure A8 - Histogram of nanoparticle diameters at 0.7 nm film thickness of Sample T3 segmented by core-shell structure.

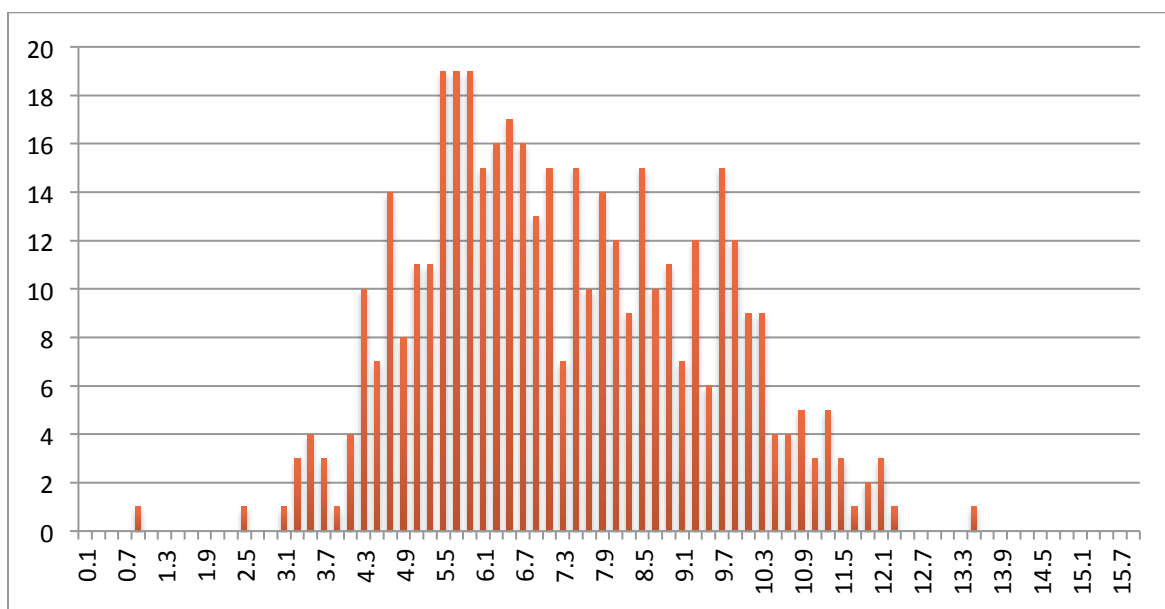


Figure A9 - Histogram of nanoparticle diameters at 0.4 nm film thickness of Sample T7.



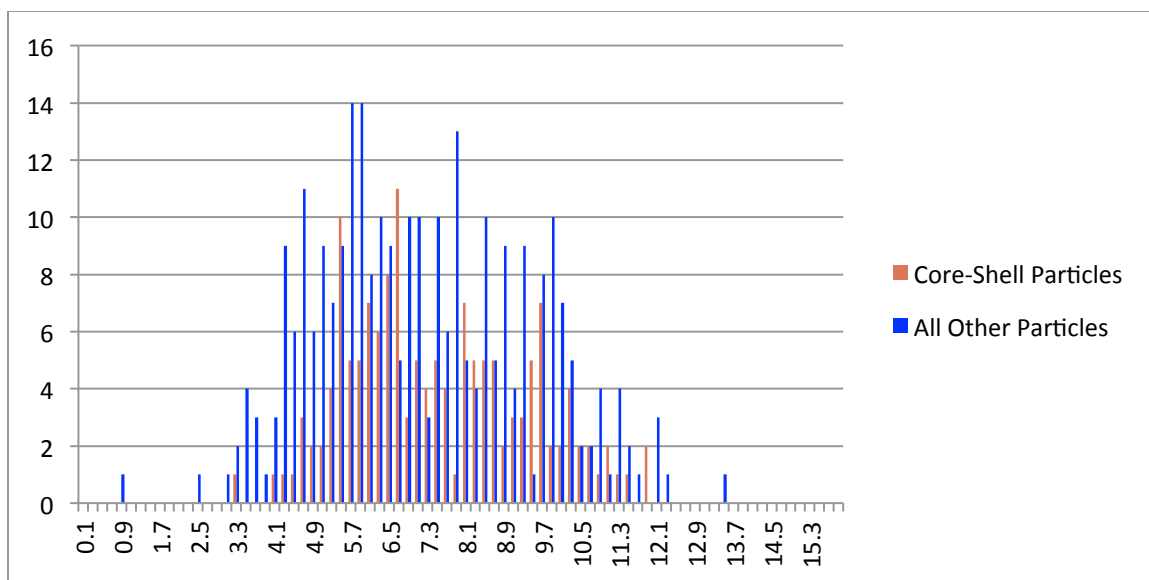


Figure A10 - Histogram of nanoparticle diameters at 0.4 nm film thickness of Sample T7 segmented by core-shell structure.

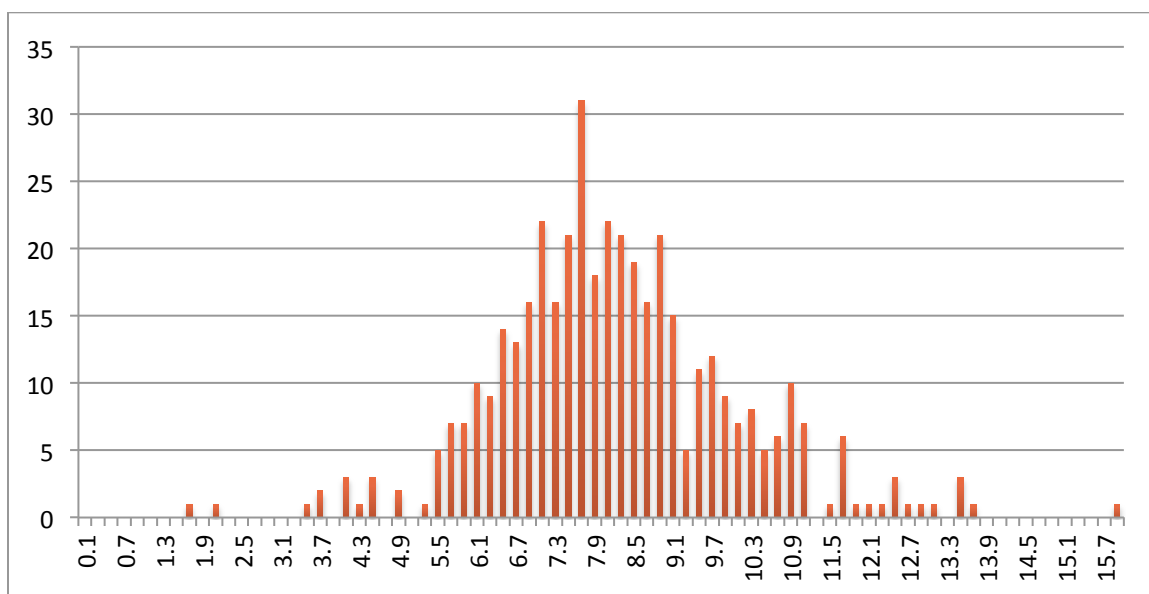


Figure A11 - Histogram of nanoparticle diameters at 0.5 nm film thickness of Sample T7.

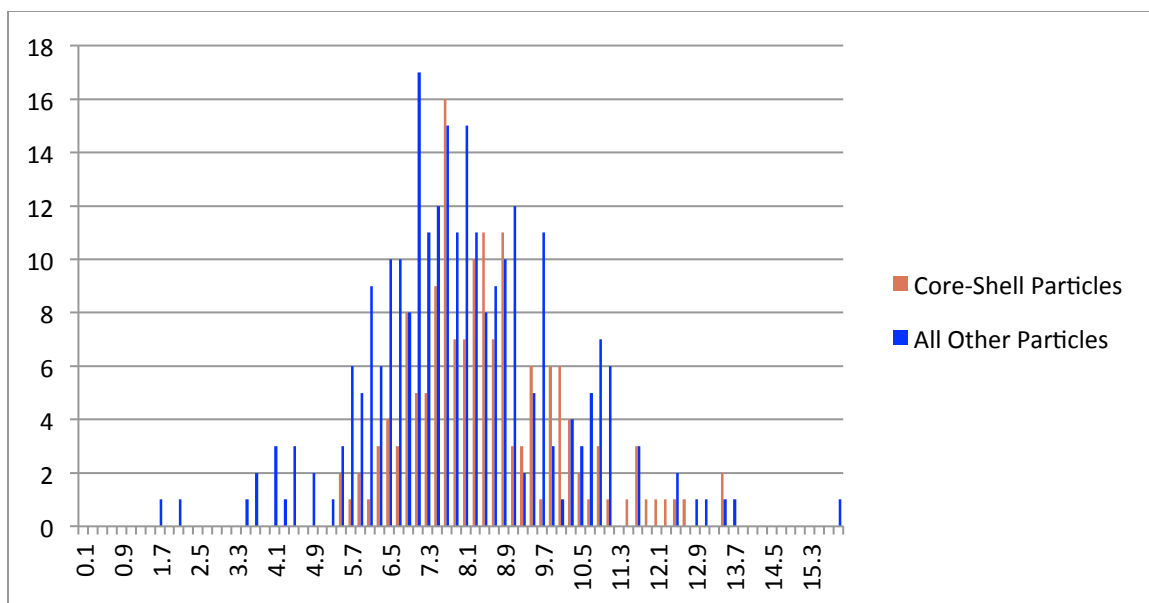


Figure A12 - Histogram of nanoparticle diameters at 0.5 nm film thickness of Sample T7 segmented by core-shell structure.

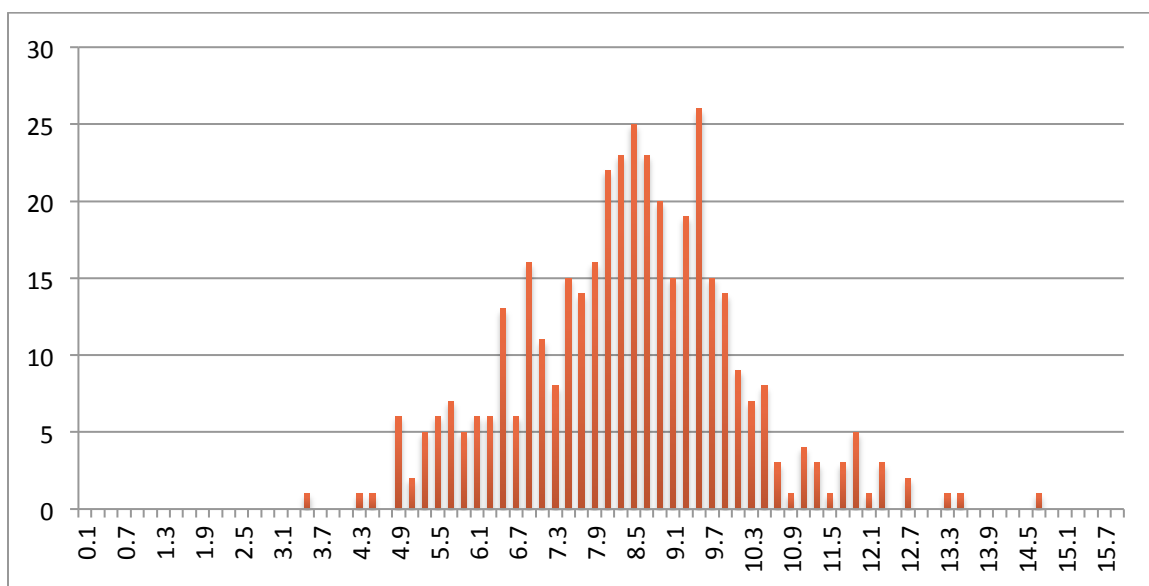


Figure A13 - Histogram of nanoparticle diameters at 0.6 nm film thickness of Sample T7.

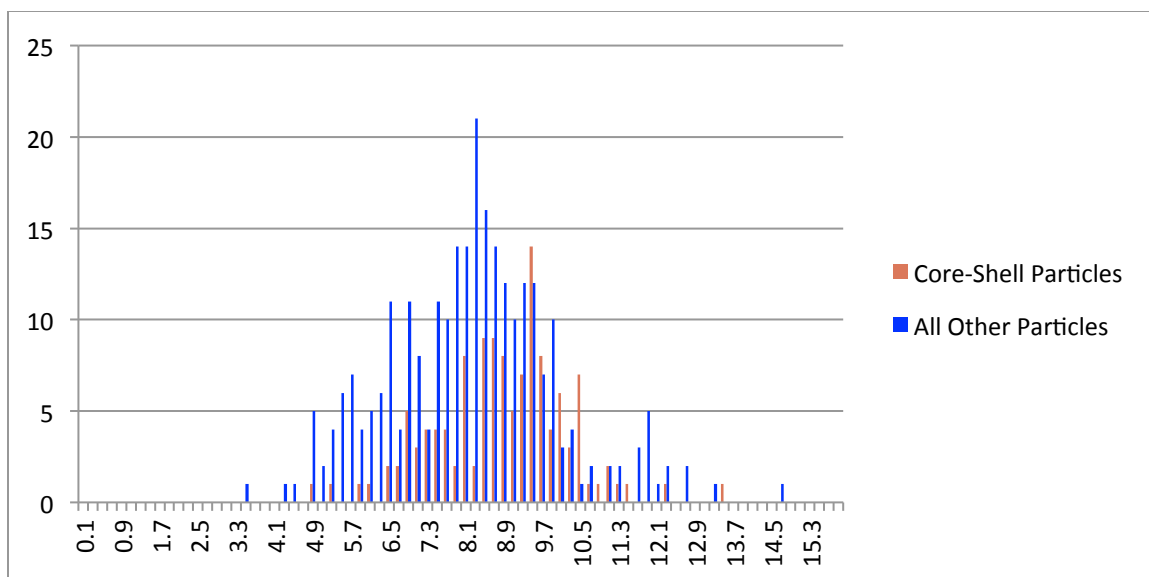


Figure A14 - Histogram of nanoparticle diameters at 0.6 nm film thickness of Sample T7 segmented by core-shell structure.

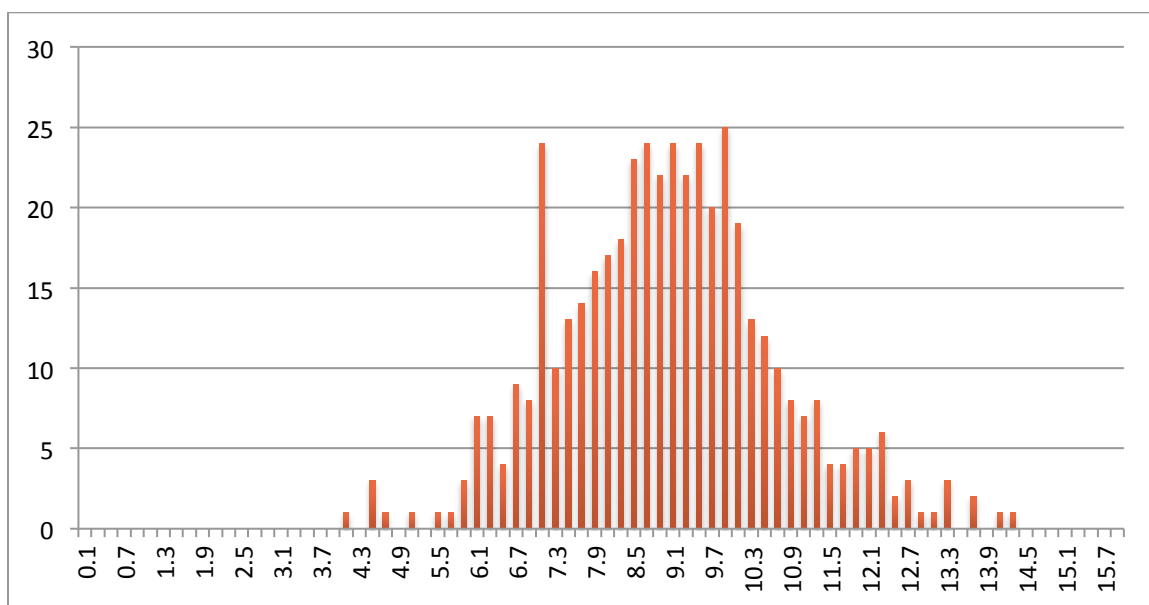


Figure A15 - Histogram of nanoparticle diameters at 0.7 nm film thickness of Sample T7.

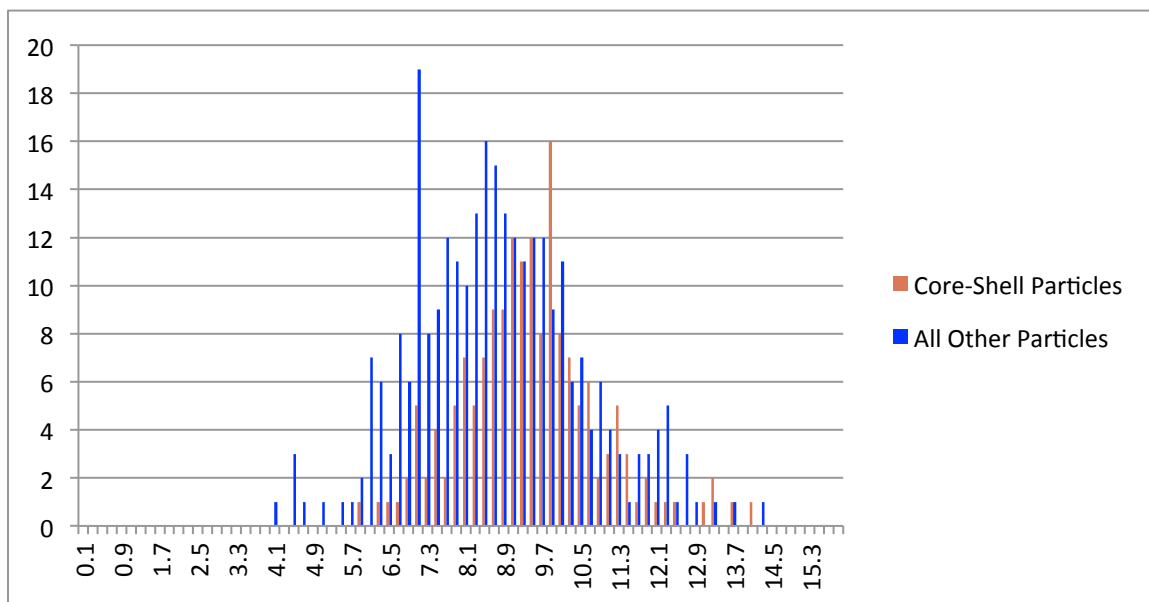


Figure A16 - Histogram of nanoparticle diameters at 0.7 nm film thickness of Sample T7 segmented by core-shell structure.

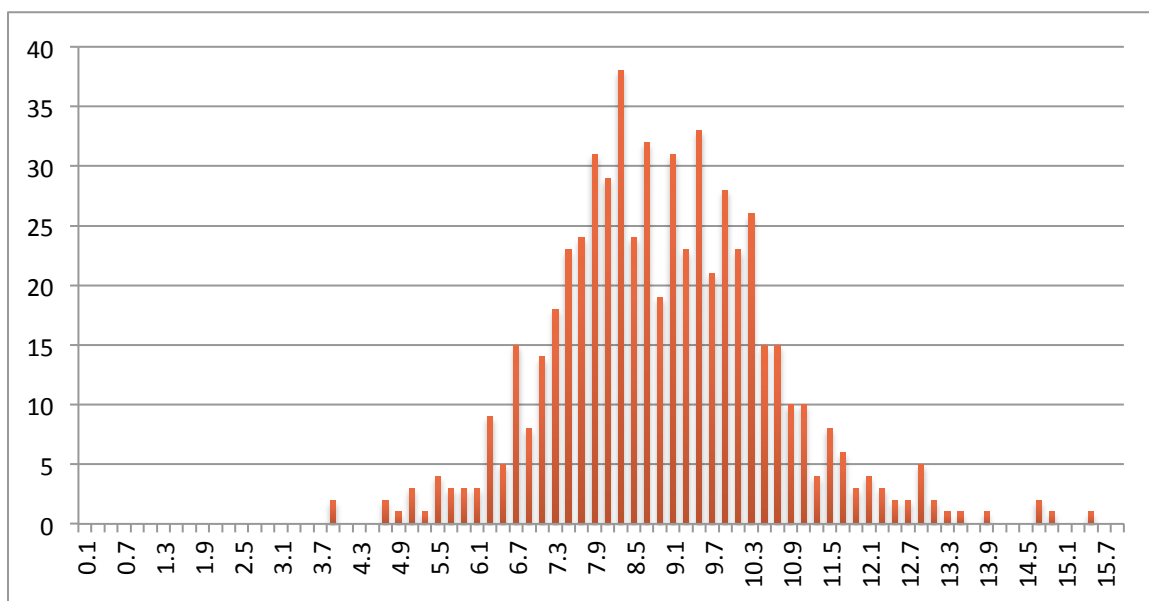


Figure A17 - Histogram of nanoparticle diameters at 0.8 nm film thickness of Sample T7.

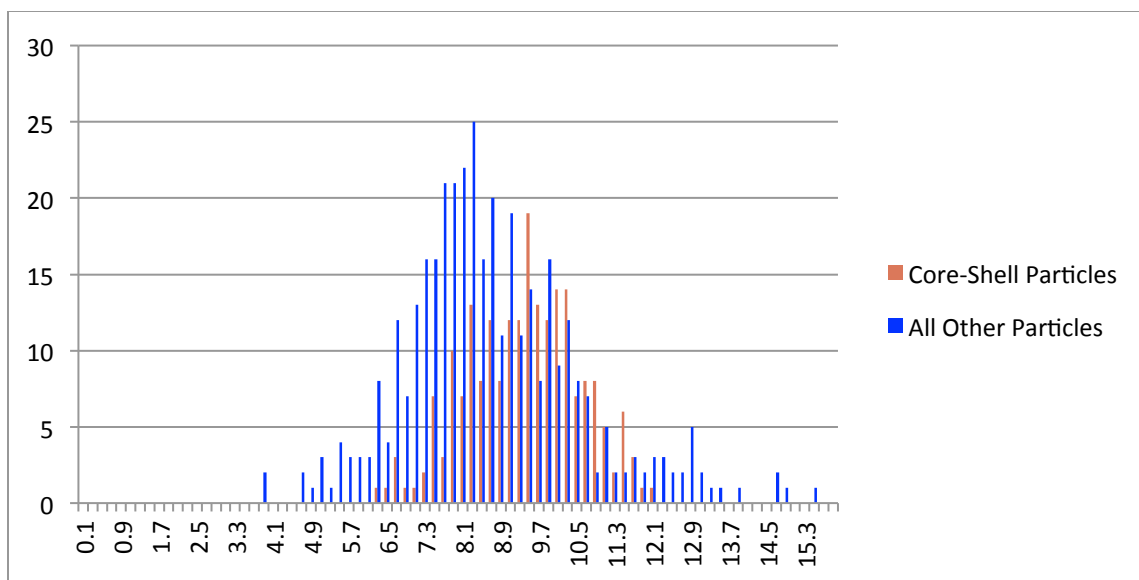


Figure A18 - Histogram of nanoparticle diameters at 0.8 nm film thickness of Sample T7 segmented by core-shell structure.

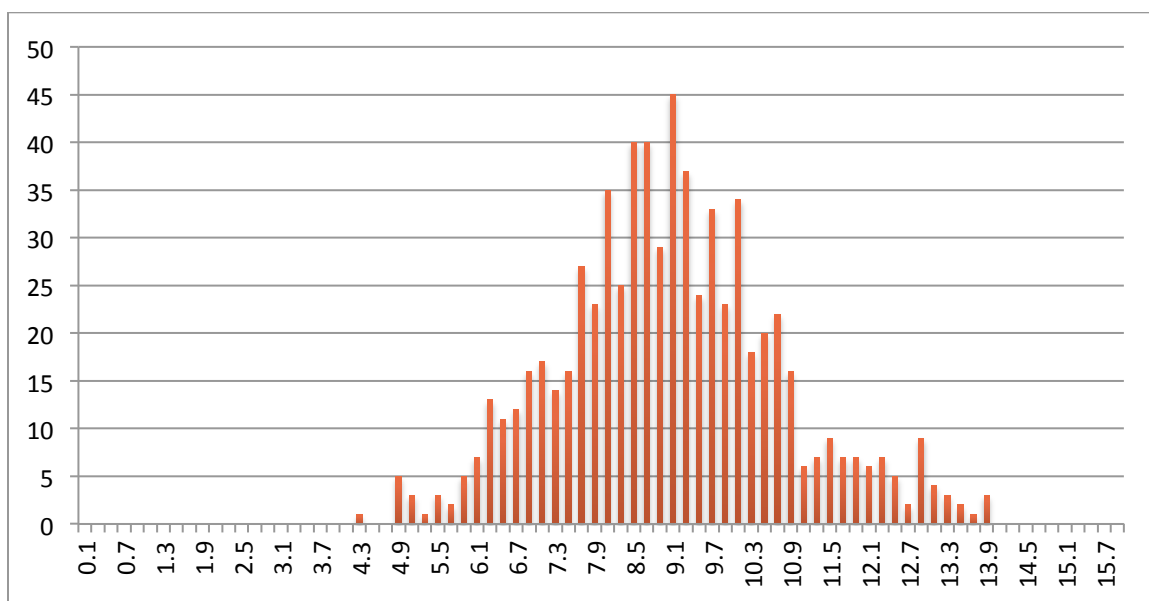


Figure A19 - Histogram of nanoparticle diameters at 0.9 nm film thickness of Sample T7.

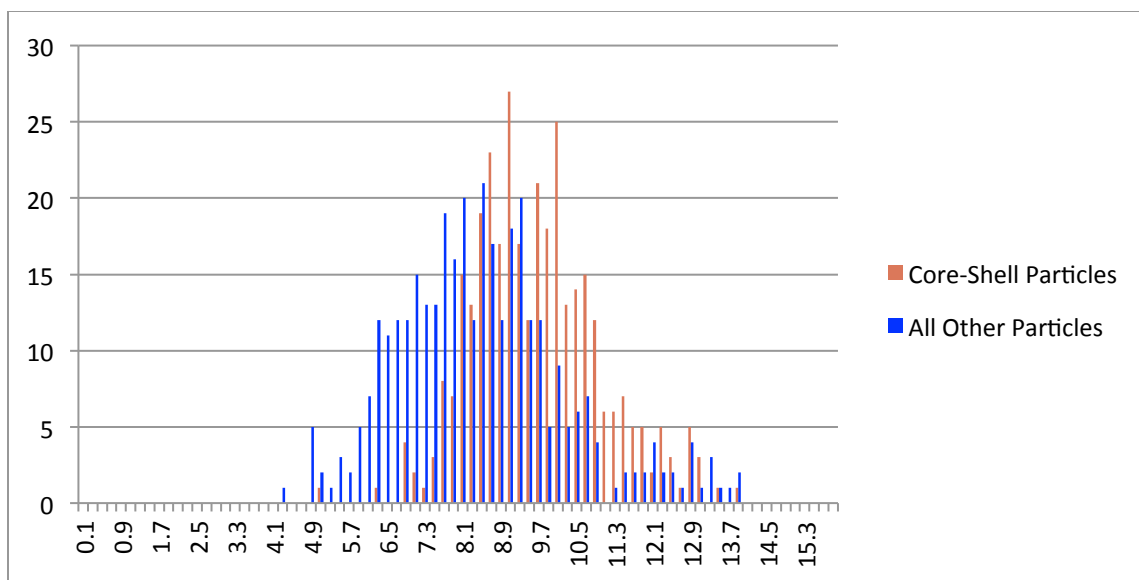


Figure A20 - Histogram of nanoparticle diameters at 0.9 nm film thickness of Sample T7 segmented by core-shell structure.

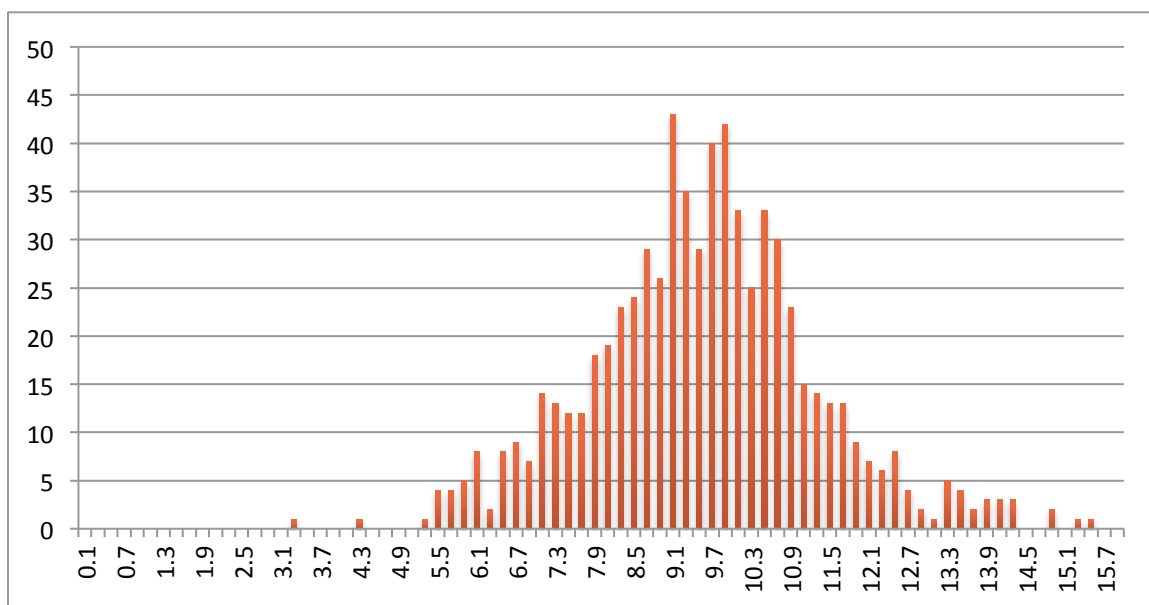


Figure A21 - Histogram of nanoparticle diameters at 1.0 nm film thickness of Sample T7.

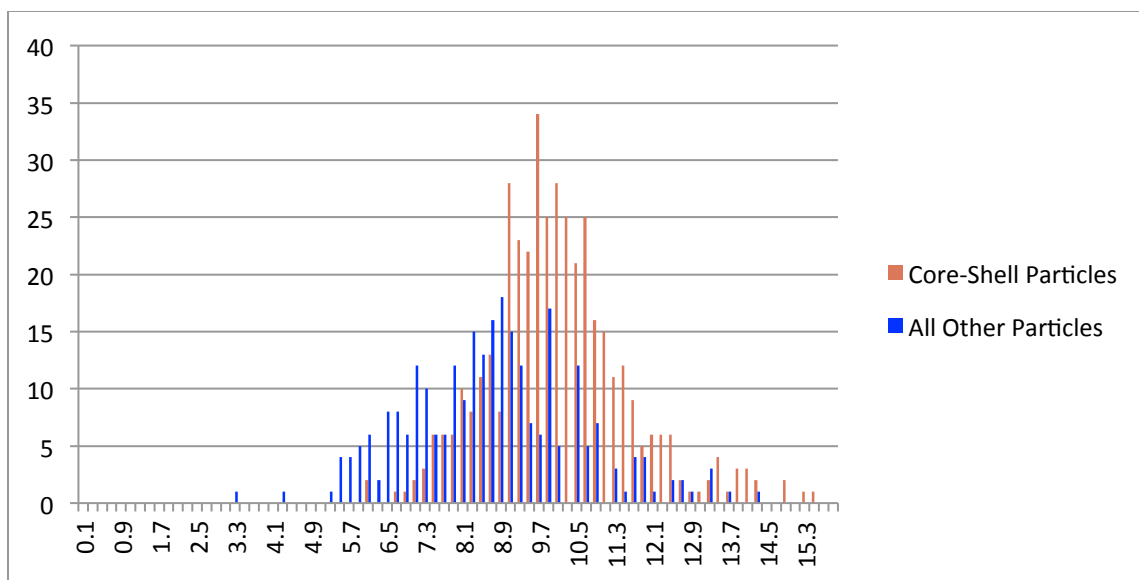


Figure A22 - Histogram of nanoparticle diameters at 1.0 nm film thickness of Sample T7 segmented by core-shell structure.

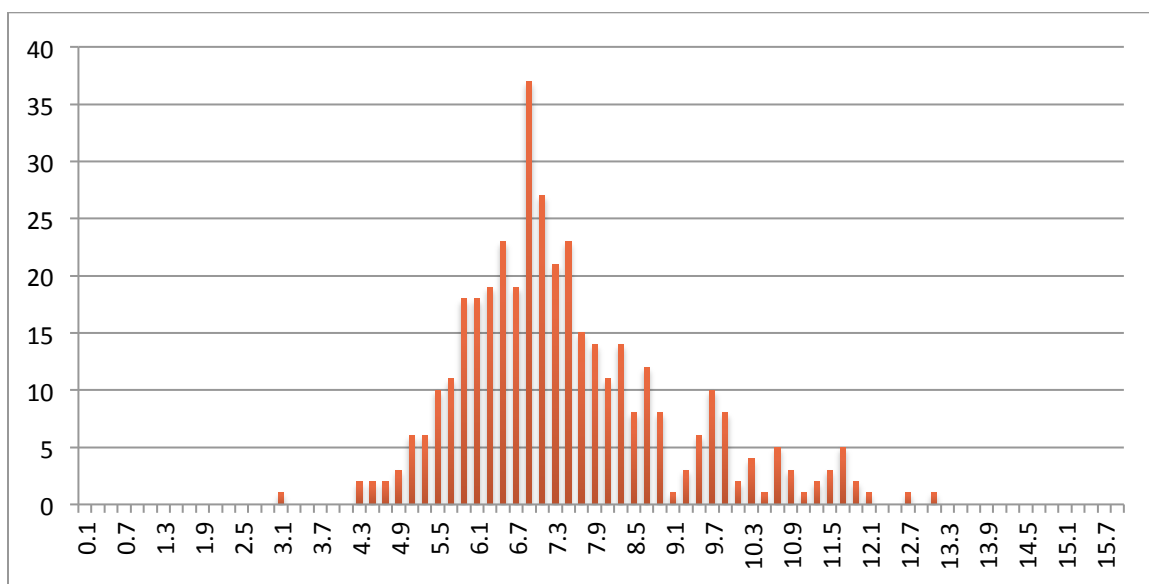


Figure A23 - Histogram of nanoparticle diameters at 0.4 nm film thickness of Sample S8.

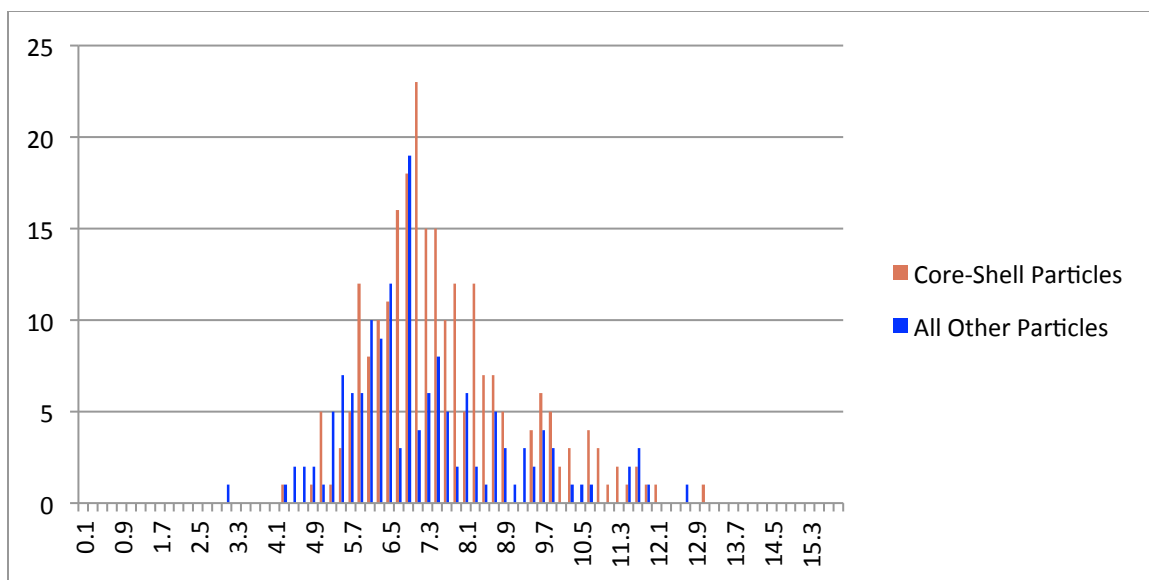


Figure A24 - Histogram of nanoparticle diameters at 0.4 nm film thickness of Sample S8 segmented by core-shell structure.

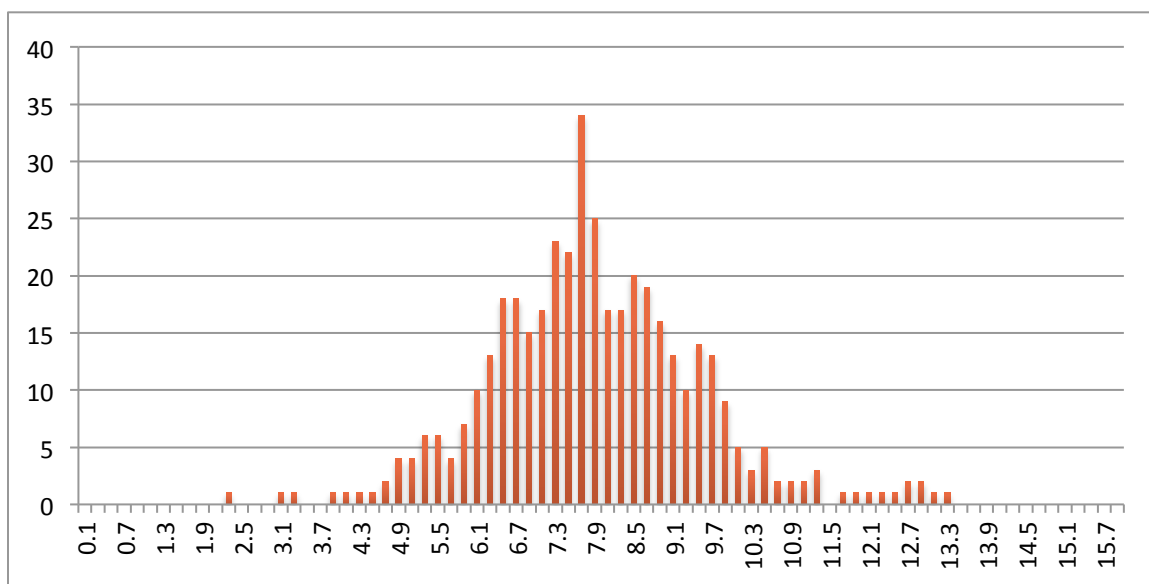


Figure A25 - Histogram of nanoparticle diameters at 0.5 nm film thickness of Sample S8.



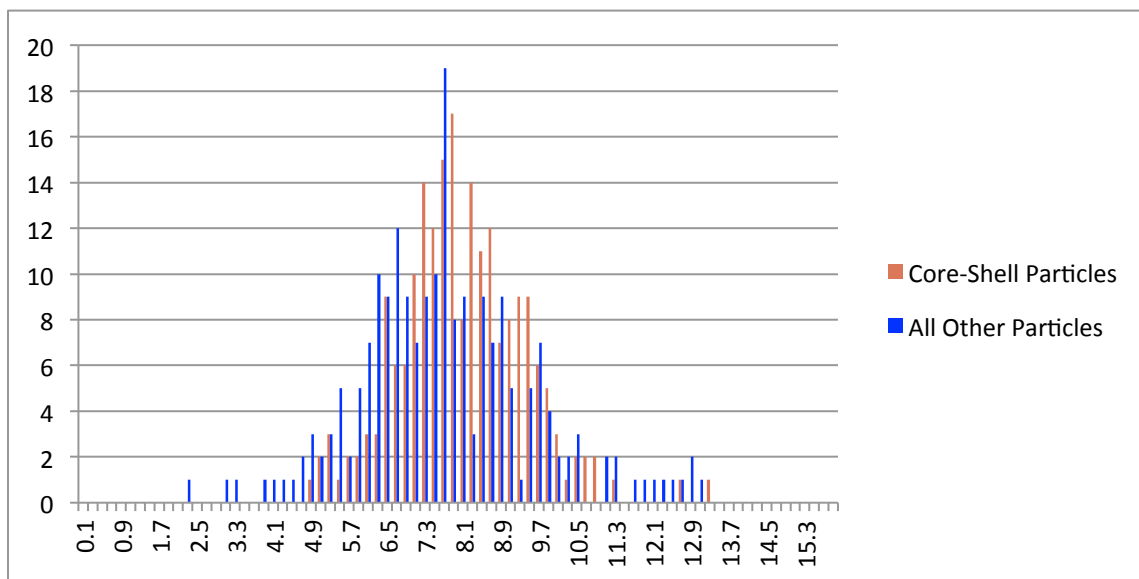


Figure A26 - Histogram of nanoparticle diameters at 0.5 nm film thickness of Sample S8 segmented by core-shell structure.

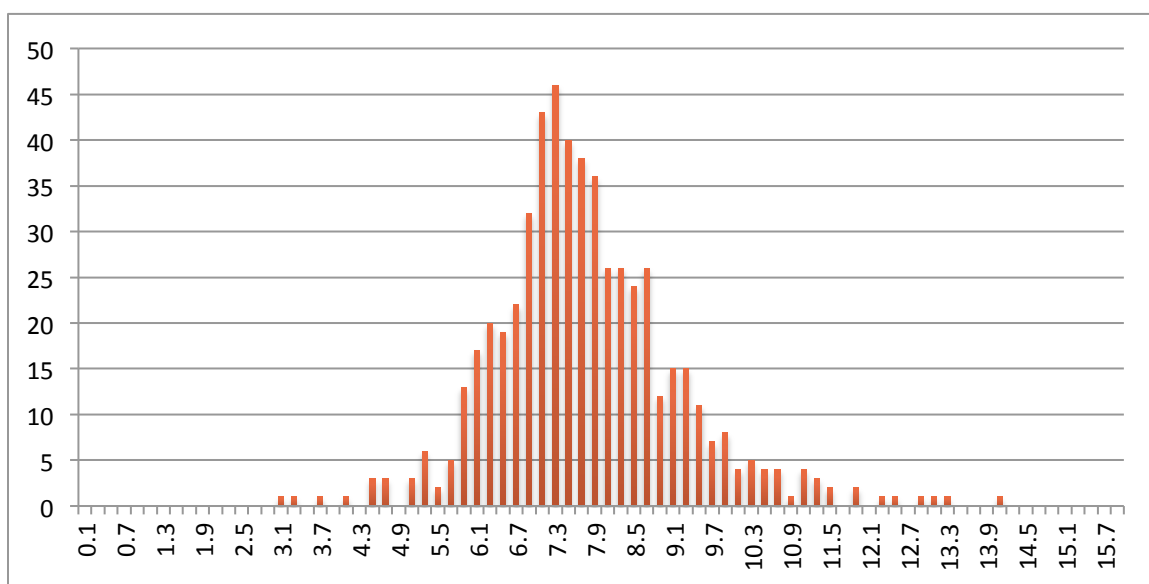


Figure A27 - Histogram of nanoparticle diameters at 0.6 nm film thickness of Sample S8.

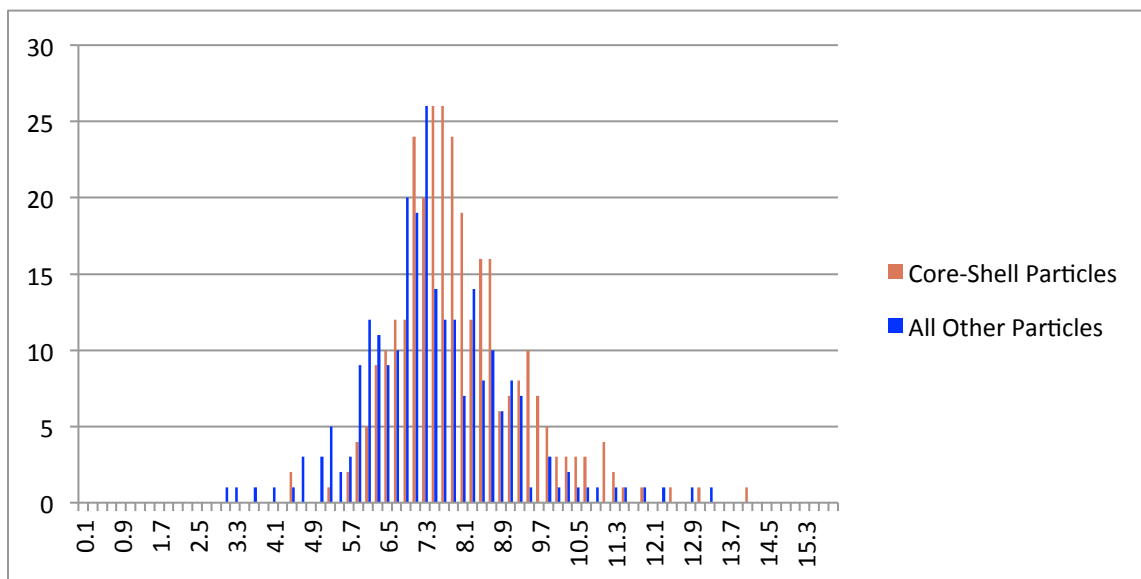


Figure A28 - Histogram of nanoparticle diameters at 0.6 nm film thickness of Sample S8 segmented by core-shell structure.

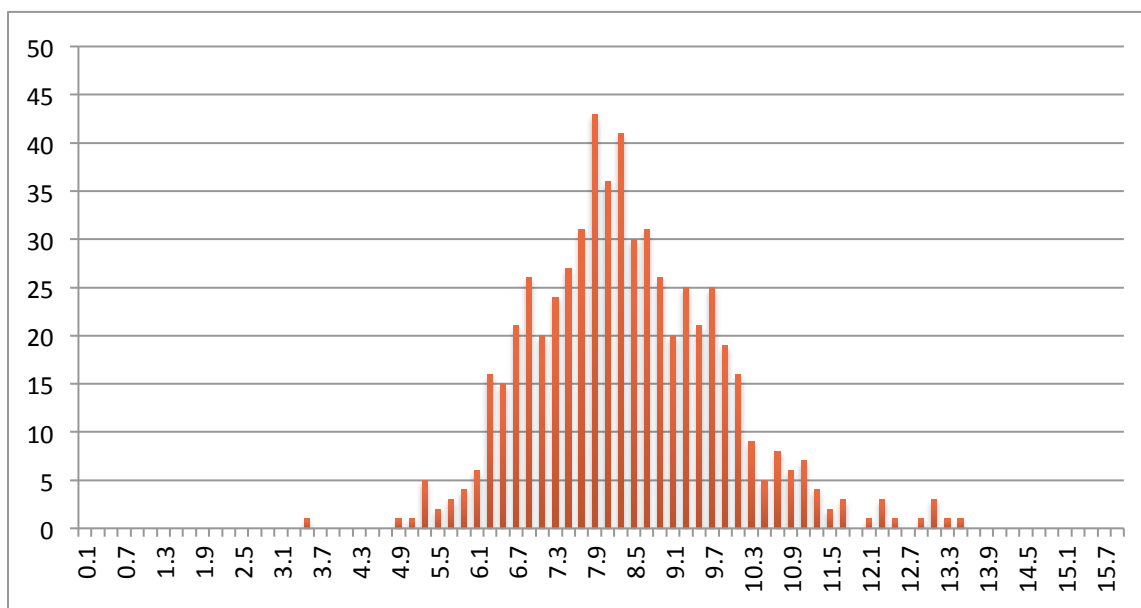


Figure A29 - Histogram of nanoparticle diameters at 0.7 nm film thickness of Sample S8.

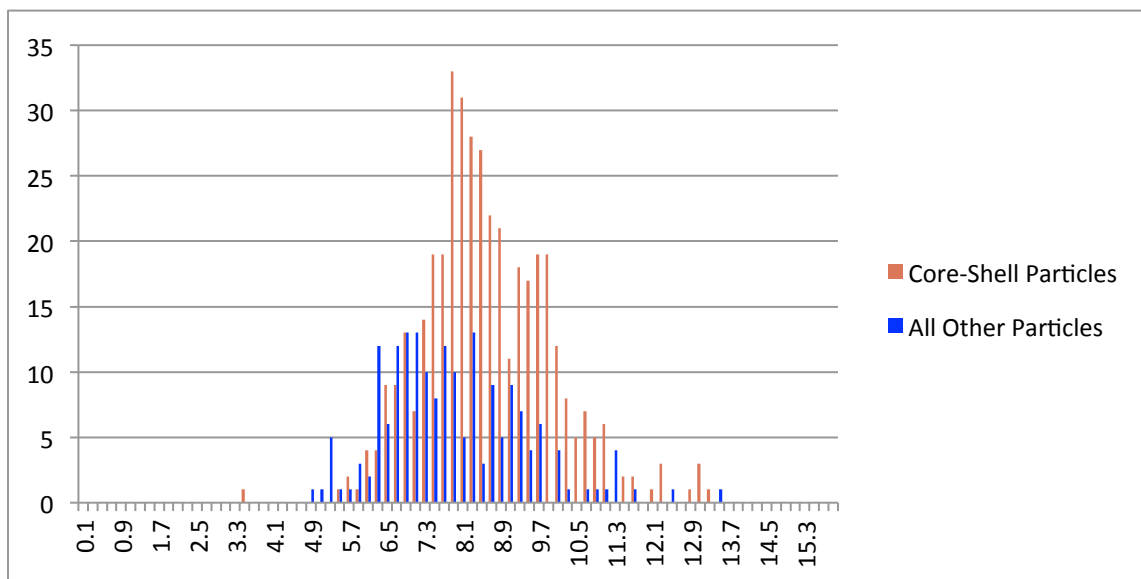


Figure A30 - Histogram of nanoparticle diameters at 0.7 nm film thickness of Sample S8 segmented by core-shell structure.

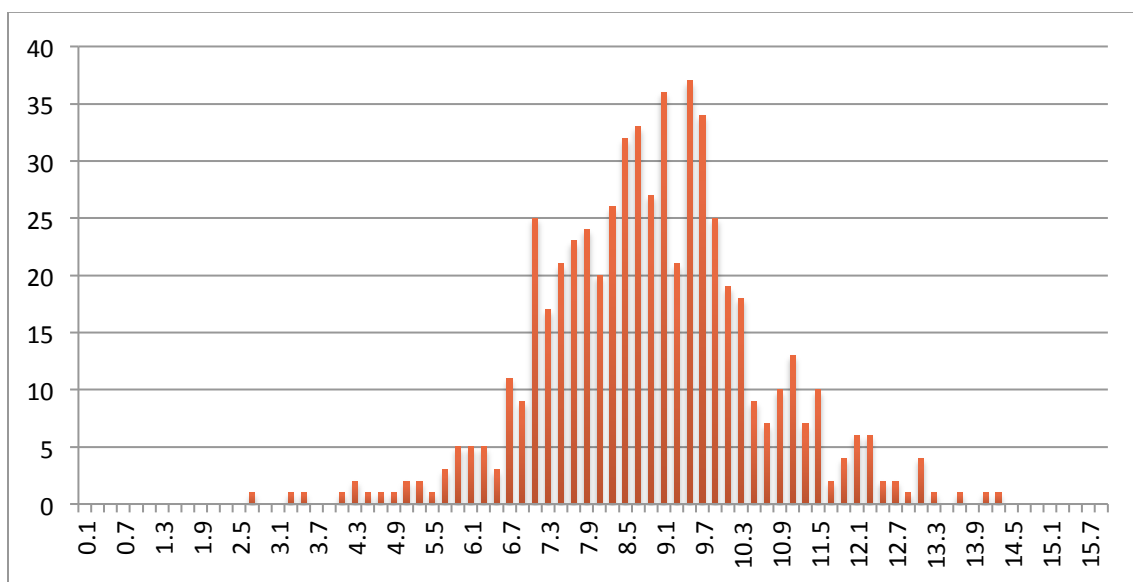


Figure A31 - Histogram of nanoparticle diameters at 0.8 nm film thickness of Sample S8.

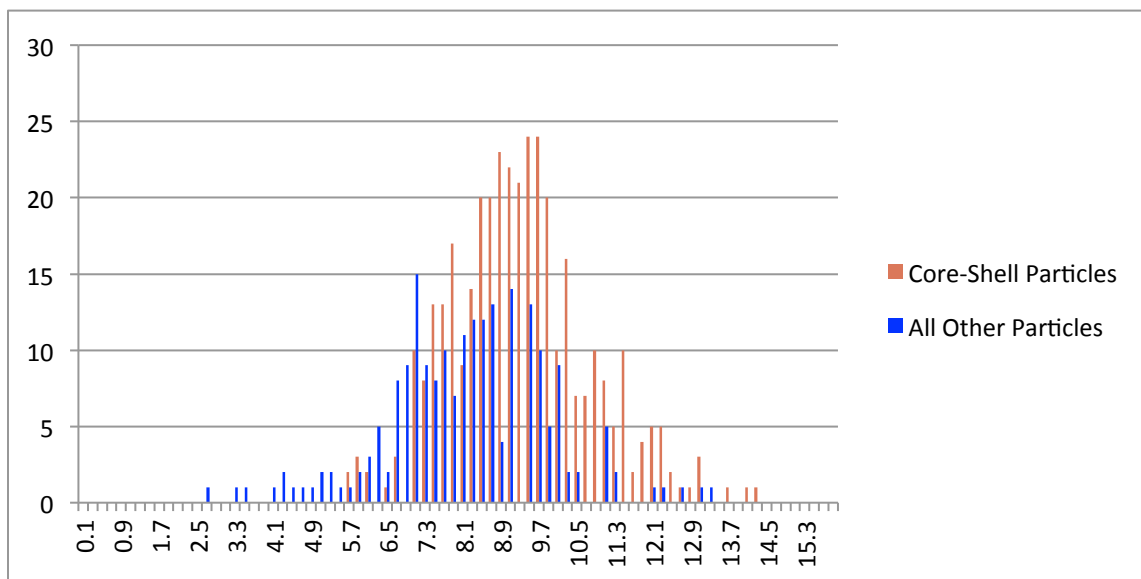


Figure A32 - Histogram of nanoparticle diameters at 0.8 nm film thickness of Sample S8 segmented by core-shell structure.

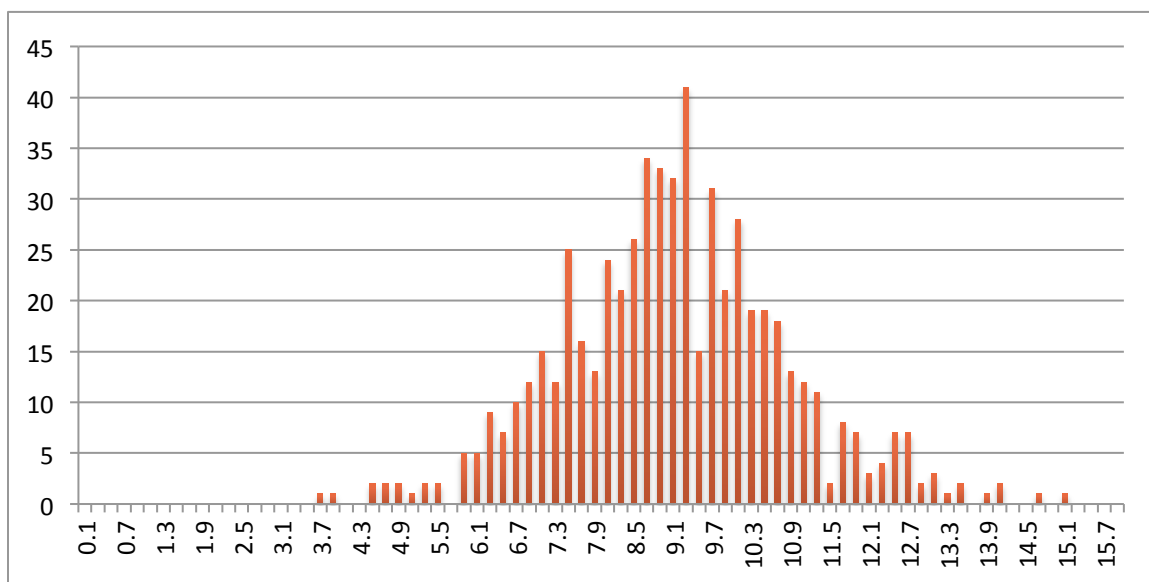


Figure A33 - Histogram of nanoparticle diameters at 0.9 nm film thickness of Sample S8.

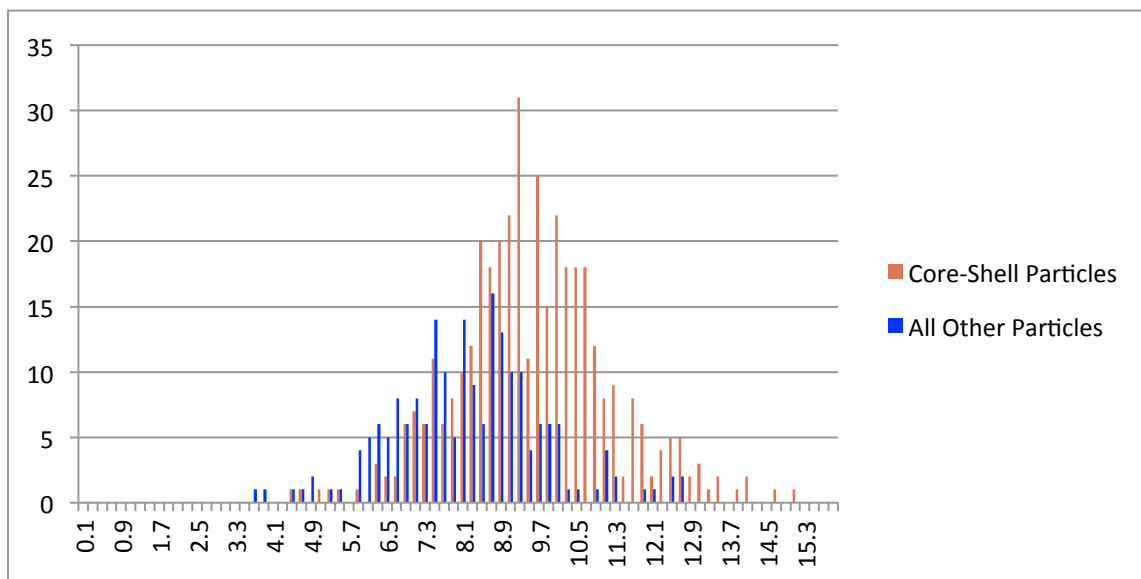


Figure A34 - Histogram of nanoparticle diameters at 0.9 nm film thickness of Sample S8 segmented by core-shell structure.

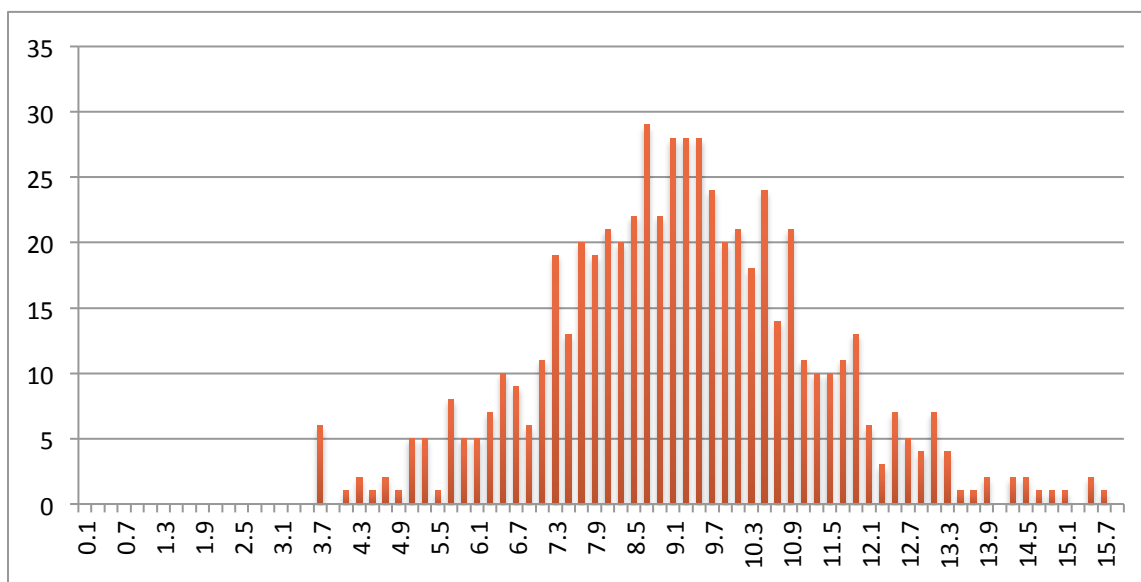


Figure A35 - Histogram of nanoparticle diameters at 1.0 nm film thickness of Sample S8.

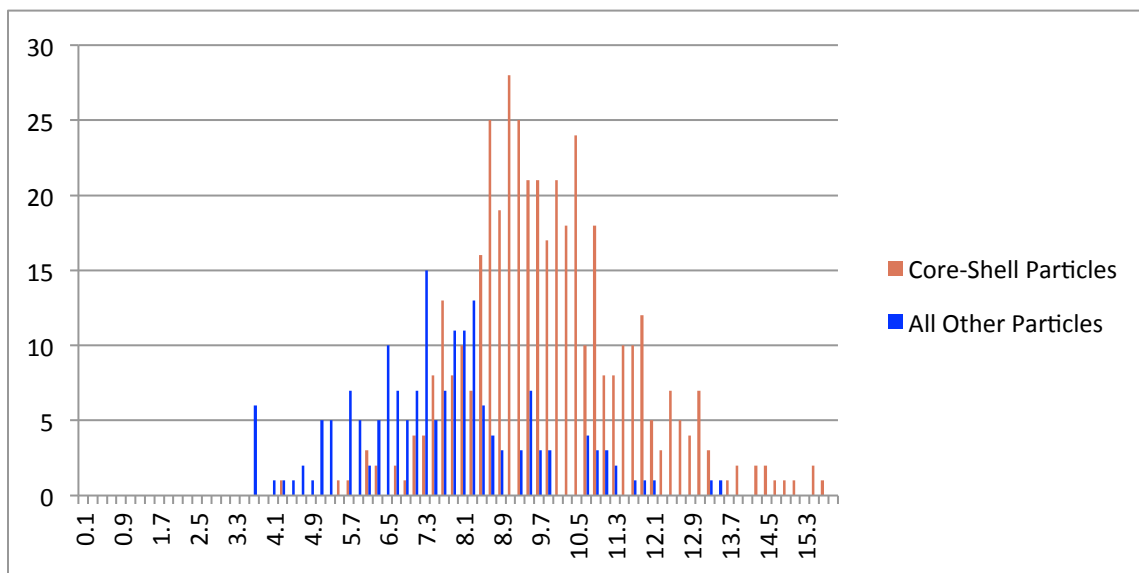


Figure A36 - Histogram of nanoparticle diameters at 1.0 nm film thickness of Sample S8 segmented by core-shell structure.

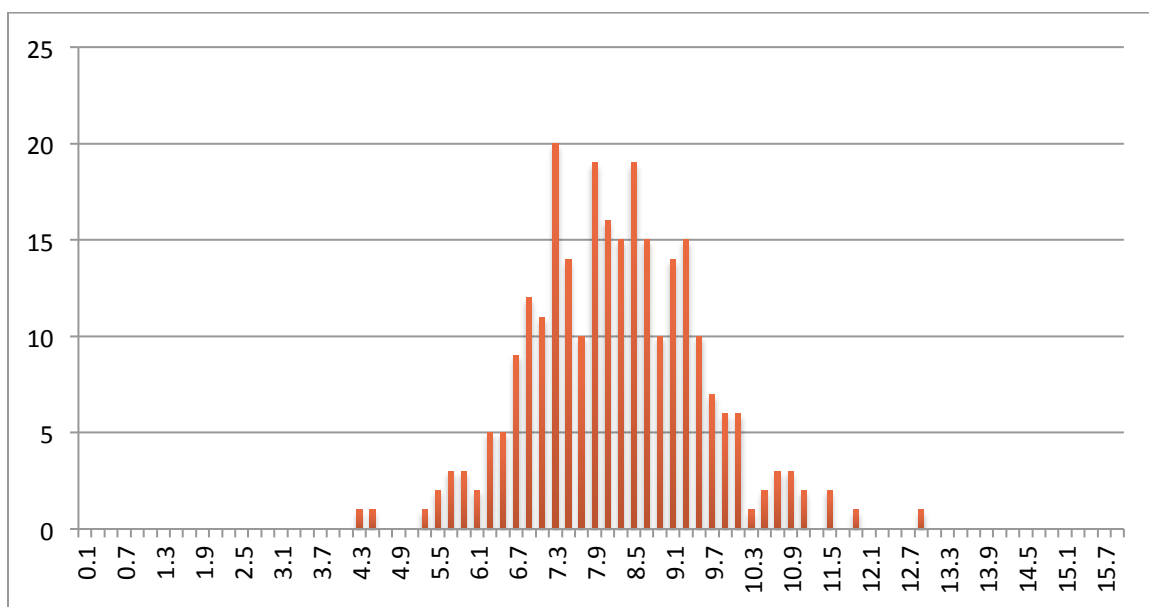


Figure A37 - Histogram of nanoparticle diameters at 0.4 nm film thickness of Sample T9.

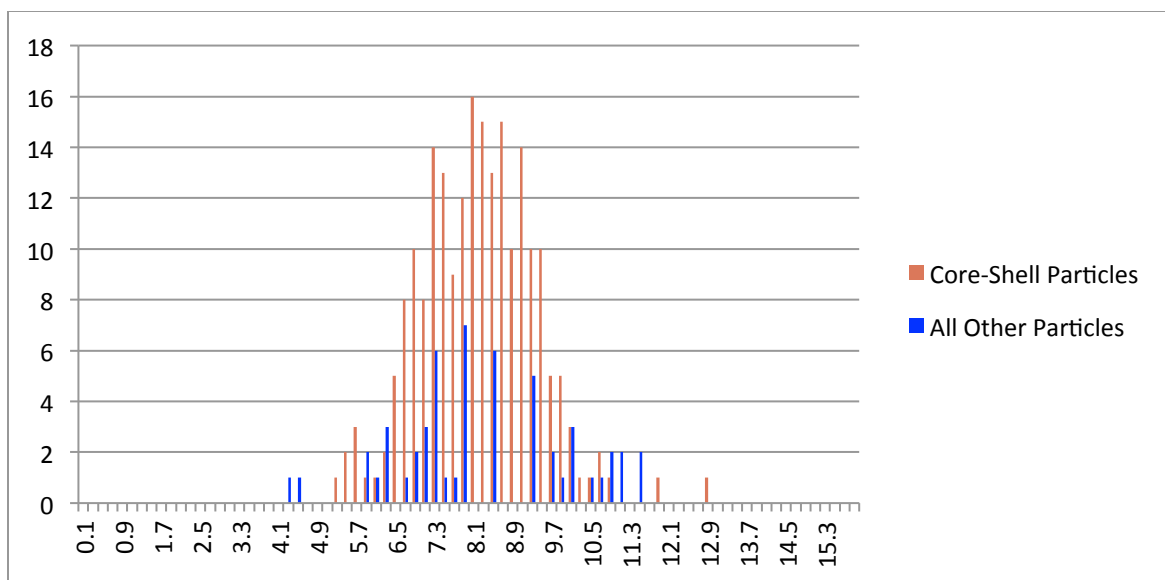


Figure A38 - Histogram of nanoparticle diameters at 0.4 nm film thickness of Sample T9 segmented by core-shell structure.

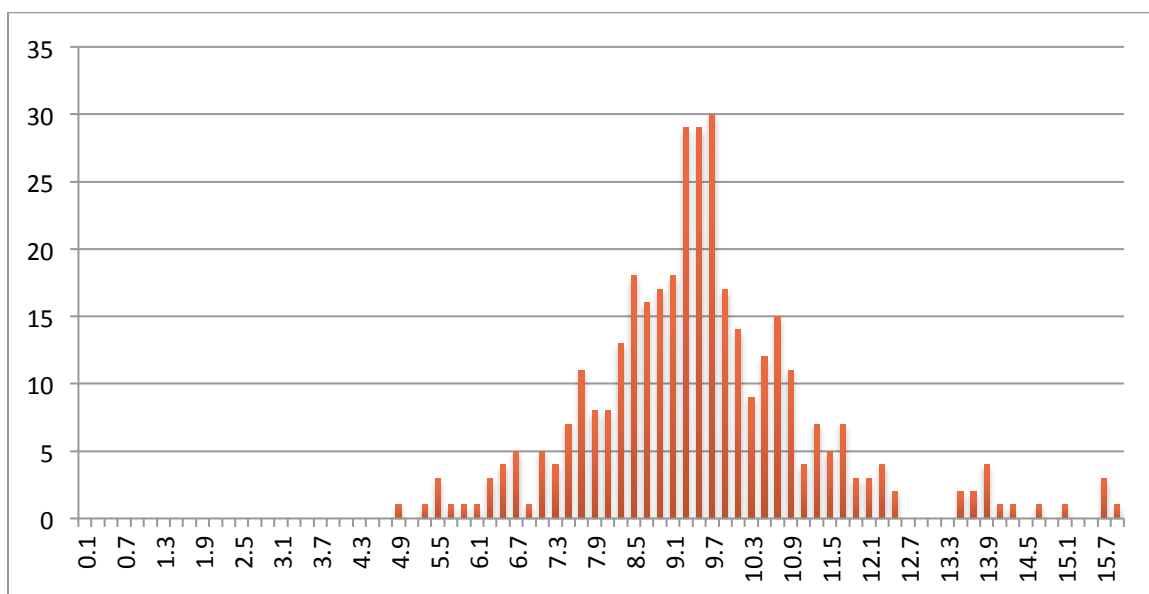


Figure A39 - Histogram of nanoparticle diameters at 0.5 nm film thickness of Sample T9.

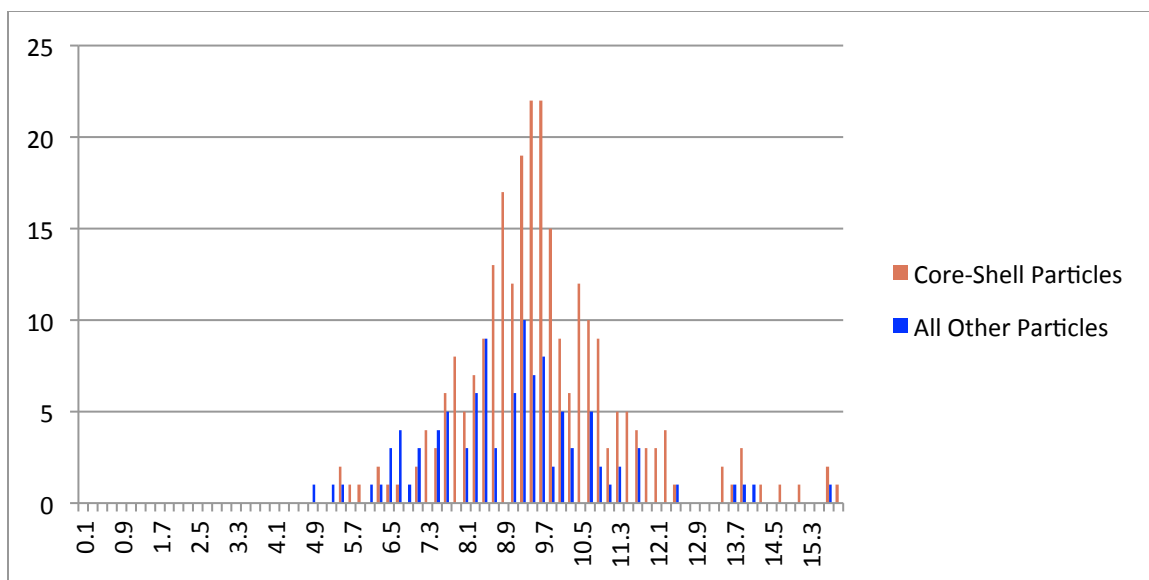


Figure A40 - Histogram of nanoparticle diameters at 0.5 nm film thickness of Sample T9 segmented by core-shell structure.

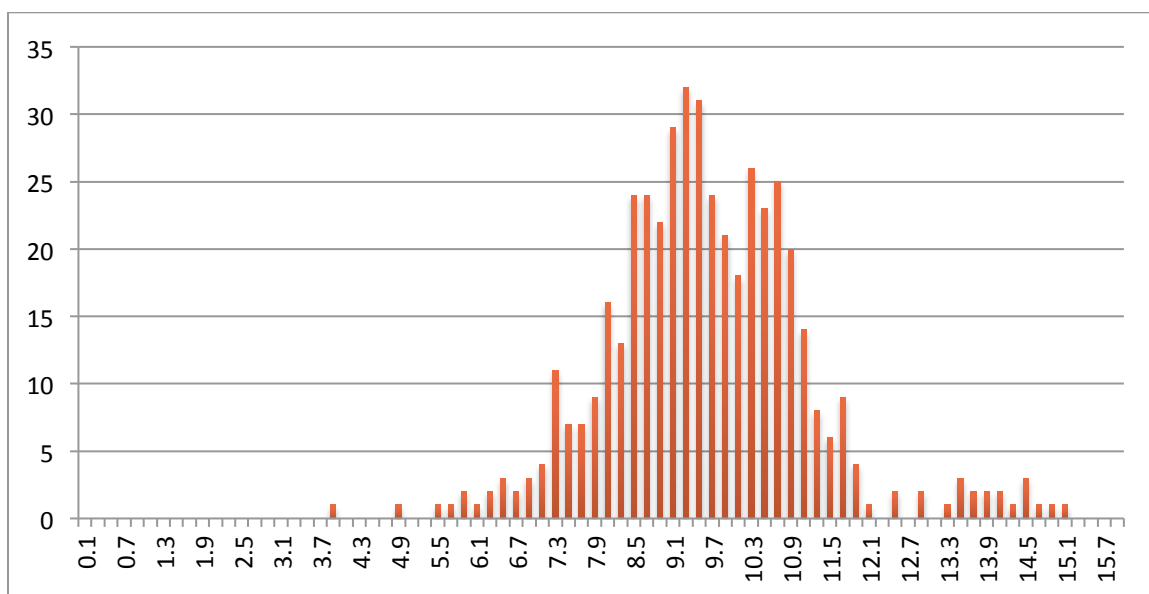


Figure A41 - Histogram of nanoparticle diameters at 0.6 nm film thickness of Sample T9.



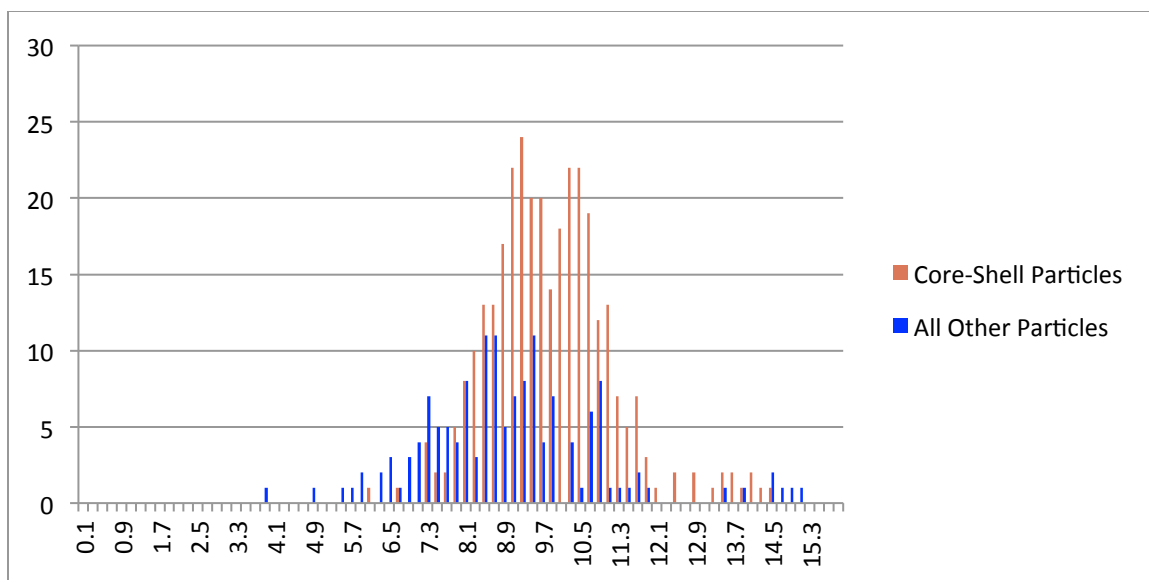


Figure A42 - Histogram of nanoparticle diameters at 0.6 nm film thickness of Sample T9 segmented by core-shell structure.

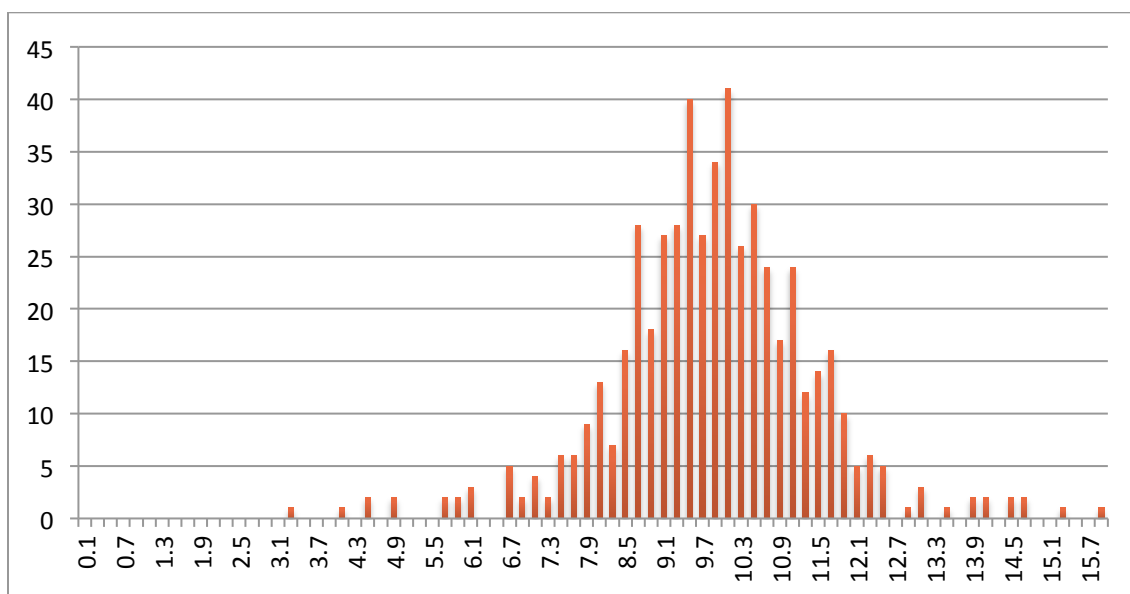


Figure A43 - Histogram of nanoparticle diameters at 0.7 nm film thickness of Sample T9.

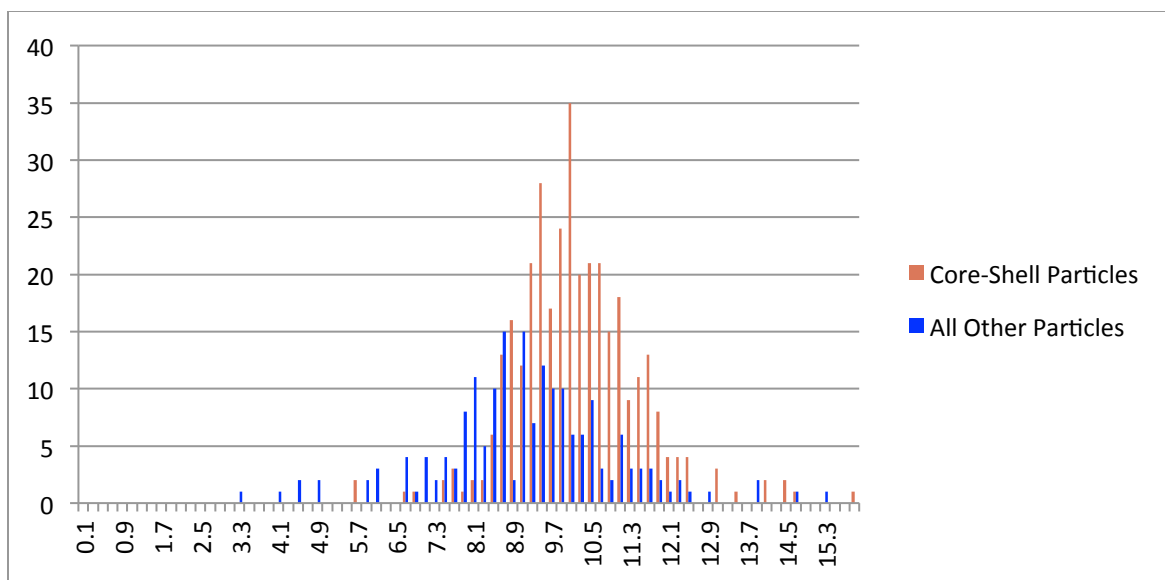


Figure A44 - Histogram of nanoparticle diameters at 0.7 nm film thickness of Sample T9 segmented by core-shell structure.

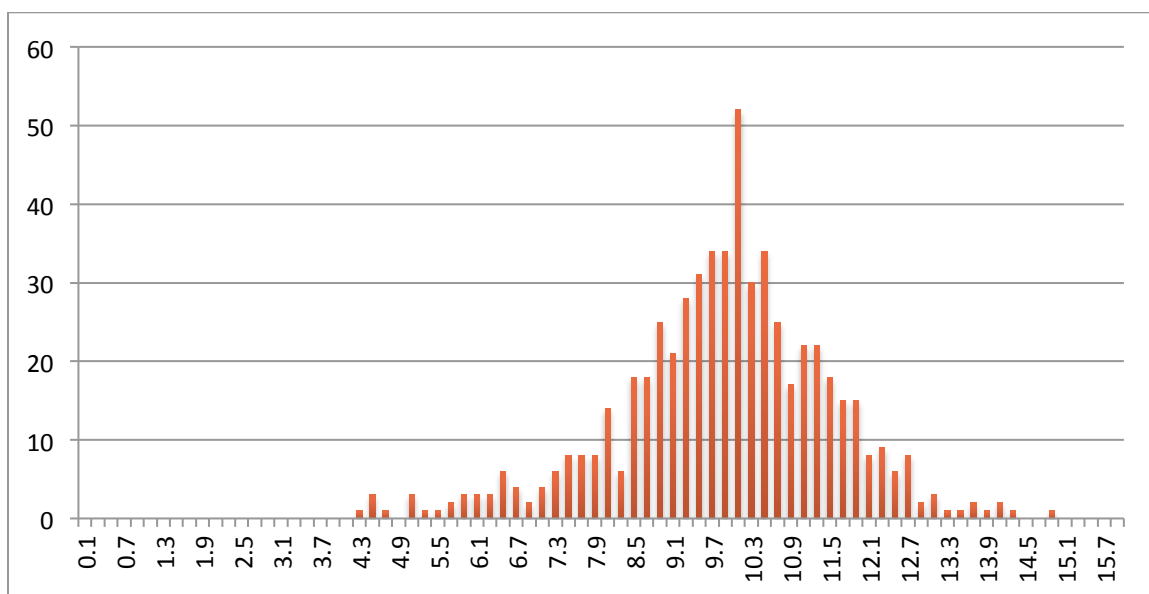


Figure A45 - Histogram of nanoparticle diameters at 0.8 nm film thickness of Sample T9.

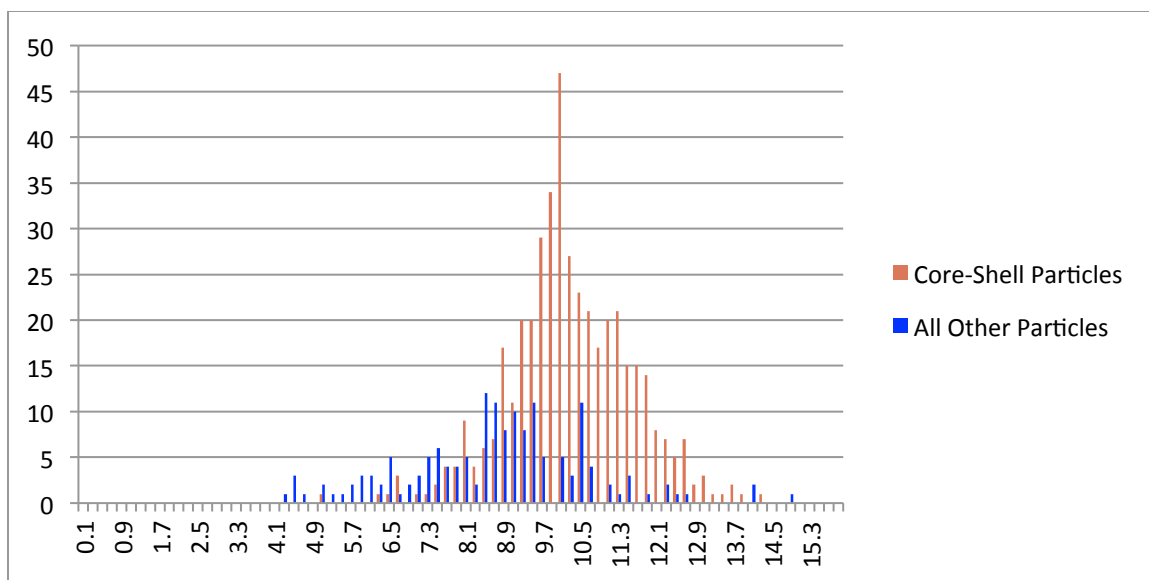


Figure A46 - Histogram of nanoparticle diameters at 0.8 nm film thickness of Sample T9 segmented by core-shell structure.

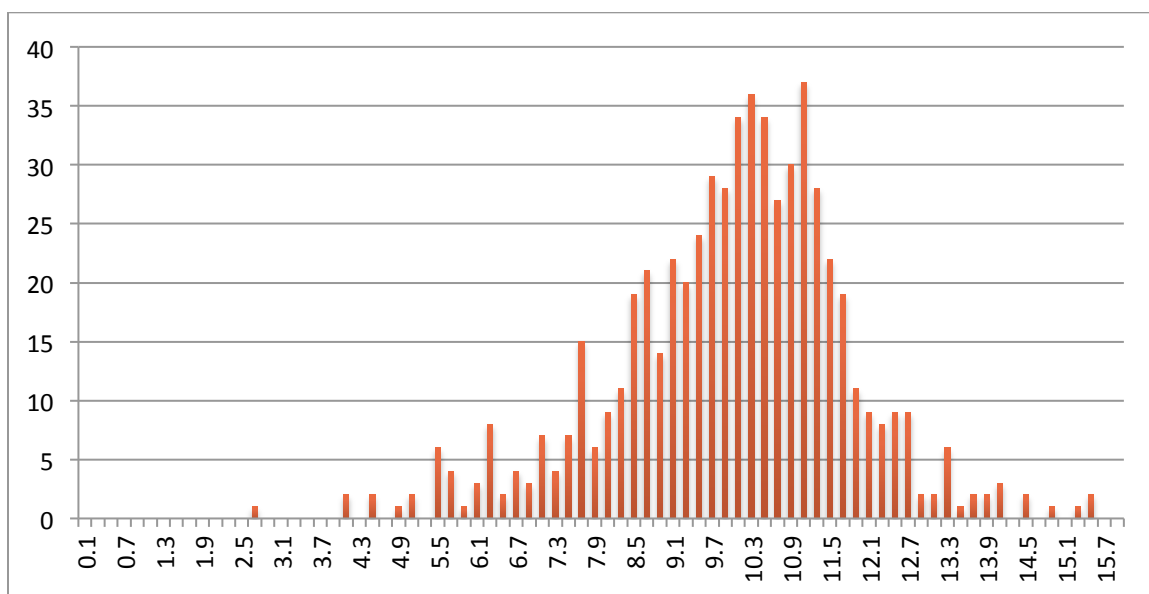


Figure A47 - Histogram of nanoparticle diameters at 0.9 nm film thickness of Sample T9.

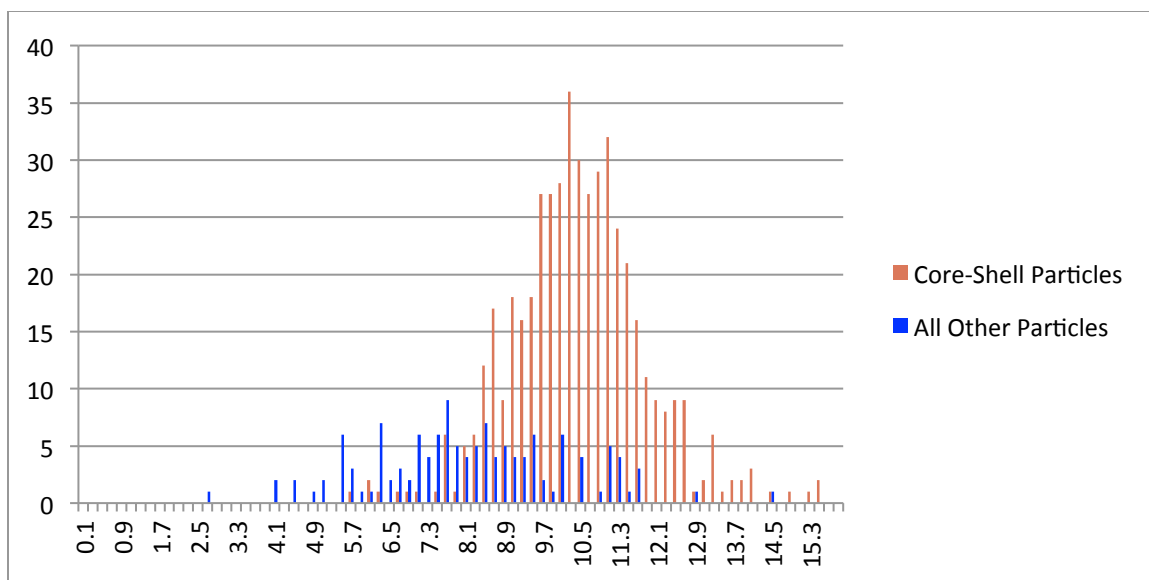


Figure A48 - Histogram of nanoparticle diameters at 0.9 nm film thickness of Sample T9 segmented by core-shell structure.

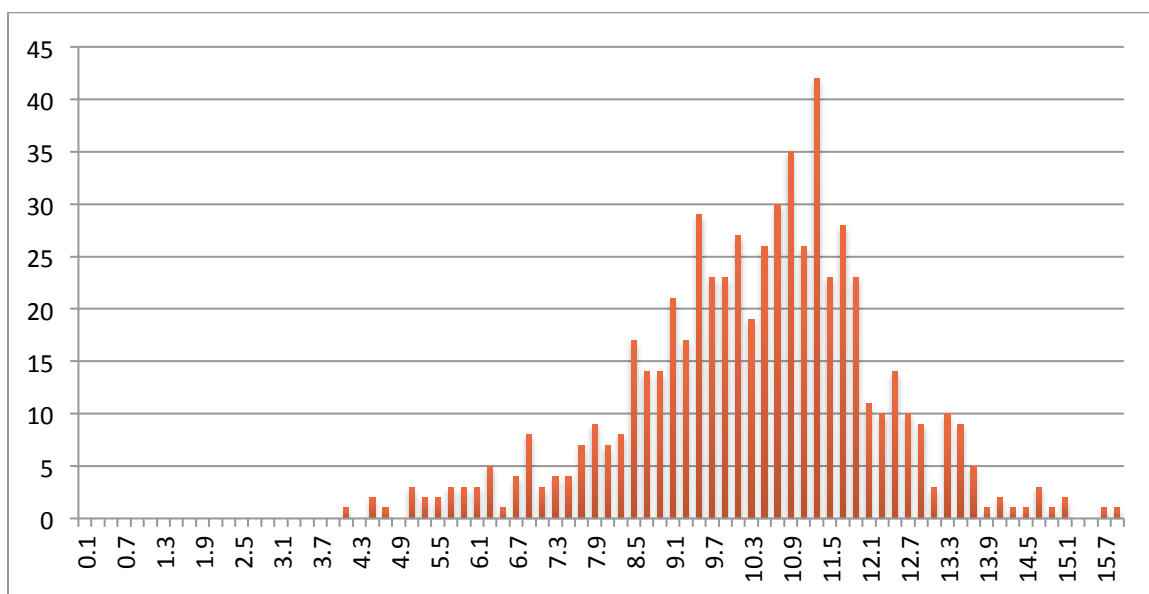


Figure A49 - Histogram of nanoparticle diameters at 1.0 nm film thickness of Sample T9.

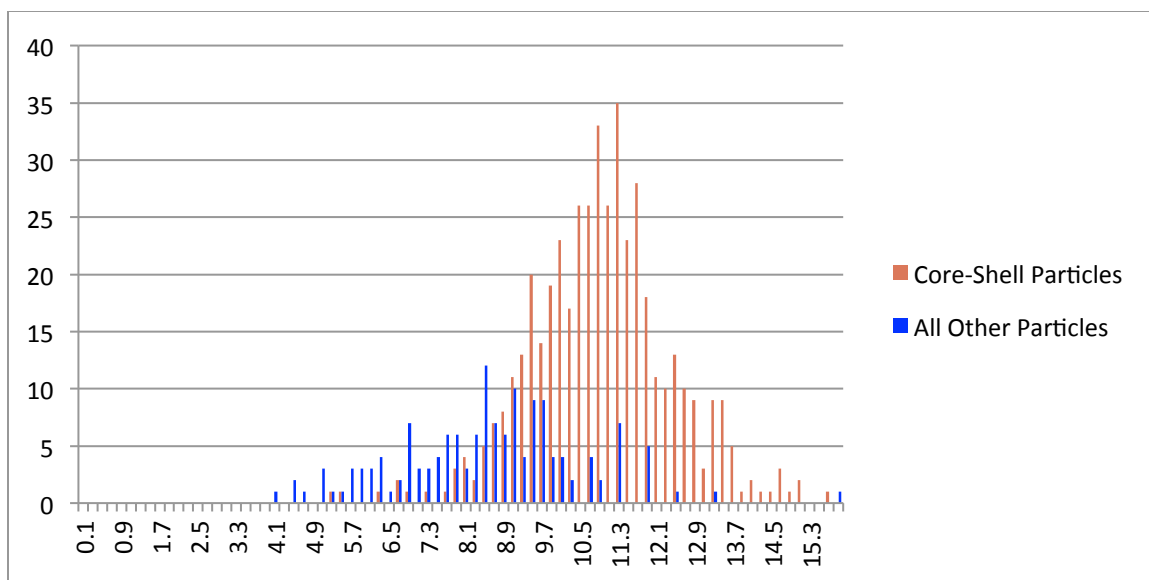


Figure A50 - Histogram of nanoparticle diameters at 1.0 nm film thickness of Sample T9 segmented by core-shell structure.

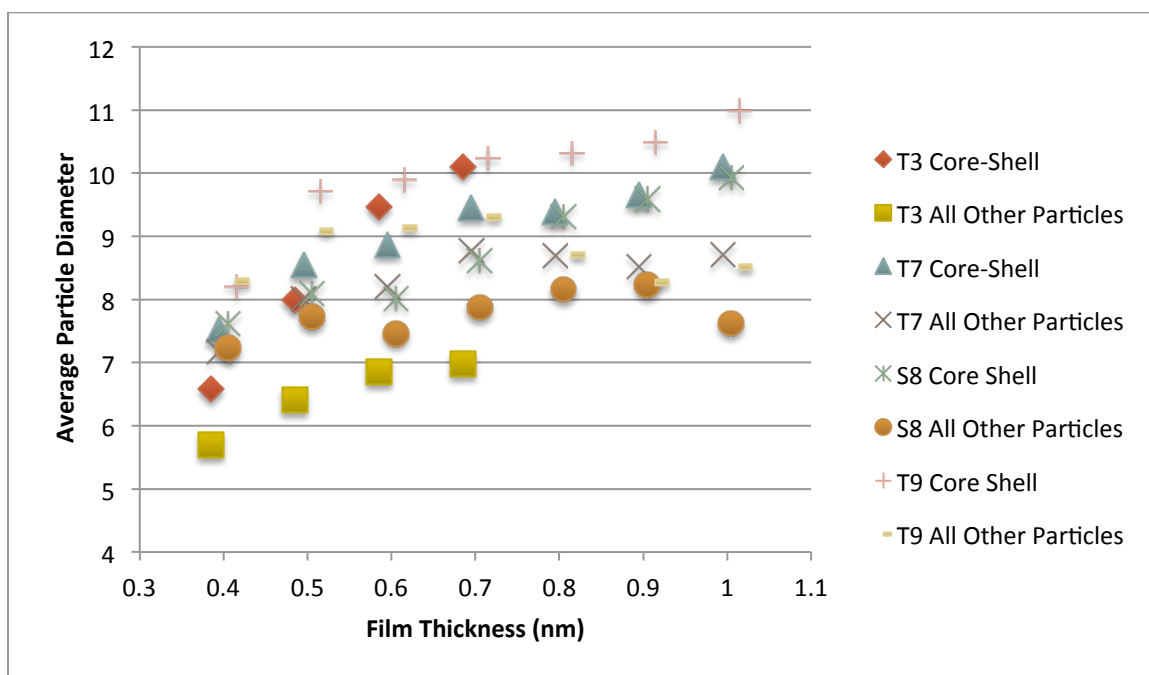


Figure A51 - Average particle size by segmented populations. Core-shell structures are generally larger than non-core shell particles and the difference becomes greater at increasing film thicknesses.

VITA

## VITA

Sammy Saber was born and raised in Terre Haute, IN. After spending nearly 18 years in one state, he decided to experience life in a bigger city and moved to Philadelphia, PA to work towards his undergraduate degree at the University of Pennsylvania (Penn). After spending a year not knowing what to study, Sammy stumbled upon Materials Science & Engineering and became fascinated with the power and beauty of crystal structures. While looking for a research opportunity, he found a summer research fellowship at Purdue University focusing on electron microscopy. Sammy was once again inspired by the power of this field had to visualize the micro and nanoscopic structure of materials. After completing his BSE in Materials at Penn, in an attempt to put off entering the job market during the worst economic crisis since the Great Depression, Sammy began studying for his Ph.D. at Purdue University in 2009 under the guidance of Dr. Eric Stach with a focus on utilizing transmission electron microscopy as a tool to study materials.